

**STRUCTURE, CHEMICAL COMPOSITION AND OPTICAL
PROPERTY RELATIONSHIP OF ALKALI-METAL
TUNGSTEN OXIDES AND NIOBIUM TUNGSTEN OXIDES**

Von der Naturwissenschaftlichen Fakultät der
Gottfried Wilhelm Leibniz Universität Hannover
zur Erlangung des Grades

Doktor der Naturwissenschaften
- Dr. rer. nat. -

genehmigte Dissertation
von

M.S. -Chem. Tapas Debnath

geboren am 12.03.1977 in Netrakona, Bangladesh

2008

Referent: Prof. Dr. Claus Henning Rücher

Korreferent: Prof. Dr. Josef-Christian Buhl

Tag der Promotion: 09.12.2008

ACKNOWLEDGEMENTS

I am extremely thankful to Professor Dr. Claus Henning Rüsch, Institute of Mineralogy, Leibniz University of Hannover, Germany, who has introduced me to the field of spectroscopy. His continuous supervision at each and every part has made this study as a full fledged thesis. He was exceptionally enthusiastic in providing new ideas for explaining new findings. My sincere gratitude is also for his tireless discussions, which have brought this thesis to its present form.

I am indebt to Professor Dr. Josef-Christian Buhl, Institute of Mineralogy, Leibniz University of Hannover, Germany, for his help in learning basic crystallography and for his whole-hearted guidelines.

My heartfelt thanks to PD Dr. habil Thorsten Michael Gesing, Department of Geoscience, University of Bremen, Germany, for his sincere support and help in learning X-ray diffractometry and Rietveld refinement.

I am also deeply indebted to Professor Dr. Altaf Hussain, Department of Chemistry, University of Dhaka, who introduced me to the field of Tungsten Bronzes. His kind cooperation, encouragement and valuable advice have helped me to perform my research work smoothly.

I am thankful to Professor Dr. Robert Glaum, Department of chemistry, University of Bonn, Germany, for giving me the opportunity to work in his laboratory for preparing some of my samples.

I would also like to thank Ms. Fongjan Jirasit, Institute of Building Materials Science, Leibniz University of Hannover, Germany, for her help in learning electron microscopy.

My heartfelt thanks to Dr. Kalpana Rani Dey, Independent University, Bangladesh, for discussion about some of my results during her visit in Germany.

I am grateful to my loving mother and sisters for their constant encouragement.

I thank all of my colleagues in the institute specially Aftab A. Shaikh, Christoph Hübsch, Elzbieta Mielcarek, Florian Stemme, Lars Roben., Robert Knobel, Sara Fanara, Tanja Höfs, Wanja Dziony, who always make my life joyful.

Finally, I would like to thank the Ministry of Science and Culture, Land Niedersachsen for providing me “Georg-Christoph-Lichtenberg-Stipendium”, which has made possible my studies in Germany.

ABSTRACT

The relationship between chemical composition, structure and optical property in alkali metal tungsten oxides (tungsten bronzes) and niobium tungsten oxides (block type compounds) was investigated using X-ray powder diffraction, optical microscopy, microprobe analysis, Raman and optical spectroscopic techniques.

Substitution experiments of nominal compositions $\text{Na}_{0.8}\text{Nb}_y\text{W}_{1-y}\text{O}_3$ ($y = 0.0 - 0.4$) show a single phase cubic perovskite tungsten bronze (PTB_c) type structure up to $y = 0.07$. Further increase in Nb content show an additional PTB_c type phase up to $y = 0.2$. For nominal compositions $y > 0.2$ even a separation into three distinct colored crystallites with cubic perovskite type structure is obtained: (i) red-orange Na_xWO_3 crystallites with slightly decreasing x (i.e. 0.8 to 0.72) with increasing nominal y , (ii) bluish crystallites of variable compositions $\text{Na}_x\text{Nb}_y\text{W}_{1-y}\text{O}_3$, and (iii) white crystallites of a new phase with composition $\text{Na}_{0.5}\text{NbO}_{2.75}$. Substitution experiments of nominal compositions $\text{K}_{0.55}\text{Nb}_y\text{W}_{1-y}\text{O}_3$ show up to $y = 0.07$ tetragonal tungsten bronze (TTB) type single phase. Samples with nominal niobium content $y > 0.07$ show an additional cubic pyrochlore type phase.

Na_xWO_3 samples reveal coexisting phases of cubic perovskite tungsten bronze (PTB_c), tetragonal tungsten bronze (TTB), and tetragonal perovskite tungsten bronze (PTB_t) in the range of $0.15 \leq x \leq 0.4$, which has been quantified. Pure PTB_t and orthorhombic perovskite tungsten bronze (PTB_o) appear for $x = 0.1$, and 0.05, respectively. Structural studies for single phase PTB_c Na_xWO_3 show that all compositions in the range of $0.4 < x < 0.9$ can uniquely be refined using space group Im-3 . The linear increase in lattice parameters with increasing x in PTB_c Na_xWO_3 is explained by increasing W-O bond length, suggesting an x independent tilt of about 3° of the WO_6 octahedra. For the PTB_t phase it is shown that the puckering effect, i.e. the off centering of W along c -axis, is insufficient to explain the structure. Additionally the WO_6 octahedra show a tilt around the c axis, which is consistent with space group P4/ncc .

The optical properties of the metallic compositions of the systems Li_xWO_3 , Na_xWO_3 , K_xWO_3 , Cs_xWO_3 , $\text{Na}_x\text{Nb}_y\text{W}_{1-y}\text{O}_3$, and $\text{K}_x\text{Nb}_y\text{W}_{1-y}\text{O}_3$ reveal that the optical plasma edge shifts systematically as a function of x and y , which enable to estimate the effect of doping and pleochroism. However, the Drude free electron description of the optical properties is found to be insufficient. Instead the optical spectra can be described using an oscillator function of a transversal optical mode at about 2000 cm^{-1} and high oscillator strength in addition to a Drude free electron function. A similar quantification of the optical properties of $\text{Nb}_{18-x}\text{W}_{9+x}\text{O}_{69}$ ($x = 0, 2, 4, 6, 8$, and 9) block type compounds is obtained. It is concluded that a Feynman-polaron

model which includes an oscillator effect for the internal polaron oscillations and a Drude term for the polaron drift contribution could uniquely describe the optical features of the metallic samples.

Keywords: Alkali metal tungsten bronzes, Optical properties, Polaron.

ABSTRACT

Die Beziehung zwischen chemischer Zusammensetzung, Struktur und optischer Eigenschaft von Alkalimetall-Wolframoxiden (Wolframbronzen) und Niob-Wolframoxiden (Blocktyp-Verbindungen) wurde mit Hilfe von Röntgenpulvermethoden, optischer Mikroskopie, Mikrosondenanalysen, Raman und optischer Spektroskopietechniken untersucht.

Substitutionsexperimente mit nominellen Zusammensetzungen $\text{Na}_{0.8}\text{Nb}_y\text{W}_{1-y}\text{O}_3$ ($y = 0.0 - 0.4$) zeigen einphasige Perovskit-Wolframbronzen kubischer Symmetrie (PTB_c) bis $y = 0.07$. Bei einer weiteren Zunahme des Nb-Anteils zeigt sich eine zusätzliche PTB_c Phase bis $y = 0.2$. Für nominelle Zusammensetzungen $y > 0.2$ wird sogar eine Separation in drei verschieden farbige Kristalltypen mit kubischer Perovskit Typ Struktur erhalten: (i) rot-orange Na_xWO_3 -Kristalle mit einem leicht abnehmendem x (d.h. 0.8 to 0.72) mit zunehmendem nominellen y , (ii) bläuliche Kristall variabler Zusammensetzungen $\text{Na}_x\text{Nb}_y\text{W}_{1-y}\text{O}_3$ und (iii) weiße Kristalle einer neuen Phase der Zusammensetzung $\text{Na}_{0.5}\text{NbO}_{2.75}$. Substitutionsexperimente mit nominellen Zusammensetzungen $\text{K}_{0.55}\text{Nb}_y\text{W}_{1-y}\text{O}_3$ zeigen bis $y = 0.07$ eine Phase vom Typ tetragonaler Wolframbronzen (TTB). Proben mit nominellen Nb Anteil $y > 0.07$ zeigen eine zusätzliche Phase vom Pyrochlore Typ.

Na_xWO_3 Proben zeigen für $0.15 \leq x \leq 0.4$ koexistierende Phasen vom Typ kubischer Perovskit Wolframbronzen (PTB_c), tetragonaler Wolframbronzen (TTB) und tetragonaler Perovskit Wolframbronzen (PTB_t), deren Anteile quantifiziert wurden. Für $x = 0.1$ erscheint einphasiges PTB_t , bzw. für $x = 0.05$ eine Perovskit Wolframbronze orthorhombischer Symmetrie (PTB_o). Strukturuntersuchungen an Na_xWO_3 des PTB_c Typs zeigen für alle Zusammensetzungen von 0.4 bis 0.9, dass einheitlich die Raumgruppe Im-3 für die Verfeinerung benutzt werden kann. Die lineare Zunahme der Gitterparameter mit zunehmendem x wird durch die Zunahme der W-O Bindungslänge erklärt, wobei von einem x unabhängigen „tilt“ der WO_6 Oktaeder von ca 3° ausgegangen wird. Für PTB_t wird gezeigt, dass ein „puckering“, d. h. ein „off centering“ der W-Atome parallel zur c -Achse, ungenügend ist, die Struktur zu erklären. Hinzu kommt ein „tilt“ der WO_6 -Oktaeder um die c -Achse, konsistent mit der Raumgruppe P4/ncc .

Die optischen Eigenschaften der metallischen Zusammensetzungen der Systeme Li_xWO_3 , Na_xWO_3 , K_xWO_3 , Cs_xWO_3 , $\text{Na}_x\text{Nb}_y\text{W}_{1-y}\text{O}_3$, and $\text{K}_x\text{Nb}_y\text{W}_{1-y}\text{O}_3$ zeigen, dass die optischen Plasmakanten systematisch als Funktion von x und y verschieben, was eine Abschätzung des Dotiereffektes und des Pleochroismus ermöglicht. Eine Beschreibung dieser Eigenschaften mittels des Drude-Modells freier Elektronen erscheint jedoch nicht ausreichend. Anstelle dessen können die optischen Spektren mittels einer Oszillatorfunktion mit einer transversal optischen Mode bei 2000 cm^{-1} und einer großen Oszillatorstärke, zusätzlich zu einer Drude

Funktion freier Elektronen, beschrieben werden kann. Eine ähnliche Quantifizierung der optischen Eigenschaften wird für $\text{Nb}_{18-x}\text{W}_{9+x}\text{O}_{69}$ Block Typ Verbindungen erhalten. Es wird geschlossen, dass das Feynman-Polaron Modell, das einen Oszillator-Effekt für die internen Anregungen der Polaronen und einen Drude Term für den Polaron „Drift-Beitrag“ beinhaltet, einheitlich die optischen Eigenschaften der metallischen Proben beschreiben kann.

Schlagwörter: Alkali metal Wolframbronzen, Optische Eigenschaften, Polaron.

LIST OF CONTENTS	P
ABSTRACT	i
1. INTRODUCTION	01
2. STRUCTURAL DESCRIPTION OF THE INVESTIGATED SAMPLES	06
3. EXPERIMENTAL	12
3.1 Sample preparation	12
3.2 Sample characterization methods	14
3.3 Data evaluation of single crystal reflectivity spectra	16
4. RESULTS	19
4.1 Characterization of Na_xWO_3 system	19
4.1.1 Samples prepared by isothermal condition	19
4.1.2 Samples prepared by chemical transport method	33
4.2 Characterization of $(\text{Na}_x\text{Li}_{1-x})_{0.45}\text{WO}_3$ system	38
4.3 Characterization of $\text{Na}_{0.8}\text{Nb}_y\text{W}_{1-y}\text{O}_3$ system	39
4.4 Characterization of $\text{Na}_{0.6}\text{Nb}_y\text{W}_{1-y}\text{O}_3$ system	47
4.5 Characterization of $\text{K}_{0.55}\text{Nb}_y\text{W}_{1-y}\text{O}_3$ system	49
4.6 Polarized micro-reflectivity of HTB M_xWO_3 single crystals ($\text{M} = \text{K}, \text{Cs}$ and $x = 0.20, 0.25$) and Kramers-Kronig analysis	60
4.7 Micro-reflectivity of metallic Li_xWO_3 single crystals ($x = 0.45 - 0.35$) and Kramers-Kronig analysis	65
4.8 Polarized micro-reflectivity of $\text{Nb}_{18-x}\text{W}_{8+x}\text{O}_{69}$ ($x = 0, 2, \dots, 9$) with block type structure and Kramers-Kronig analysis	67
5. DISCUSSION	72
5.1 Structural details concerning Na_xWO_3 and Li_xWO_3 systems	72
5.2 Discussion of the optical properties of alkali metal tungsten bronzes	78
5.3 Discussion of the optical properties of Nb-W oxides with block type structure	87
6. SUMMARY	90
7. REFERENCES	92

1. INTRODUCTION

The structure and properties like color and conductivity in tungsten oxides can largely be varied with oxygen deficiency or incorporation of foreign ion or partial substitution of tungsten by similar elements (e.g. Nb, Ta etc.). This has made the system practically important (e.g. electrochromic devices) and also for the understanding of basic phenomena such as superconductivity, metal to non-metal transition. Tungsten trioxide, WO_3 , is basically the host structure of these materials. Without doping or oxygen deficiencies, it is an insulator with a band gap of about 3 eV. Structural changes of WO_3 occur with both temperature and pressure, possessing at least six structural modifications (Aird *et al.*, 2000). Systematic incorporation of foreign ions (e.g., alkali metal ions, rare-earth ions, etc) also lead to systematic structural changes. An aristotype cubic phase of WO_3 (space group Pm-3m) has never been observed at room temperature, but such an hypothetical structure is taken into account to describe all actual structures of WO_3 and also those of the derivatives (Salje, 1976; Vogt *et al.*, 1999; Locherer *et al.*, 1999; Howard *et al.*, 2002). The derivatives of WO_3 having the general formula M_xWO_3 are called as tungsten bronzes. The name “tungsten bronzes” was applied only because of their metallic lustre, but they are neither alloys nor intermetallic compounds. M_xWO_3 are non-stoichiometric compounds and M can be electropositive elements and the value of x can be varied from 0 to 1.

Investigations of tungsten bronzes have a long history of about two hundred years. After discovery of sodium tungsten bronze, Na_xWO_3 , (Wöhler, 1823) other alkali metal tungsten bronzes have also been reported (Laurent, 1838; Hallopeau, 1900; Schäfer, 1903; Brunner, 1903). The tungsten bronzes, however, regarded as stoichiometric compounds until 1935 when Hägg (1935) showed that the sodium bronzes of cubic symmetry belong to a continuous series of solid solutions, Na_xWO_3 of variable composition within an extended homogeneity range $0.32 \leq x \leq 0.93$. Magnéli and Blomberg (1951) reported the presence of such solid solution in other alkali metal tungsten bronzes, too. In the past years an enormous amount of data was accumulated on their crystal structure (Shanks, 1972; Hussain, 1978; Ekstrom and Tilley, 1980; Labbe, 1992), electronic and magnetic properties (Sienko *et al.*, 1963; Stanley *et al.*, 1979; Aristimuno *et al.*, 1980), electrochromic property (Granqvist, 2000), superconductivity (Raub *et al.*, 1964; Skokan *et al.*, 1979; Cadwell *et al.*, 1980; Reich *et al.*, 2000; Leitus *et al.*, 2002). The general formula M_xWO_3 (M = alkali metal) can be formally written as $\text{M}_x(\text{W}_x^{5+}\text{W}_{1-x}^{6+})\text{O}_3$, which indicates the presence of pentavalent tungsten in the bronzes. This assumption is supported by Yang *et al.* (2003) and Gu *et al.* (2006) who investigated the TTB (tetragonal

tungsten bronze) and HTB (hexagonal tungsten bronze) phases of K_xWO_3 by XPS spectroscopy and reported only the presence of W^{5+} and W^{6+} states of W. It has been reported (Weller *et al.*, 1970; Miyamoto *et al.*, 1983; Dubson *et al.*, 1985) that pentavalent tungsten ions can be partially replaced by other pentavalent ions of suitable sizes such as Nb^{5+} and Ta^{5+} , which results in a decrease of the electrical conductivity due to the d^0 character of Nb^{5+} and Ta^{5+} . Weller *et al.* (1970) obtained a substitution up to about 10% of niobium and tantalum in sodium tungsten bronzes by electrolytic reduction method. Miyamoto *et al.* (1983) synthesized a series of niobium containing solid solution, $NaNb_{1-y}W_yO_3$, at high temperature (1550°C) and high pressure (6 GPa) and could observe the formation of cubic phases of compositions $y \approx 0.16$ and for $0.52 \leq y \leq 1$. Dubson *et al.* (1985) prepared tantalum substituted sodium tungsten bronzes, $Na_xTa_yW_{1-y}O_3$, by electrolytic reduction method. Hussain *et al.* (2002) synthesized niobium substituted hexagonal rubidium tungsten bronze and hexagonal potassium tungsten bronze. Recently, Dey (2004) worked on niobium substituted Li- and Cs-tungsten bronzes. In this work attempts were taken to synthesize Nb substituted cubic perovskite sodium tungsten bronzes, and tetragonal potassium tungsten bronzes (TTB). The mother system Na_xWO_3 has also been rechecked to get better composition-structure relationship.

The “fully oxidized” phases analogous to bronzes are termed as “Bronzoids” (Kihlberg *et al.*, 1982) and this type of compound was reported by Galasso *et al.* (1959). There are reports of substitution of the pentavalent tungsten atoms by other pentavalent atoms such as Nb or Ta (Deschanvres *et al.*, 1968; Sharma, 1981 and 1985; Klimova *et al.*, 1995) in bronzoids. Not only pentavalent but also lower valent metal can be substituted for pentavalent tungsten according to the general formula $M_x(T^u_y W^{6+}_{1-y}O_3)$ where M = alkali metal atoms, u = oxidation state of T and $y = x/(6-u)$ for fully oxidized phases. It has been reported (Sabatier and Baud, 1972 and references therein) that monovalent (Li), divalent (Mg), trivalent (Cr), tetravalent (Ti), and hexavalent (Mo) can also partly replace tungsten in appropriate amount so that the resulted compounds are completely oxidized.

The tungsten bronzes and bronzoids contain still unexplained informations about the interplay of very basic phenomena like structural variation, electronic band structure formation, magnetism and superconductivity, and their fine tuning depending on compositions. Therefore it has been a central aim of this work to study the chemical composition, structure and optical property relationship of tungsten bronze systems. Depending on the types and amount of the incorporated metal ions, these materials display a large variety in structure types and electronic properties. To understand the nature of doped electrons in these systems a key question is

related with the interaction between electron and lattice vibration. Thus, another aim of this study is to obtain a better understanding of the optical properties of these systems.

The color change in $M_x\text{WO}_3$ with the increase in alkali ions was investigated more than half a century ago by many groups starting with Glemser *et al.* (1943). The sodium tungsten bronze, Na_xWO_3 ($0 < x < 1$), exhibits most colors of the visible spectrum on varying Na content. Because of their strong variation in colors with varying alkali metal content all known bronzes attracted many scientists to investigate the optical properties and to understand the mechanism of color variation. Brown *et al.* (1954) studied optical reflectivity on cubic Na_xWO_3 system where they measured the diffuse reflectivity of the compressed, powder sodium tungsten bronzes and calculated the absorption spectra ($\% A = 100 - \% R$) between 335 and 1250 nm. Two points of interest are apparent from their study: (i) a linear shift ($\lambda (\text{\AA}) = -3387x + 7488$, λ is the position of the absorption peak at composition x) of absorption peak to low wave lengths with increasing sodium content, and (ii) the width of the peaks increases with decreasing sodium content. Brown *et al.* (1954) argued that the reflectance from powdered samples is too complex to be simply related to their metallic behavior. Dickens *et al.* (1968) also measured the diffuse reflectivity of compressed powder samples using both pure bronze and bronzes mixed with powdered MgO and KCl before compacting, and showed qualitatively similar results with those of Brown and Banks (1954). However, such spectra are not adaptable to the usual Kramers-Kronig analysis as for specular reflectance. Therefore real and imaginary part of the dielectric function is not easy to separate for powder reflectivity data.

King *et al.* (1972) measured the reflectivity of hexagonal tungsten bronzes (HTB) of Rb_xWO_3 system at 4.2 K and described the spectrum by Drude free carrier model. Lynch *et al.* (1973) measured the optical reflectivity of cubic perovskite tungsten bronzes (PTB_c) of Na_xWO_3 system, and tetragonal tungsten bronzes (TTB) of K_xWO_3 system at 4.2 K in the energy range of 0.1 to 38 eV, and analyzed the reflectivity curves by Kramers-Kronig analysis method to get optical dielectric functions. They interpreted the optical constants based on the band structure of ReO_3 . A remarkable work on Na_xWO_3 was done by Owen *et al.* (1978) who measured directly the optical dielectric functions of single crystal (cubic) system by a polarization-modulation ellipsometric technique. The data evaluation given by Owen *et al.* (1978) indicates a deviation from Drude free carrier type behavior. Hussain *et al.* (1997) investigated the anisotropic optical reflectivity of HTB phases of K_xWO_3 , Rb_xWO_3 , Cs_xWO_3 , and TTB K_xWO_3 systems at room temperature. The authors explained the spectra using Drude free carrier model. An exclusion from Drude free carrier type behavior was reported for the spectra of K-HTB system using

alternatively a Lorentz oscillator function for the fit of the spectra. However, an interpretation of such a deviation from the Drude free carrier effect was not given. By high-energy electron-energy-loss spectroscopy (EELS) in transmission, Kielwein *et al.* (1995) showed that electron effective mass (m^*) increases linearly with increasing Na content in $\text{PTB}_c \text{Na}_x\text{WO}_3$. From this findings they proposed narrowing of conduction band due to admixture of 3s states of Na and 2p states of O. Raj *et al.* (2005 and 2006) investigated the electronic structure of Na_xWO_3 of both metallic ($x = 0.3, 0.58, 0.65, 0.7$, and 0.8) and non-metallic ($x = 0.025$) region by high-resolution angle-resolved photoemission spectroscopy (HR-ARPES). These authors noted that a feature at about 2.5 eV survive in the metallic regime, which could be related to the polaron formation. Recently, it has been questioned where the Drude free carrier model could really be appropriate to describe the optical properties of metallic Li_xWO_3 (PTB_c) or if for example a gas of polarons could be more suitable to be considered (Rüscher *et al.*, 2008).

A “polaron” is a quasi-particle in which the phonon and electron degrees of freedom are coupled. The presence of an electron is associated to a finite lattice distortion, which in turn binds the electron leading to the so-called self-trapping effect. The polaron effect is thus an extension to the Bloch wave function of an electron in an undistorted periodic lattice. Historically self-trapping effect has first been noted by Landau (1933). A development of this idea to the polaron concepts (large, intermediate, small) can be traced back to the works of Landau and Pekar (1946), Fröhlich, Pelzer and Zienau (1950), Holstein (1959), Feynman, Hellwarth, Iddings and Platzman (1962), and Austin and Mott (1969). An overview of detailed aspects of the understanding of polaron formation has been given by the various contributions in the conference proceedings on “Polarons in ionic crystals and polar semiconductors” edited by Devreese (1972), “Polarons and excitons in polar semiconductors and ionic crystals” edited by Devreese and Peeters (1982). The importance of the polaron effect for a better understanding of the propagation of electron and hole like charge carriers in solids becomes very clear, however, systems to which polaron theory has been applied or the polaron state has been experimentally proofed like those as the halide systems seems to be limited (e.g. Hirano, 1987). Polarons also tend to create pairs called bipolaron. The formation and properties of bipolaron in tungsten oxide based materials has been discussed in the book titled “Polaron and bipolaron in high T_c superconductor and related material” edited by Salje *et al.* (1995).

A key for a better understanding of the polaron effect in particular for highly conducting oxide systems could be related to a better understanding of their optical properties since any effect of electron-phonon coupling should lead to a significant change in the joint density of states

depending on the coupling strength compared to the free carrier behaviour. The strong increase in the optical absorption peak at about 1 eV in WO_{3-x} (Salje and Güttler, 1984) is related to the increase in polaron concentration. Thereby the electrical conductivity in WO_{3-x} changes from semiconducting to metallic type behavior for $x > 0.1$, which has been explained by an Anderson type insulator to metal transition. Similar effects were observed for the niobium oxides ($\text{NbO}_{2.5-x}$) and niobium tungsten oxides $\text{Nb}_{18-x}\text{W}_{9+x}\text{O}_{69}$ ($x = 0 - 9$) with block type structure depending on the degree of reduction (Rüscher *et al.*, 1988a and 1988b). With the increase in carrier concentration the near infrared reflectivity changes from polaron absorption to a free carrier plasma edge like appearance. Therefore, it was interesting to reinvestigate the optical properties in particular of changes in optical properties at the non-metal to metal transition as for example for the $\text{Nb}_{18-x}\text{W}_{9+x}\text{O}_{69}$ system.

2. STRUCTURAL DESCRIPTION OF THE INVESTIGATED SYSTEMS

Several different crystal structures of alkali metal tungsten bronzes, M_xWO_3 have been identified (Magnéli, 1949, 1951, and 1953; Dickens *et al.*, 1968). Each structure is based upon a network of corner bonded WO_6 octahedra, which form channels into which the alkali metal ions are inserted. The size and concentration of the M ions play major roles of forming different types of tungsten bronze structures. In the following the different structure types of tungsten bronzes and niobium tungsten oxides (block type structure) relevant to this work will be described.

Perovskite tungsten bronze (PTB)

The structure of tungsten bronzes, M_xWO_3 , of perovskite (ABO_3) type but with the partially occupied of A sites by the alkali metal atom M, was determined by Hägg (1935). It can be regarded as comprising of four-membered rings of WO_6 octahedra sharing corner to form tunnels of square cross-sections which contain the M atoms. The PTB structure permits only atoms with maximum radius of 1.3Å at normal pressure. Thus, among the alkali metals only Li and Na are permitted. Perovskite tungsten bronzes, PTB can be further classified into mainly PTB_o (orthorhombic perovskite tungsten bronze), PTB_t (tetragonal perovskite tungsten bronze), and PTB_c (cubic perovskite tungsten bronze) (Ribnick *et al.*, 1963), are shown in Fig. 1(a), (b) and (c), respectively. For example, Li_xWO_3 and Na_xWO_3 form all these types of PTBs but in different region of x e.g., for Na_xWO_3 system: $0.03 \leq x \leq 0.04$ (PTB_o , 298K, pure phase), $0.07 \leq x \leq 0.11$ (PTB_t , 298K, pure phase), and $x \geq 0.43$ (PTB_c , 298K, pure phase), respectively (Ribnick *et al.*, 1963).

The structures of all perovskite tungsten bronzes can be explained by considering three different types of distortion: (i) distortions of the WO_6 octahedral units, (ii) W-displacements within these octahedra, and (iii) the tilting of the corner-linked octahedral units relative to one another. The tetragonal structure (PTB_t) with $P4/nmm$ symmetry differs from the cubic aristotype ($Pm-3m$) by displacements of the W atoms, alternatively parallel and anti-parallel to the z-axis. This antiferroelectric pattern of cation displacements seems to be preserved in the low-symmetry structures (e.g., PTB_o), the lower symmetries being associated with tilting of the corner-linked WO_6 octahedral units. The tetragonal structure (PTB_t) with $P4/ncc$ symmetry comprises both antiferroelectric displacements of W and tilting of WO_6 octahedra around z-axis (Fig. 2).

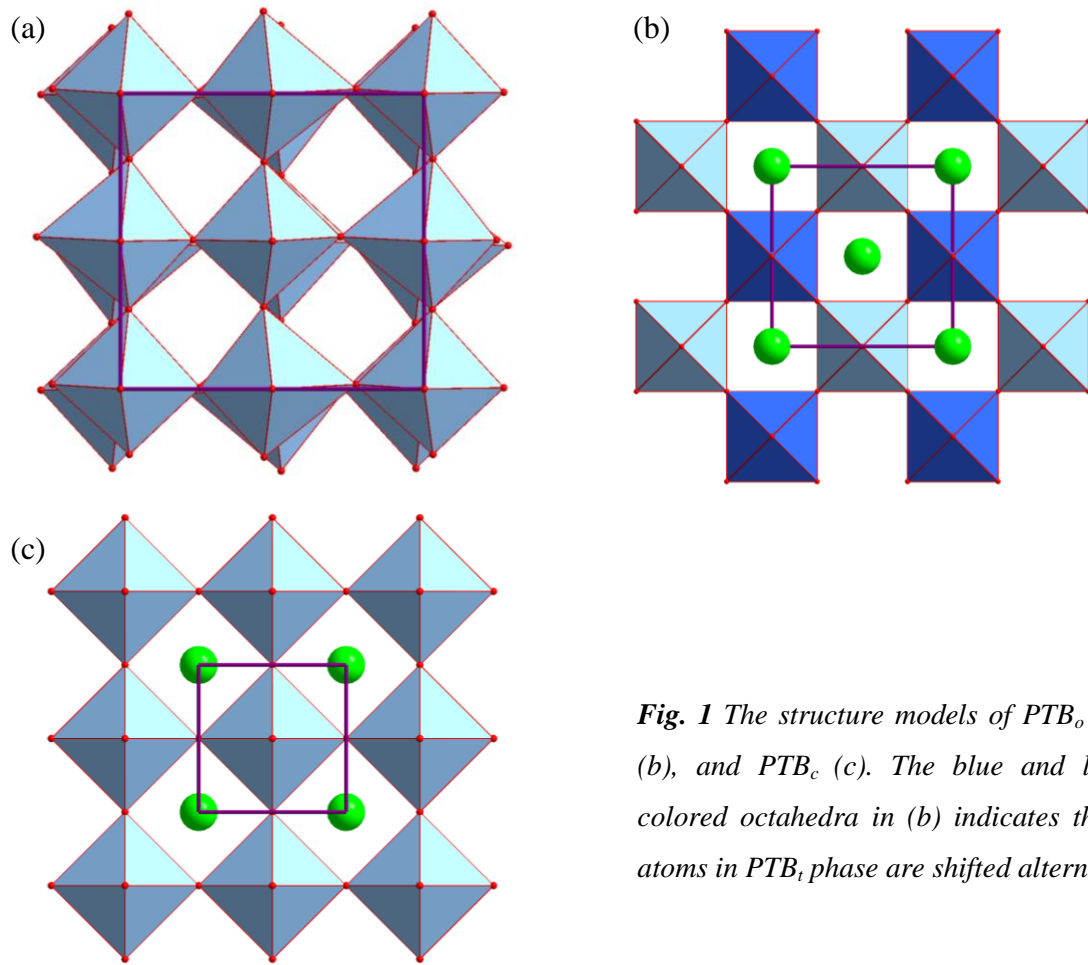


Fig. 1 The structure models of PTB_o (a), PTB_t (b), and PTB_c (c). The blue and light blue colored octahedra in (b) indicates that the W atoms in PTB_t phase are shifted alternatively.

The structure of $PTB_t M_xWO_3$ ($M = Na, Li$) phases was determined by Magnéli (1951) by $P4/nmm$ space group. Rüscher *et al.* (2008) discussed the possibility of $P4/ncc$ space group for $PTB_t Li_xWO_3$ phase.

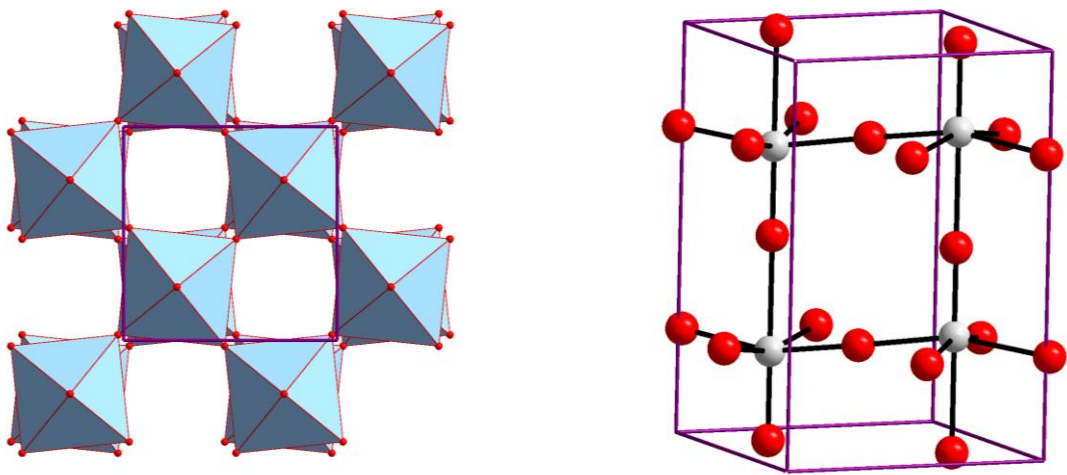


Fig. 2 The structure model of PTB_t phase with $P4/ncc$ symmetry. Both antiferroelectric displacements of W (white balls) and tilting of WO_6 octahedra around z -axis are visualized.

Brown and Banks (1954) refined the lattice parameters of $\text{PTB}_c \text{Na}_x\text{WO}_3$ using space group Pm-3m . Using neutron diffraction data Wiseman *et al.* (1976) have shown that the structure belongs to the space group Im-3 due to successive rotations about three WO_6 rows parallel to $[100]$, $[010]$ and $[001]$ (Fig. 3).

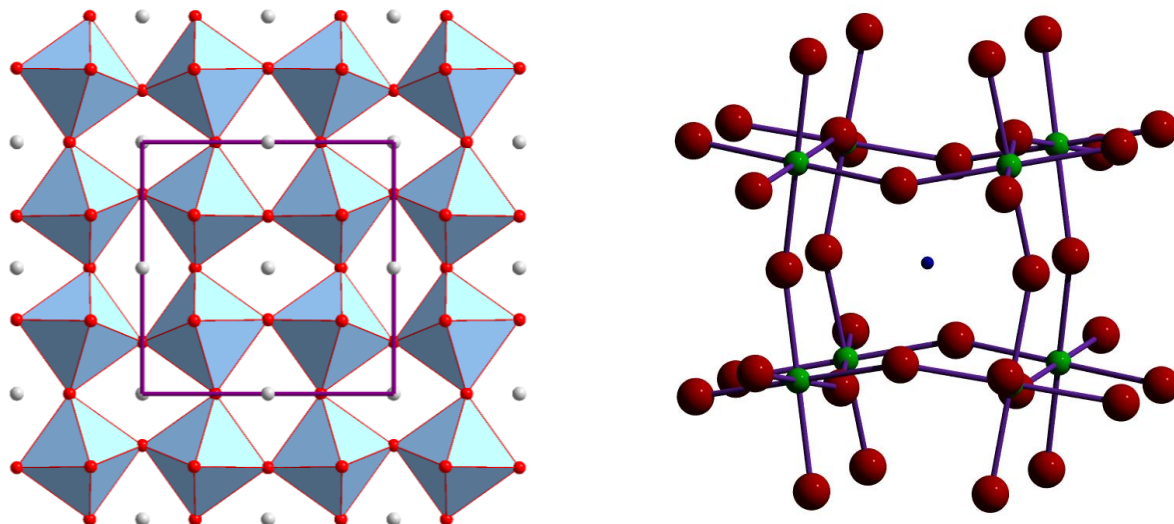


Fig. 3 The structure model of PTB_c with Im-3 symmetry obtained from asitotype Pm-3m structure after successive rotations about three WO_6 rows parallel to $[100]$, $[010]$ and $[001]$.

Tetragonal tungsten bronzes (TTB)

Among the alkali metals only sodium and potassium form a non-perovskite type tetragonal tungsten bronzes (TTB) which consists of corner sharing of WO_6 octahedra forming three types of tunnels, namely trigonal, tetragonal and pentagonal (Fig. 4). The M ions can be located either in the tetragonal or pentagonal or both tunnels, but most of the metal ions show a preference for the larger size pentavalent tunnels. The structure of tetragonal tungsten bronzes (TTB) was determined by Magnéli (1949) for K_xWO_3 ($x = 0.4 - 0.6$). In the potassium TTB the tungsten atoms and K atoms are located in the same plane. In a structural study of $\text{K}_{0.37}\text{WO}_3$ Kihlborg and Klug (1973) reported that about 88 % of the potassium ions were located in the pentagonal tunnels and only about 10% were found in the tetragonal tunnels. When all the tetragonal and pentagonal tunnels are occupied by the potassium ions, this corresponds to the $\text{K}_{0.6}\text{WO}_3$ composition. Takusagawa and Jacobson (1976) discussed the crystal structure of Na-TTB with composition $\text{Na}_{0.33}\text{WO}_3$ and $\text{Na}_{0.48}\text{WO}_3$ and reported that in $\text{Na}_{0.48}\text{WO}_3$ all the pentagonal tunnels are completely filled and only 40% of the tetragonal tunnels were occupied. Thus with increasing the alkali metal content the pentagonal tunnels are filled first and then tetragonal tunnels. This may be due to the fact that the pentagonal tunnels have more available space than

those of tetragonal tunnels and therefore large cation favors the pentagonal tunnels first. The authors (Takusagawa *et al.*, 1976) also reported that the crystal structure of $\text{Na}_{0.33}\text{WO}_3$ is more distorted than that one of $\text{Na}_{0.48}\text{WO}_3$.

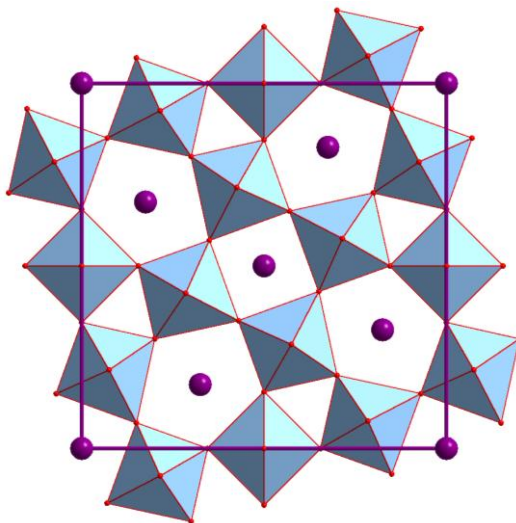


Fig. 4 The structure model of tetragonal tungsten bronze (TTB). The alkali metal atoms occupy pentagonal and tetragonal tunnel sites indicated by big balls.

Hexagonal tungsten bronzes (HTB)

The hexagonal tungsten bronze (HTB) was reported by Magnéli (1953) for potassium, rubidium and cesium tungsten bronzes. The crystal structure of HTB M_xWO_3 consists of layers made up of WO_6 octahedra joined at the corners to form a pattern of three and six membered rings (Fig. 5).

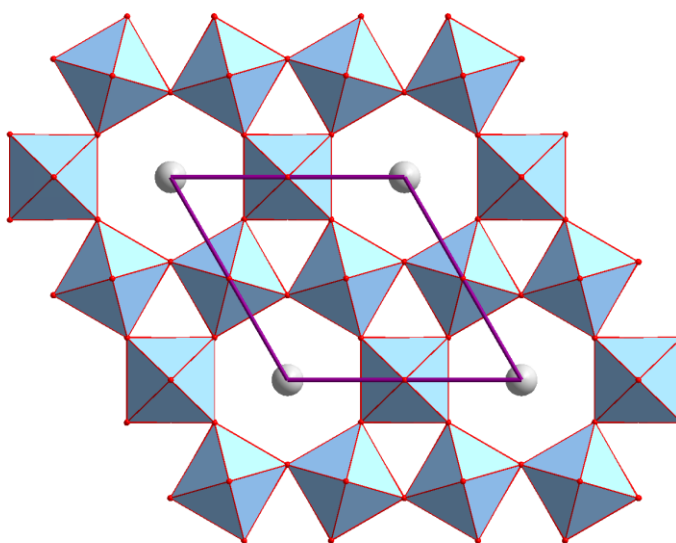


Fig. 5 The structure model of hexagonal tungsten bronze (HTB). The alkali metal atoms are situated in the hexagonal tunnel sites indicated by big balls.

The layers are connected to adjacent layers by the sharing of oxygen atoms at the octahedra corners. The alkali metal ions are distributed in the channels formed by the six membered rings and lie between the layers in the a-b plane. The hexagonal cage, bound by 18 oxygen atoms has a diameter of about 4 Å. Thus, the HTB structure is stabilized when this cage accommodates atoms of large size, such as alkali metal ions K^+ , Rb^+ or Cs^+ . The upper limit for x in the HTB phase in the formula M_xWO_3 is 0.33 and occurs when all the M sites are occupied.

In HTB structure W atoms are slightly off-centered in regular WO_6 octahedra, with alternates displacement parallel to a or b of W atoms located on a same row along c axis (Magnéli, 1953). Since the displacement is in opposite direction in neighboring layers, the c axis is doubled and the unit cell comprises two layers and the atomic set is compatible with the space group $P6_3/mcm$.

Nb-W oxides with block type structure

Nb_2O_5 / WO_3 form a series of complex shear structures (Gatehouse and Wadsley, 1964; Roth and Wadsley, 1965a, 1965b, 1965c, and 1965d). A complete study of the phase relationships in the system Nb_2O_5 / WO_3 has been conducted by Roth and Waring (1966). A classification of different structure types has been given by Wadsley *et al.* (1970). Since optical properties of the “Block type compounds” have been studied in the present investigation, only their structural description will be given. The structural building of blocks consist of $n \times m \times \infty$ of regularly top shared $[TO_6]$ (T = Nb, W) octahedral units (Fig. 6). The block columns are linked together by edge-shared octahedra yielding two sets of perpendicular “shear planes”. Therefore, ordinary “ ReO_3 ” type structure is observed only within the blocks. i.e., in block type structure the units of ReO_3 are limited by two sets of shear planes arranged in vertical position to each other. This structural building principle has been verified by many groups of authors, especially in the field of high-resolution transmission electron microscopy (HRTEM) studies (Nimmo *et al.*, 1972; Obayashi *et al.*, 1976, Heurung *et al.*, 1980, Groh *et al.*, 1982). The compounds having block type structures exist in the Nb rich part of the system at $Nb_2O_5:WO_3$ ratios of 6:1, 7:3, 8:5, and 9:8. Their formation temperatures, stability limits, and crystallographic data are collected by Hussain *et al.* (1989 and references therein). The limiting value of block type structures in these “fully oxidized” phases is $W/Nb = 0.444$ and $O/\sum M = 2.654$ which is corresponding to a 5×5 block structure. In the system Nb_2O_5/WO_3 block structures with a size of blocks larger than 5×5 are not stable under equilibrium conditions (Hussain *et al.*, 1989). Groh *et al.* (1983a and 1983b) could extend the limiting value of Nb/W ratio for the block structure region using the

formation of thermodynamic solid solution series. Starting from the fully oxidized phases Nb was replaced systematically by W and in this way they prepared four series of “reduced” solid solution series. Within each of these series the initial block size and the ratio $O/\Sigma M$ remained unchanged but the tungsten content given by W/Nb was enhanced significantly. For example, in the $Nb_2O_5:WO_3 = 9:8$ series (5×5 block) the W/Nb ratio increases from 0.444 to 1.346 (Groh *et al.*, 1983b).

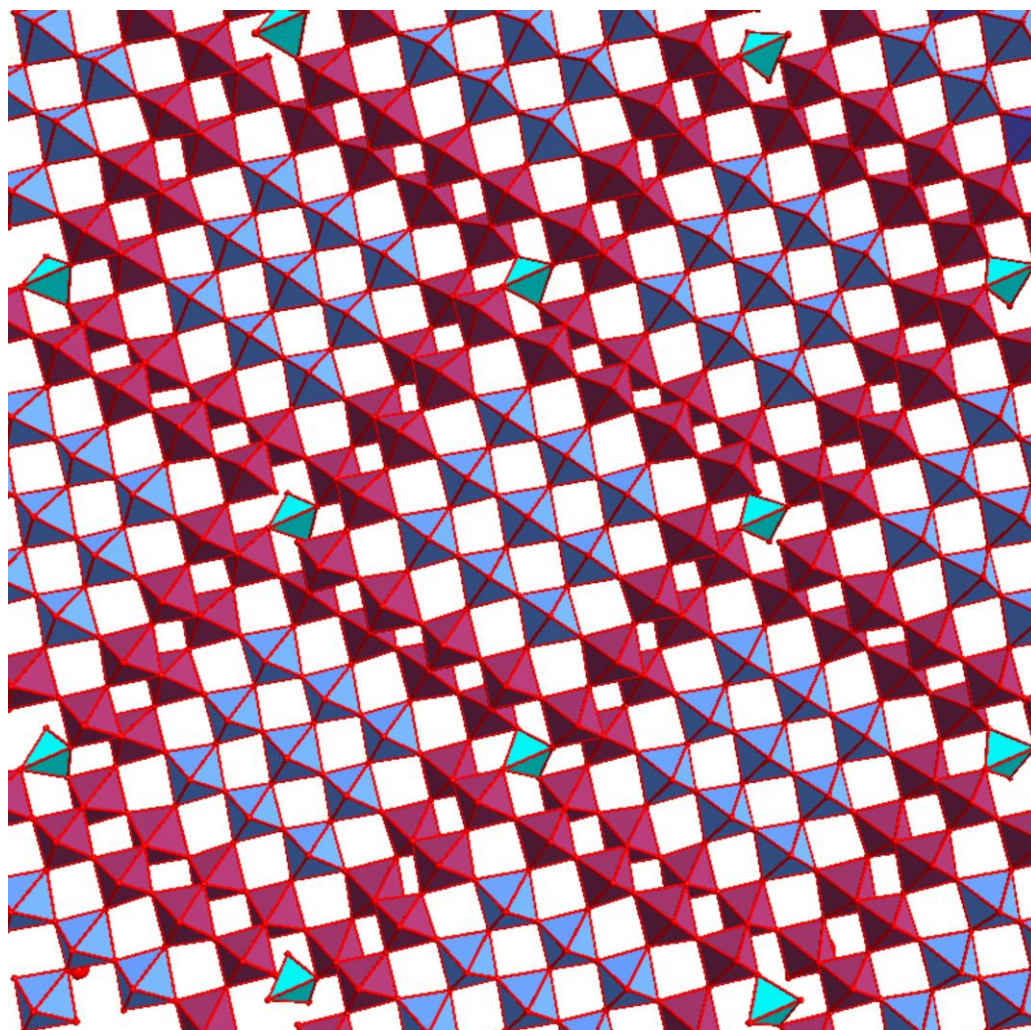


Fig. 6 The model structure of “ 5×5 block” type compounds in projection along the crystallographic y -axis. The “top shared” and “edge shared” octahedral (TO_6 , $T = Nb, W$) are distinguished by blue and red colored octahedra, respectively. The “edge shared” octahedra are shifted by $y = b/2$ ($b =$ one octahedral diameter) against each other and thus forming block columns with different heights of the block planes. Inside the block only “top shared” octahedra exist (i.e. ReO_3 -type structure).

3. EXPERIMENTAL

3.1 Sample preparation

Na_xWO_3 system

Polycrystalline powder materials were prepared by solid state synthesis method. Starting materials were reagent grade (Alfa Aesar) chemicals, $\text{Na}_2\text{WO}_4 \cdot 2\text{H}_2\text{O}$ (99.9%), WO_3 (99.998%), and WO_2 (99.9%). Anhydrous Na_2WO_4 was prepared by heating $\text{Na}_2\text{WO}_4 \cdot 2\text{H}_2\text{O}$ in air at 150°C for 24 hours. WO_3 was preheated for 24 hours in air at 700°C before use. The purity of all reactants was checked before use by taking IR absorption spectra and X-ray powder patterns and checking for a single phase. The reactants were taken with appropriate molar ratio according to Eq. 1.



The reactants were mixed intimately in an agate mortar and transferred into clean, dry silica tubes (6 mm inner diameter and about 100 mm in length), evacuated (0.13 Pa) at room temperature for two hours and then sealed. Series of sample prepared in this way were heated in a Muffle Furnace at a temperature of 600°C for seven days. The ampoules were quenched to room temperature. The picture of an isothermally heated reaction tube is shown in Fig. 7a.

Crystals of sizes up to few hundred micrometers were prepared by chemical vapor transport method using HgCl_2 (99.9995%, Alfa Aesar) as a transporting agent and same reactants as used for the preparation of polycrystalline materials. About 5-10 % (by weight) of HgCl_2 was loaded in the silica tubes (6 mm inner diameter and about 100 mm in length) before evacuation.

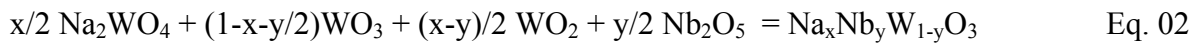


Fig. 7 Pictures of typical reaction tubes: (a) isothermally heated in a Muffle Furnace for the preparation of polycrystalline samples, (b) heated in a double-zoned furnace using temperature gradient for the preparation of big crystals.

The reaction tubes were then heated in a double-zone furnace for about 7 days with a temperature gradient between 700°C for the sink and 800°C for the source side (for details see Hussain et al., 1997). In this way, only PTB_o and PTB_c could be grown as a transported product in the sink side. But TTB crystals were formed in the source side and so in this case HgCl₂ works as a mineralizer. The picture of a typical reaction tube used for chemical transport reaction is shown in Fig. 7b.

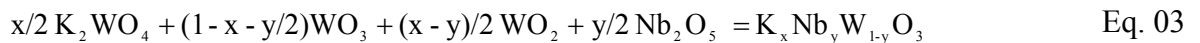
Na_xNb_yW_{1-y}O₃ system

Attempts were made to prepare niobium substituted sodium tungsten bronzes by solid state synthesis method. Starting materials were reagent grade (Alfa Aesar) chemicals, Na₂WO₄·2H₂O (99.9%), WO₃ (99.998%), WO₂ (99.9%) and Nb₂O₅ (99.9985%). Both WO₃ and Nb₂O₅ were heated for 24 hours in air at 700°C before use. Anhydrous Na₂WO₄ was prepared by heating Na₂WO₄·2H₂O in air at 150°C for 24 hours. The reactants were mixed according to Eq. 2 and same procedure was applied as used for the preparation of polycrystalline Na_xWO₃.



K_xNb_yW_{1-y}O₃ system

Samples of nominal composition K_xNb_yW_{1-y}O₃ were taken as prepared by Roy (2007) where the same method of preparation was used as described for the other polycrystalline materials. In this case the reaction temperature was 800°C and starting materials were WO₃ (99.998%), WO₂ (99.9%), Nb₂O₅ (99.9985%) and K₂WO₄. All the reactants except K₂WO₄ were from Alfa Aesar whereas K₂WO₄ was prepared by heating the equimolar mixture of K₂CO₃ (99.95%, Alfa Aesar) and WO₃ at 600°C. Eq. 3 was used to prepare nominal composition K_xNb_yW_{1-y}O₃. KNbWO₆ (pyrochlore type phase) was prepared by heating equimolar mixtures (according to Eq. 4) of K₂WO₄, WO₃ and Nb₂O₅ in air in an open silica glass tube at 800°C for 3 days.



(Na_xLi_{1-x})_{0.45}WO₃ system

Attempts were taken to prepare mixed metal sodium-lithium tungsten bronzes by the same method and conditions used for the preparation of polycrystalline Na_xWO₃. The reactants were mixed according to Eq. 5.



Crystals in Li_xWO_3 , K_xWO_3 , Cs_xWO_3 and Nb-W oxide systems

For these samples published data (Rüscher et al., 2008; Hussain et al., 1997; Rüscher et al., 1993) were used and remeasured in MIR spectral range additionally.

Li_xWO_3 (PTB_c): Single crystal slices were taken from the earlier study (Rüscher et al., 2008), where the crystals were prepared from the appropriate amounts of Li_2WO_4 , WO_3 and WO_2 mixture in a silica glass tube. HgCl_2 was used as a transporting agent. The reaction tubes were heated in a double-zoned furnace for about 5-7 days with a temperature gradient between 700 °C for the sink 800 °C for the source.

K_xWO_3 (HTB) and Cs_xWO_3 (HTB): Single crystal slices were taken from the earlier study (Hussain et al., 1997). The crystals were prepared using appropriate amount of reactants K_2WO_4 , WO_3 and WO_2 (for K_xWO_3), and Cs_2WO_4 , WO_3 and WO_2 (for Cs_xWO_3). The preparation procedure and temperature gradient was almost same as described for Li_xWO_3 system. In this case HgCl_2 / HgBr_2 / HgI_2 was used as a transporting agent.

Nb-W oxide (block type structure, 5×5): Single crystal slices were taken from Rüscher et al. (1993). Appropriate amounts of reactants (Nb_2O_5 , WO_3 , and NbO_2) were mixed, transferred in a dry silica glass tube, evacuated and sealed. HgCl_2 was used as a mineralizer before sealing. The reaction tubes were heated isothermally at 1300 °C for 2-7 days.

3.2 Sample characterization methods

X-ray diffraction method

The products were characterized by X-ray powder patterns recorded in a Stoe Stadi P diffractometer (transmission geometry, $\text{CuK}\alpha_1$ radiation by a focusing Ge (111) monocromator, linear PSD) and in a Bruker D8 diffractometer (transmission geometry, $\text{CuK}\alpha$ radiation) at room temperature (298K). Structure refinements were performed using the Rietveld software Diffrac Plus TOPAS (Bruker AXS, Karlsruhe, Germany). For the calculation of the reflex profiles fundamental parameters were used on the basis of instrumental parameters calculated out of a silicon standard measurement. As an additional general parameter the zero point of the centre was varied and a polarization parameter was fixed. The absolute values of lattice parameter (for single phase samples) were determined by using X-ray powder photographs in a Guinier-Hägg focusing camera ($\text{CuK}\alpha_1$) using Si as internal standard ($a = 5.430879 \text{ \AA}$).

Selected films were read using an automatic film scanner (Johansson et al., 1980) and evaluated with use of computer programs SCANPI and PIRUM (Werner, 1970).

Infrared absorption spectroscopy

For the IR investigation 1mg of the finely ground sample was dispersed into 199 mg potassium bromide (KBr) and pressed into pellet (13 mm diameter). The spectrum of pure KBr pellet prepared in same way was used as a reference. For most of the samples measurements were done in the range of 230–4000 cm^{-1} (Bruker IFS66v FTIR spectrometer equipped with standard DTGS detector). The absorption spectra of some samples were measured down to 50 cm^{-1} using polyethylene instead of KBr as a reference material. Spectra are given in absorbance units ($-\lg(I/I_0)$, I_0 , I are transmitted intensities through “reference” and “reference + sample”, respectively).

Powder reflectivity

The optical reflectivity was measured in the range of 10000 - 24000 cm^{-1} from the undiluted powders against a suitable reference (KBr or MgO) by using Bruker IFS88 FTIR spectrometer. The optical reflectivity of the series of powder samples were also measured in the range 10000 to 40000 cm^{-1} against MgO as a reference by using a Zeiss-Specord S10 spectrometer.

Optical micrography

For optical microscopy samples were glued to plane sample holder (ordinary glass) and mechanically abraded and finally polished (0.2 μm diamond paste) to show optically high quality surfaces. Optical micrographs were taken in reflection mode using a Leica microscope with an attached CCD camera (Sony).

Raman spectroscopy

Raman spectroscopic measurements were performed on polished samples using a confocal Raman microscope (CRM 200, frequency doubled Nd:YAG laser with maximal power of 20-mW). All spectra were obtained in backscattering geometry using a microscope device that allows the incident light to be focused on the sample as a spot of about 2 μm in diameter.

Single crystal reflectivity

The optical reflectivity of selected crystals slices as well as polished powder samples were measured using an FTIR spectrometer (Bruker IFS88) with an attached microscope IR scope II). An Al-mirror was used for reference measurements. The reflectivity measurements were carried out between 550 cm^{-1} and 18000 cm^{-1} with special detector settings and beam splitters for the ranges 550 to 4000, 3000 to 10000 and 8000 to 18000 cm^{-1} providing a sufficient spectral overlap. A spot size of above $30\text{ }\mu\text{m}$ in diameter and polarized light (only for anisotropic phases) (KRS5 and Glan Thompson polarizer) at nearly normal incidence onto the surfaces were used.

Electron microscopy

The scanning electron microscopy (SEM) images of samples Na_xWO_3 , $(\text{Na}_x\text{Li}_{1-x})_{0.45}\text{WO}_3$, and $\text{K}_x\text{Nb}_y\text{W}_{1-y}\text{O}_3$ were taken in JEOL-6060, where the powders were smeared on adhesive carbon films and mounted on aluminium plates.

Microprobe analysis

The elemental compositions were analyzed with a “Cameca SX100” electron microprobe. Some selected samples from the systems Na_xWO_3 , $\text{Na}_{0.8}\text{Nb}_y\text{W}_{1-y}\text{O}_3$, and $\text{K}_x\text{Nb}_y\text{W}_{1-y}\text{O}_3$ were investigated. For microprobe analysis, polycrystalline samples were glued to plane sample holder (ordinary glass) and mechanically abraded and finally polished ($0.2\text{ }\mu\text{m}$ diamond paste) and coated with a carbon layer. All data were obtained using 15 kV acceleration potential, a static (fixed) beam, $\text{K}\alpha$ emission from sodium, $\text{K}\alpha$ emission from potassium, $\text{L}\alpha$ emission from Nb and $\text{M}\alpha$ emission from tungsten. The standards Nb on metallic Nb, NbO_2 , and Nb_2O_5 ; W on metallic W; Na on albite (composition: O = 48.65%, Na = 8.52%, Al = 10.12%, Si = 31.34%, Ca = 0.45%), and K on orthoclase (composition: O = 46.11%, Na = 0.33%, Al = 9.09%, Si = 30.56%, K = 13.03%, Fe = 0.88%) were used for calibration. The samples were analyzed with a focused beam, 15 nA beam current and counting times of 3 s for each elements. A beam diameter of about 2 - 5 μm was used.

3.3 Data evaluation of single crystal reflectivity spectra

Specular reflectivity spectra contain an interplay of the real and the imaginary parts of the complex dielectric function $\varepsilon^*(\omega) = \varepsilon_1 + i\varepsilon_2$ or complex refractive index $n^*(\omega) = n + ik$. At normal incidence the reflectivity is given by the Fresnel formula (Eq. 6).

$$R = \frac{(n-1)^2 + k^2}{(n+1)^2 + k^2} \quad \text{Eq. 06}$$

It has been shown (Rimmer et al, 1960 and references therein) that the Kramers-Kronig (K-K) relation provides a powerful tool for analyzing the specular reflectivity to obtain $\varepsilon^*(\omega)$ or $n^*(\omega)$. If the reflectivity amplitude is written $re^{i\theta}$, $R = rr^*$, the K-K relation results:

$$\theta(\omega) = \frac{\omega}{\pi} \int_0^\infty \frac{\ln R(\omega_0)}{\omega_0^2 - \omega^2} d\omega_0 \quad \text{Eq. 07}$$

which enables to calculate the real (n) and imaginary part (k) of the refractive index as

$$n = (1-R) / (1+R - 2 R^{1/2} \cos\theta(\omega)) \quad \text{Eq. 08}$$

$$k = (2 R^{1/2} \sin\theta(\omega)) / (1+R - 2 R^{1/2} \cos\theta(\omega)) \quad \text{Eq. 09}$$

The optical and dielectric constants are related as

$$(n-ik) / (n+ik) = R^{1/2} e^{i\theta}, \quad \text{Eq. 10}$$

$$\varepsilon = \varepsilon_1 - i\varepsilon_2 = (n-ik)^2, \quad \text{Eq. 11}$$

$$\varepsilon_1 = n^2 - k^2, \quad \varepsilon_2 = 2nk \quad \text{Eq. 12}$$

Thus by calculating θ and by suitable algebraic manipulations, one can obtain the dielectric constants from the reflectivity data. However, since R is not known over the entire energy spectrum, it is necessary to extrapolate R . One can also use an extrapolation, which will force the optical or dielectric functions to agree with some independent measurement at a particular energy range. For example, ellipsometric measurements on metals will yield ε_1 , ε_2 , or n , k directly.

In the present study the reflectivity spectra were transformed to the real and imaginary part of the complex dielectric function by the Kramers-Kronig transformation using computer program (OPUS).

To explain the reflectivity of metallic samples the classical Drude theory for free electrons was used (Drude, 1900). It accounts for free electrons undergoing scattering, characterized by a constant relaxation frequency (damping constant). The dielectric function for Drude free carrier model can be written as

$$\varepsilon_1 = \varepsilon_\infty (1 - \omega_p^2 / (\omega^2 + \gamma^2)), \quad \text{Eq. 13}$$

$$\varepsilon_2 = \varepsilon_\infty \gamma \omega_p^2 / (\omega (\omega^2 + \gamma^2)) \quad \text{Eq. 14}$$

The wavenumber (ω), screened plasma frequency (ω_p), and damping constant (γ), are given in wavenumber units (cm^{-1}). The “high wavenumber dielectric constant” ϵ_∞ , contains the summed contributions of the valence band electrons.

For the description of phonon peaks or the electronic excitation, the dielectric functions

$$\epsilon_1 = \epsilon_\infty + \sum_i [F_i \omega_i^2 (\omega_i^2 - \omega^2)] / [(\omega_i^2 - \omega^2)^2 + \gamma_i^2 \omega^2] \quad \text{Eq. 15}$$

$$\epsilon_2 = \sum_i [F_i \omega_i^2 \gamma_i \omega] / [(\omega_i^2 - \omega^2)^2 + \gamma_i^2 \omega^2], \quad \text{Eq. 16}$$

were used. Here, F_i = oscillator strength, γ_i = damping constant, and ω_i = oscillator frequency of the i th phonon.

The frequency dependence of the conductivity ($\sigma(\omega)$) is related with the imaginary part of the dielectric function (ϵ_2) according to Eq. 17.

$$\sigma(\omega) \text{ (in } \text{Scm}^{-1}\text{)} = 0.0167 \times \epsilon_2 \times \omega \quad \text{Eq. 17}$$

4. RESULTS

4.1 Characterization of Na_xWO_3 system

4.1.1 Samples prepared by isothermal condition

XRD results

Polycrystalline sodium tungsten bronzes, Na_xWO_3 , were prepared and systematically investigated. The structural information and relative phase contributions of Na_xWO_3 obtained by Rietveld refinement of X-ray diffraction data are listed in Table 1. The samples Na_xWO_3 show pure PTB_0 phase for $x = 0.05$, pure PTB_t phase for $x = 0.10$, a mixture of three phases ($\text{PTB}_t + \text{TTB} + \text{PTB}_c$) for $0.15 \leq x \leq 0.25$, a mixture of two phases ($\text{TTB} + \text{PTB}_c$) for $0.30 \leq x \leq 0.4$, and pure PTB_c phase for $x > 0.4$.

Table 1 List of lattice parameters of polycrystalline Na_xWO_3 series and relative contribution of different phases (according to Rietveld refinement of XRD data).

Nominal composition, x	Crystal structure	Relative contribution / wt %	Space group	Lattice parameter / Å			
				a	$a_c (= a/2)$	b	c
0.05	PTB_0		Pcnb	7.4068 (5)		7.4410(4)	7.7580(4)
0.10	PTB_t		P4/ncc	5.2567(6)		-	7.8085(5)
0.15	PTB_t	71	P4/ncc	5.2595(5)		-	7.8133(8)
	TTB	5	P4/mbm	12.0773(13)		-	3.7535(5)
	PTB_c	24	Im-3	7.5970 (10)	3.7985	-	-
0.20	PTB_t	48	P4/ncc	5.2601(5)		-	7.8139(7)
	TTB	16	P4/mbm	12.0744(4)		-	3.7560(5)
	PTB_c	36	Im-3	7.5968 (7)	3.7984	-	-
0.25	PTB_t	17	P4/ncc	5.2607(6)		-	7.8143(9)
	TTB	36	P4/mbm	12.0705(5)		-	3.7554(8)
	PTB_c	47	Im-3	7.6009 (6)	3.8005	-	-
0.30	TTB	42	P4/mbm	12.0751(4)		-	3.7550(3)
	PTB_c	58	Im-3	7.6049 (5)	3.8025	-	-
0.35	TTB	34	P4/mbm	12.0851(3)		-	3.7551(4)
	PTB_c	66	Im-3	7.6171 (4)	3.8086	-	-
0.40	TTB	3	P4/mbm	12.0982(14)		-	3.7572(5)
	PTB_c	97	Im-3	7.6290 (5)	3.8145	-	-
0.45	PTB_c		Im-3	7.6355 (4)	3.8178	-	-
0.50	PTB_c		Im-3	7.6416 (3)	3.8208	-	-
0.60	PTB_c		Im-3	7.6636 (4)	3.8318	-	-
0.70	PTB_c		Im-3	7.6798 (4)	3.8399	-	-
0.80	PTB_c		Im-3	7.6959 (3)	3.8480	-	-
0.90	$\text{PTB}_c + \Delta$		Im-3	7.7199 (5)	3.8600	-	-

Δ = few lines from impurity phase

PTB₀ pure phase

The sample having nominal composition Na_{0.05}WO₃ shows PTB₀ crystal structure. Fig. 8 shows the X-ray diffraction pattern along with the Rietveld refinement fit using space group Pcbn, which is comparable to the high temperature β phase of WO₃ (Woodward *et al.*, 1997). The atomic coordinates and displacement parameters obtained from Rietveld refinement method are listed in Table 2.

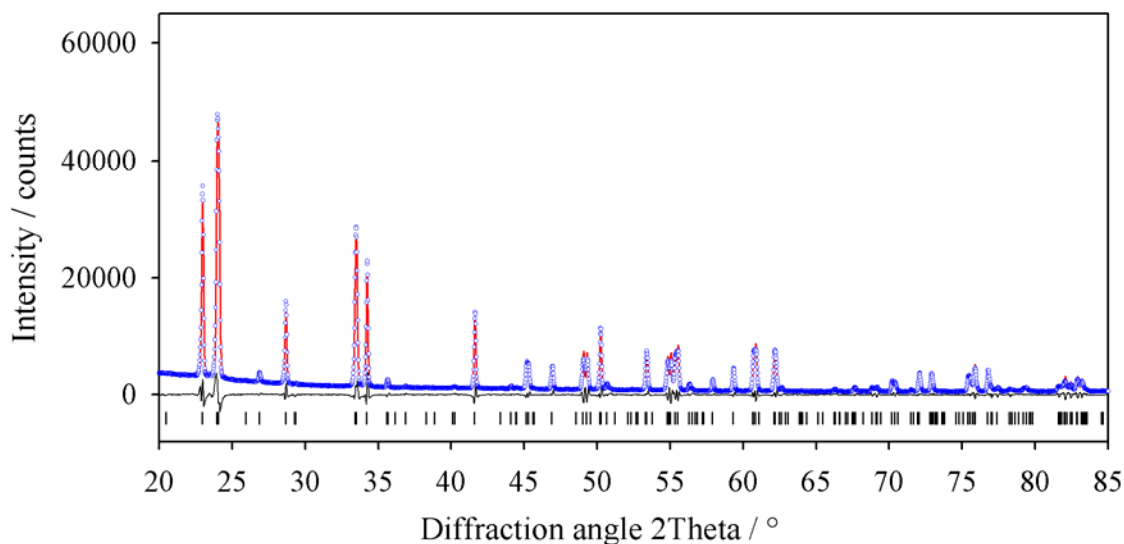


Fig. 8 Rietveld refinement fit for nominal Na_{0.05}WO₃ sample. Blue dots, red line and tick marks represent the observed pattern, the refined pattern and the positions of the refined reflection peaks, respectively. The black line indicates the difference of observed and calculated pattern. Rietveld refinement was done in the range of $2\theta = 20 - 110^\circ$. For the sake of clarity the diffraction pattern is shown only up to $2\theta = 85^\circ$.

Table 2 Atomic coordinates and displacement parameters of nominal Na_{0.05}WO₃. (Space group: Pcbn, $R_{wp} = 11\%$, $Z = 8$). The occupancy factor of Na is constrained to nominal value because of very low amount. The displacement parameter of Na is chosen as an arbitrary constant value of 1.0.

Atom	Site	x	y	z	Occ.	B _{iso}
W	8d	0.2451(3)	0.01509 (16)	0.2844(2)	1	0.82 (2)
O(1)	8d	0.9640 (23)	0.0138 (40)	0.2971 (24)	1	1.5 (3)
O(2)	8d	0.2938 (22)	0.2423 (22)	0.2512 (52)	1	1.5 (3)
O(3)	8d	0.2859 (28)	0.0028 (22)	0.9820 (14)	1	1.5 (3)
Na	4a	1/2	1/4	0	0.05	1.0

PTB_t pure phase

The sample of nominal composition Na_{0.1}WO₃ with the PTB_t phase was refined earlier (Magneli, 1951) using P4/nmm space group. Fig. 9 shows the Rietveld refinement fit for Na_{0.1}WO₃ using P4/ncc space group. There is a small hint for the presence of a reflection in the range between 40 and 41 2theta that can be indexed as 211 diffraction line (Fig. 9 inset), which is inconsistent with the P4/nmm space group but is consistent with the P4/ncc space group. The atomic coordinates and displacement parameters obtained from Rietveld refinement are listed in Table 3.

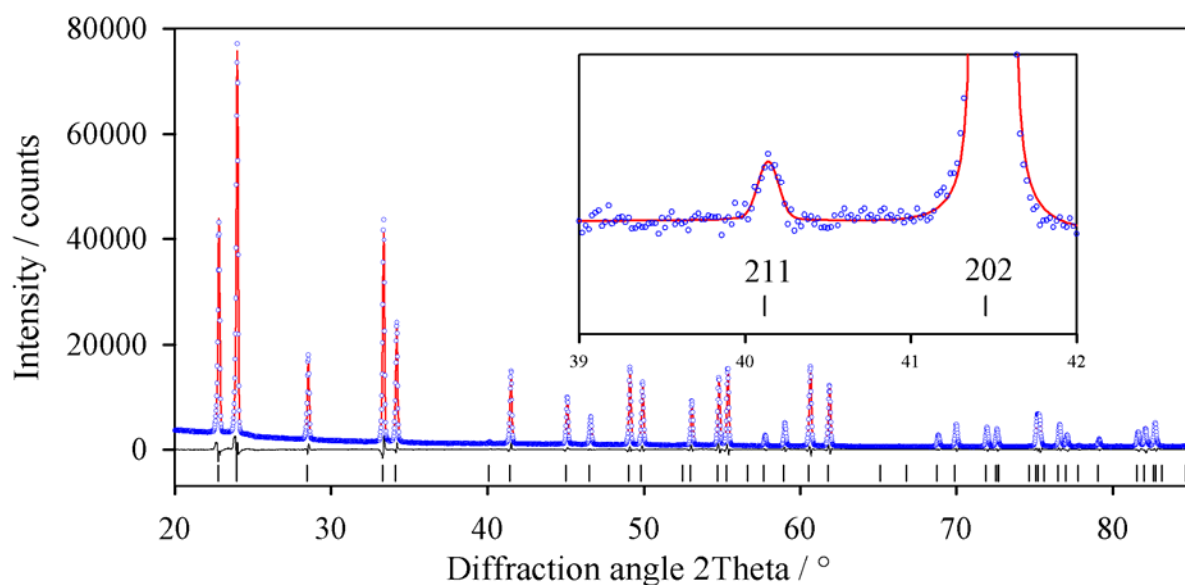


Fig. 9 Rietveld refinement fit for nominal Na_{0.1}WO₃ sample. Blue dots, red line and tick marks represent the observed pattern, the refined pattern and the positions of the refined reflection peaks, respectively. The black line indicates the difference of observed and calculated pattern. Rietveld refinement was done in the range of $2\theta = 20 - 110^\circ$. Inset shows the presence of 211, and 202 diffraction lines of space group P4/ncc.

Table 3 Atomic coordinates and displacement parameters of nominal Na_{0.1}WO₃. (Space group: P4/ncc, $R_{wp} = 7\%$, $Z = 4$)

Atom	Site	x	y	z	Occ.	B _{iso}
W	4c	1/4	1/4	0.2842 (6)	1	0.62 (2)
O(1)	4c	1/4	1/4	0.952 (8)	1	1.4 (4)
O(2)	8f	0.7120 (11)	0.0288 (11)	0.2500	1	1.4 (4)
Na	4a	3/4	0	0	0.12 (4)	2.0 (3)

PTB_c pure phase

The samples with nominal composition $x > 0.4$ show pure cubic phase. Rietveld refinements were carried out using space group Im-3 and the same setting of positional parameters given by Clarke (1977). Fig. 10 shows the Rietveld refinement fit for a typical cubic phase taking Na_{0.45}WO₃ as an example. This setting corresponds to a doubling of unit cell dimension with eight formula units ($z = 8$) per unit cell compared to a primitive unit cell Pm-3m ($z = 1$). This leads to indexing of all diffraction peaks including the weak ones which could not be indexed using Pm-3m as shown in Fig. 10.

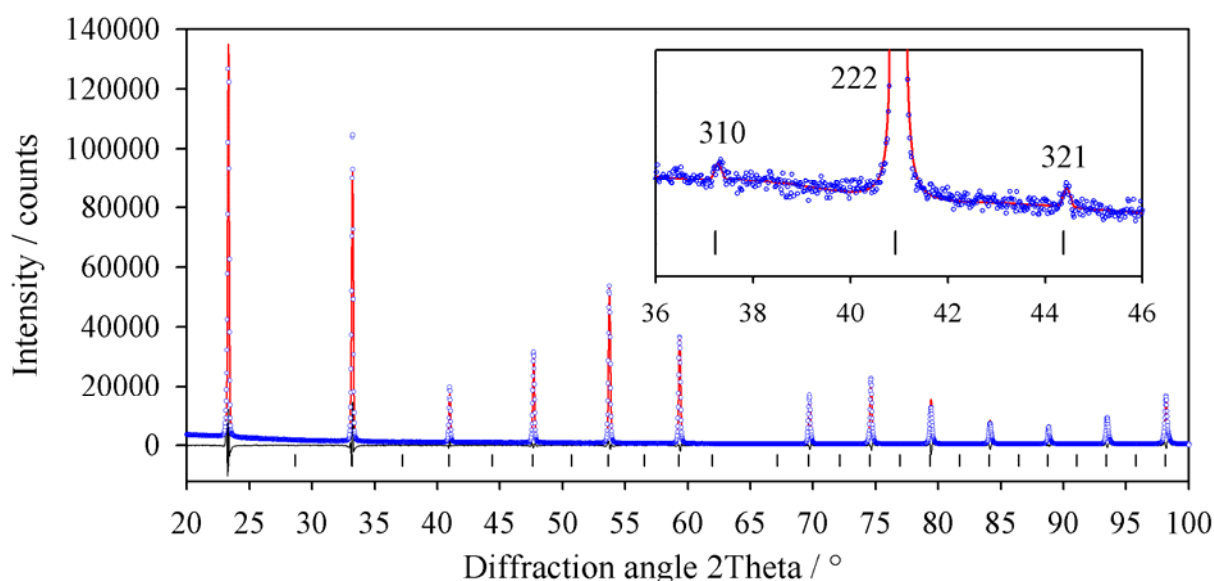


Fig. 10 Rietveld refinement fit for nominal Na_{0.45}WO₃ sample. Blue dots, red line and tick marks represent the observed pattern, the refined pattern and the positions of the refined reflection peaks, respectively. The black line indicates the difference of observed and calculated pattern. Rietveld refinement was done in the range of $2\theta = 20 - 110^\circ$. Inset shows the presence of 310, 222, and 321 diffraction lines of space group Im-3.

The XRD patterns of other PTB_c Na_xWO₃ (i.e., $x = 0.5, 0.6, 0.7, 0.8$, and 0.9) are shown in Fig. 11. The structures were refined using space group Im-3 (calculated patterns are not shown in the figure). The XRD pattern of nominal composition Na_{0.9}WO₃ shows the presence of few additional diffraction lines (marked as star), which can be indexed with the high intensity peaks of WO_{2.92} phase (ICDD-30 1387).

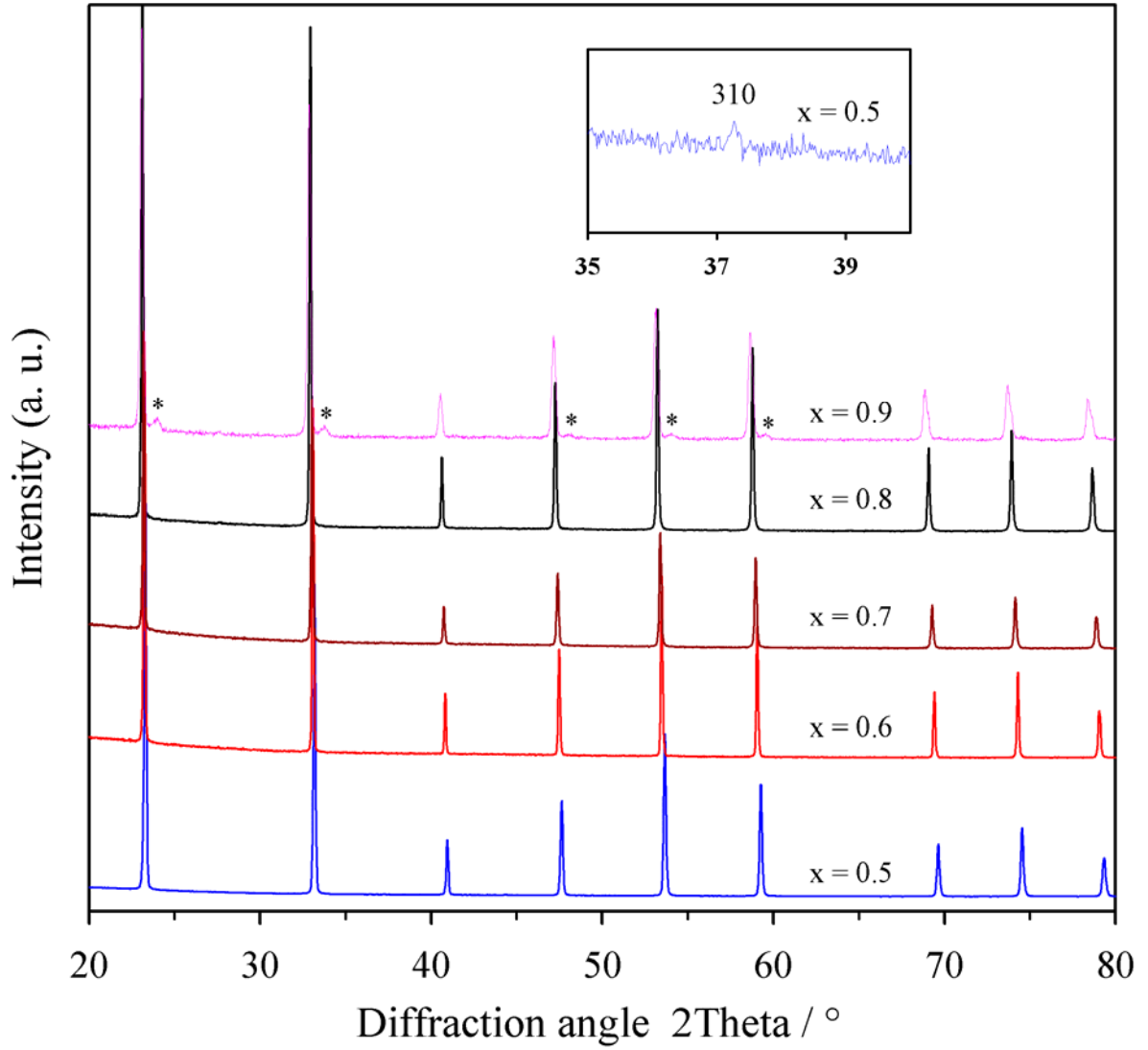


Fig. 11 XRD patterns of Na_xWO_3 samples with nominal composition $x = 0.5, 0.6, 0.7, 0.8$, and 0.9 . The diffractograms are shifted vertically for the sake of clarity. The presence of 310 diffraction line, which consistent with the space group $Im-3$, is shown in inset as an example for $x = 0.5$ composition.

The range of PTB_t , TTB , and PTB_c mixed phases

Na_xWO_3 with nominal compositions $0.15 \leq x \leq 0.40$ show mixture of different phases (PTB_t , TTB and PTB_c). Starting with the lattice parameters and atomic setting used earlier for PTB_t , PTB_c and TTB (will be shown later) phases, Rietveld refinements were done. Fig. 12a, b, and c show the Rietveld refinement fit for nominal composition $x = 0.15, 0.20$ and 0.25 , respectively. Rietveld refinements were done by considering alternatively two phases (PTB_t and TTB) and three phases (PTB_t , TTB and PTB_c) for nominal compositions $0.15 \leq x \leq 0.25$. The difference curve implies a better fit when three phases are considered in refinement (Fig. 13).

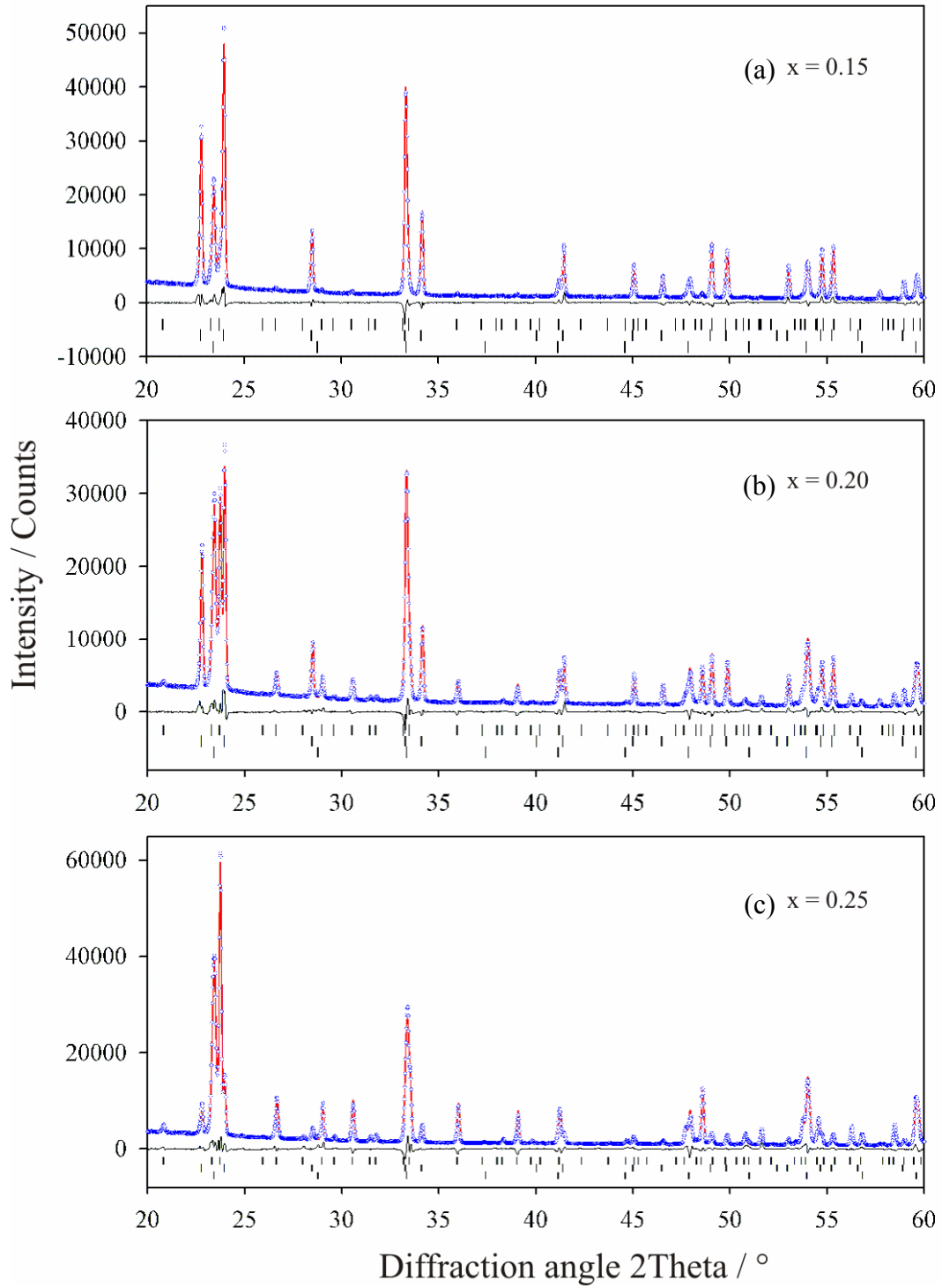


Fig. 12 Rietveld refinement fit for nominal $\text{Na}_{0.15}\text{WO}_3$, $\text{Na}_{0.20}\text{WO}_3$, and $\text{Na}_{0.25}\text{WO}_3$ samples (as denoted). The structure refinements were done considering coexisting phases of PTB_b , TTB and PTB_c . Blue dots, red line, and tick marks represent the observed pattern, the refined pattern and the positions of the refined reflection peaks, respectively. The top, middle and down ticks belong to PTB_b , TTB and PTB_c phase, respectively. The black line indicates the difference of observed and calculated patterns. Rietveld refinement was done in the range of $2\theta = 20 - 110^\circ$.

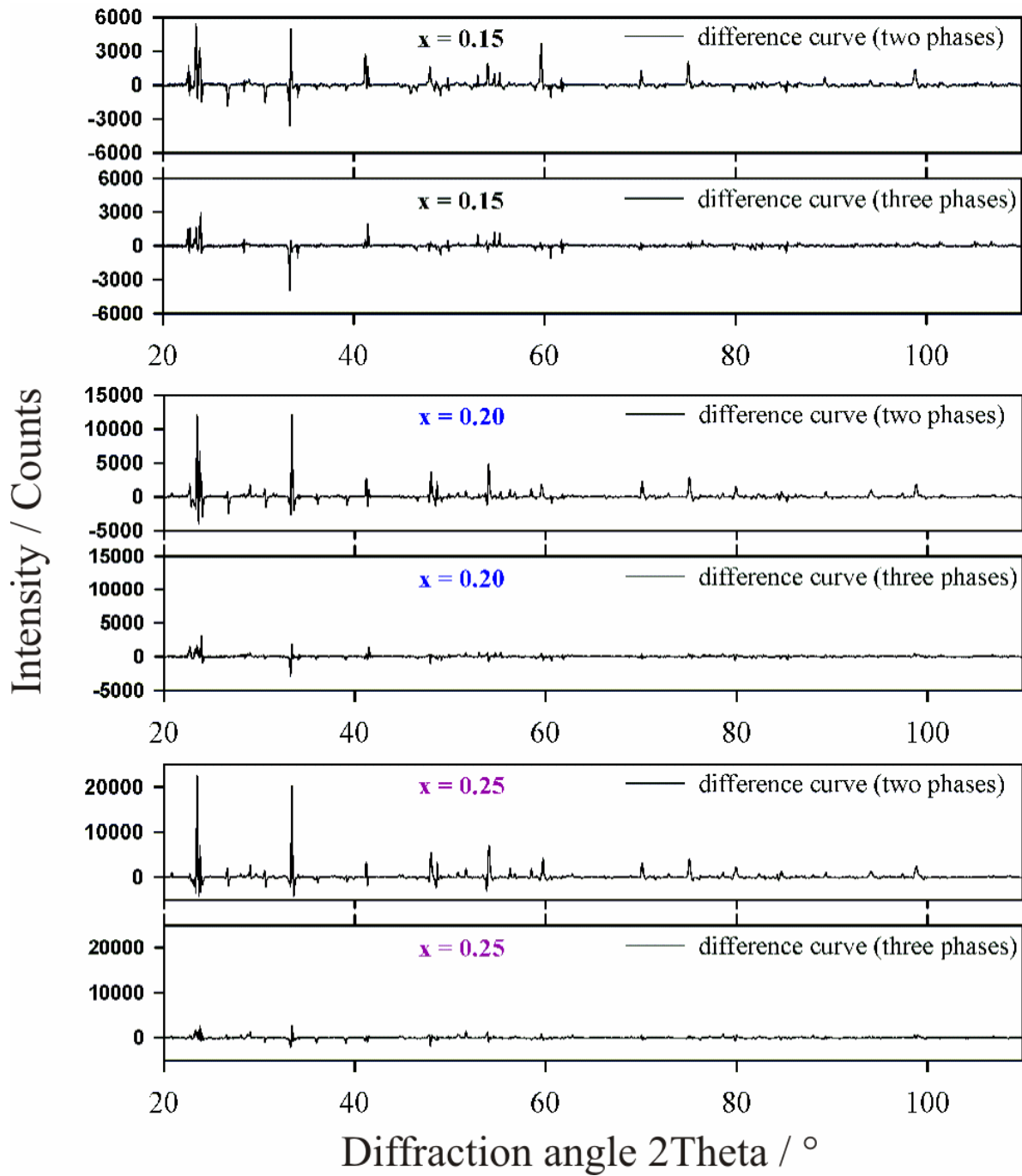


Fig. 13 The differences curves obtained from Rietveld refinement fit for nominal $\text{Na}_{0.15}\text{WO}_3$, $\text{Na}_{0.20}\text{WO}_3$, and $\text{Na}_{0.25}\text{WO}_3$ sample including two and three phases (as denoted).

Fig. 14a, b, and c show the Rietveld refinement for nominal composition $x = 0.30$, 0.35 and 0.40 , respectively. According to refinement results, cubic phase is the dominating phase in this range ($x = 0.30 - 0.40$). The relative phase contribution of different phases is given in Table 1.

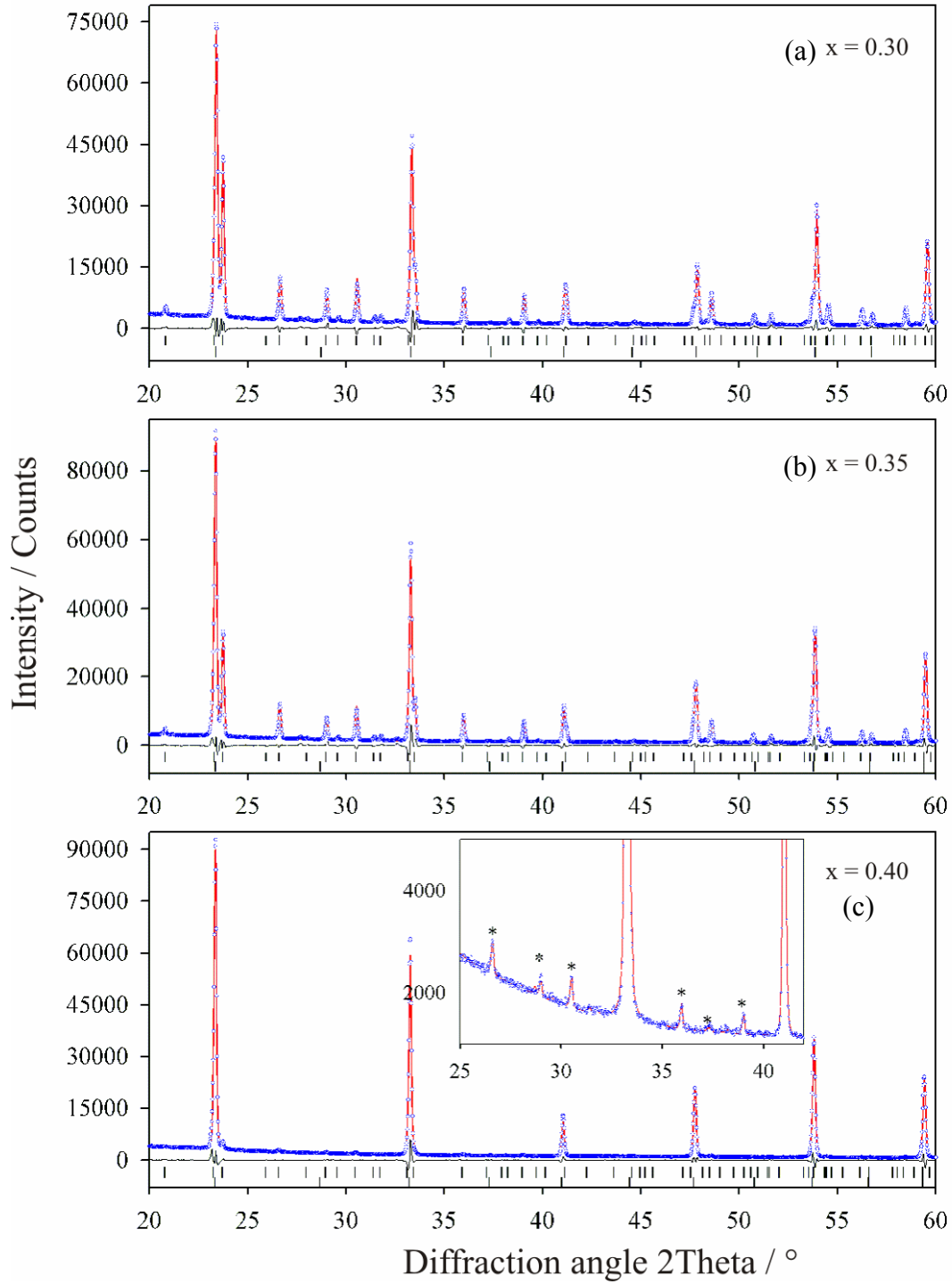


Fig. 14 Rietveld refinement fit for nominal $\text{Na}_{0.3}\text{WO}_3$, $\text{Na}_{0.35}\text{WO}_3$, and $\text{Na}_{0.4}\text{WO}_3$ sample (including two phases). Blue dots, red line and tick marks represent the observed pattern, the refined pattern and the positions of refined reflection peaks respectively. The black line indicates the difference of observed and calculated patterns. Rietveld refinement was done in the range of $2\theta = 20 - 110^\circ$. Inset shows clearly the presence of diffraction line from the TTB phase (c) (marked as star).

The lattice parameters of PTB_t increases slightly up to $x = 0.15$ and no further increase for $x > 0.15$ (Table 1). This increase in lattice parameters could indicate the increase in sodium content.

Although, the PTB_c phase start to form from nominal composition $x = 0.15$, the calculation of sodium content using lattice parameter value and Brown and Bank relation (1954) shows that the composition can be $\text{Na}_{0.2}\text{WO}_3$. For TTB phase mainly the a lattice parameter increases and may be explained by the increase in sodium content in the product, which is similar for PTB_c system. The increase in cell parameter in TTB phase has also been reported for K_xWO_3 system (Hussain, 1978). For K_xWO_3 system the TTB phase form within $0.42 \leq x \leq 0.57$ (Hussain, 1978), whereas in Na_xWO_3 system it forms when $x \leq 0.48$ (Takusagawa *et al.*, 1976).

Infrared absorption spectroscopy of polycrystalline Na_xWO_3 series

Infrared absorption spectra of polycrystalline Na_xWO_3 samples measured at room temperature are shown in Fig. 15. For direct comparison, the IR absorption spectrum of WO_3 (monoclinic, room temperature) is also included in Fig. 15. The spectra are measured in the range of 50 cm^{-1} - 4000 cm^{-1} . Below 220 cm^{-1} and above 1250 cm^{-1} all spectra appear featureless (not shown).

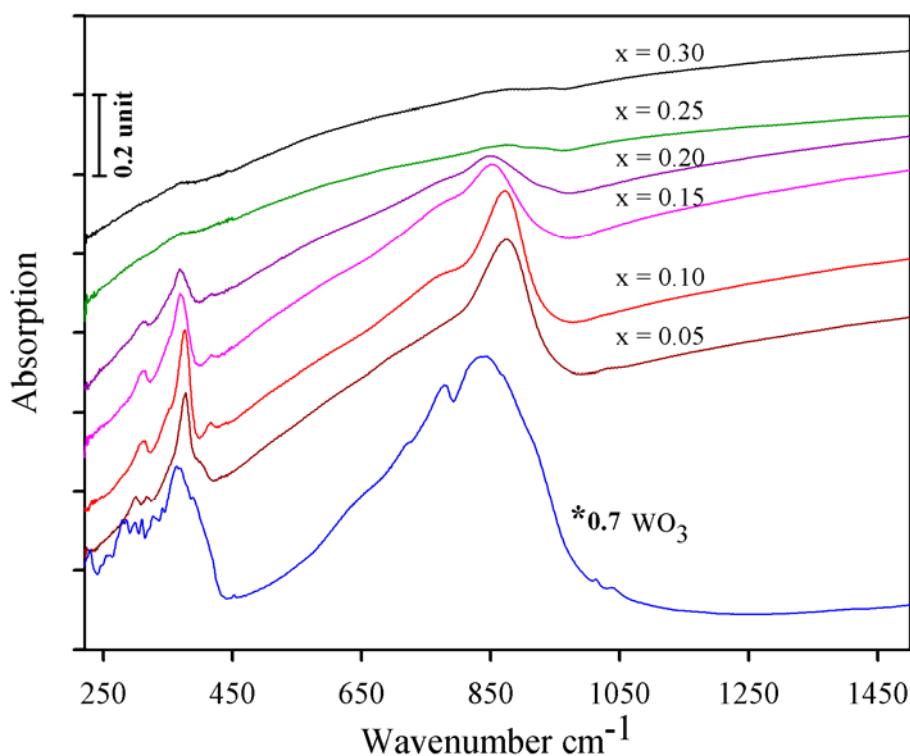


Fig. 15 The infrared absorption spectra of polycrystalline Na_xWO_3 series. The spectrum of WO_3 is multiplied by a factor of 0.7 for direct comparison. The spectra are shifted vertically for better comparison.

Peak positions for nominal composition $0.05 \leq x \leq 0.20$ are listed in Table 4. $\text{Na}_{0.05}\text{WO}_3$ shows 4 peaks with maxima at about 300, 316, 375, and 866 cm^{-1} and a sign of a broad peak with

maximum at about 750 cm^{-1} . The samples with nominal compositions $\text{Na}_{0.10}\text{WO}_3$, $\text{Na}_{0.15}\text{WO}_3$ and $\text{Na}_{0.2}\text{WO}_3$ show same number of absorption peaks.

Table 4 List of IR absorption peak positions and corresponding XRD results of Na_xWO_3 .

Nominal composition, x	1 st peak cm^{-1}	2 nd peak cm^{-1}	3 rd peak cm^{-1}	4 th peak cm^{-1}	5 th peak cm^{-1}	Phase	Lattice parameter / Å
0.05	300	316	375		866	PTB _o	a = 7.4068 (5) b = 7.4410(4) c = 7.7580(4)
0.10	311		375	416	862	PTB _t	a = 5.2567(6) c = 7.8085(5)
0.15	311		368	416	851	PTB _t + Δ	a = 5.2595(5) c = 7.8133(8)
0.20	311		367	417	849	PTB _t + Δ	a = 5.2601(5) c = 7.8139(7)

Δ = mixture of PTB_c and TTB Na_xWO_3 , which do not show any phonon peak.

The broad peak with maximum at about 750 cm^{-1} is present in all samples ($0.05 \leq x \leq 0.20$). The absorption band near 850 cm^{-1} can be assigned to the stretching mode of W-O bonds and absorption band near 350 cm^{-1} is due to O-W-O bending character in WO_6 octahedra. The peaks centered at 375 and 862 cm^{-1} for $\text{Na}_{0.1}\text{WO}_3$ sample shifts to 368 and 851 cm^{-1} , respectively for nominal $\text{Na}_{0.15}\text{WO}_3$ sample and for nominal $\text{Na}_{0.2}\text{WO}_3$ the peak positions are 367 and 849 cm^{-1} , respectively. This significance shift in peak positions to low wavenumber can be explained with the increase in sodium content in the PTB_t phase with increasing nominal composition. This effect could correspond to the increase in lattice parameters (Table 4). The systematic decrease in phonon absorption intensity with increasing x from 0.1 to 0.20 can be explained by the decreasing contribution of the PTB_t phase.

The samples with nominal composition $x \geq 0.25$ do not show any significant phonon absorption. In Fig. 16 the spectra of a few samples ($x \geq 0.25$) are shown as a typical example in comparison to spectra of WO_3 (monoclinic) and $\text{Na}_{0.1}\text{WO}_3$ (PTB_t). The featureless increase in intensity with increasing wavenumber can be related to metallic behavior of the samples which will be discussed below (see page 56, 3rd para). The broad hump in the range between 800 cm^{-1} and 400 cm^{-1} can be related to the surface oxidation during grinding of the samples for the preparation of pellet for IR absorption spectra.

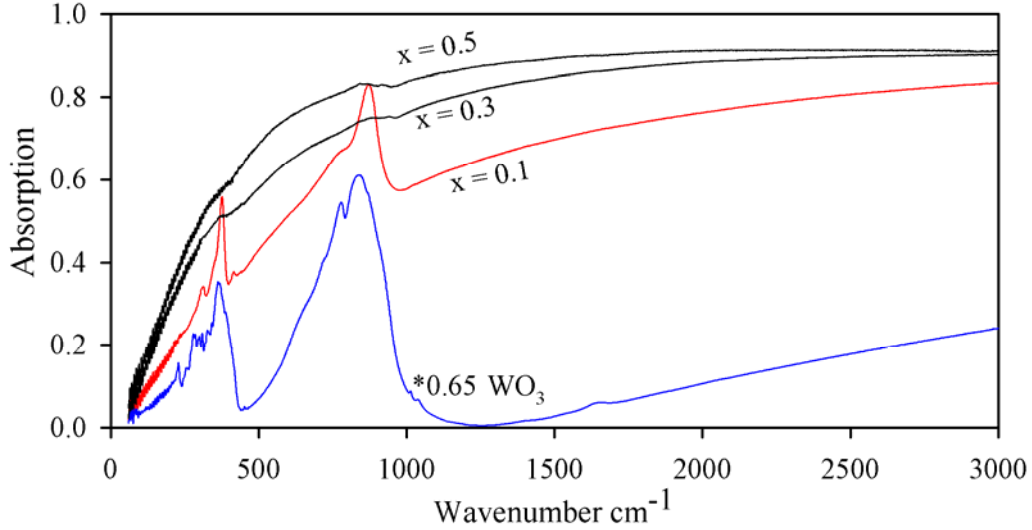


Fig. 16 IR absorption spectra of some Na_xWO_3 samples (as denoted) down to 50 cm^{-1} . The spectrum of WO_3 is multiplied by a factor of 0.65 for better comparison.

Raman spectra of polycrystalline Na_xWO_3 series

Raman spectra of polycrystalline $\text{Na}_{0.05}\text{WO}_3$ and $\text{Na}_{0.1}\text{WO}_3$ samples measured at room temperature are shown in Fig. 17. For direct comparison, the Raman spectrum of WO_3 (monoclinic, room temperature) is also included in Fig. 17.

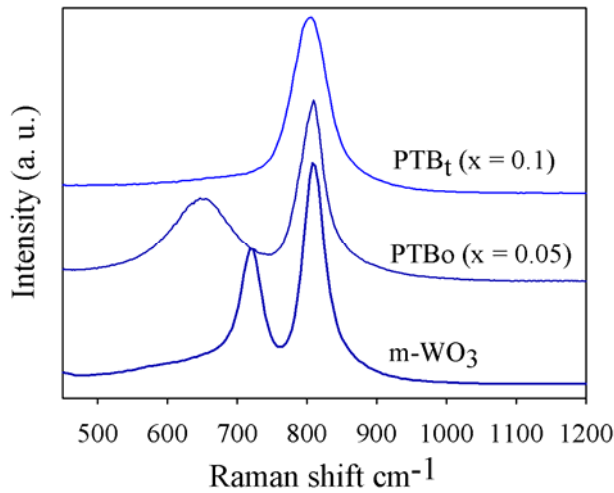


Fig. 17 Raman spectra of polycrystalline Na_xWO_3 samples (as denoted) at room temperature.

The Raman spectrum of polycrystalline monoclinic WO_3 shows two strong peaks centered at 720 cm^{-1} and 809 cm^{-1} , which are due to the phonons in W-O framework (Salje, 1975). The peak centered at 720 cm^{-1} exhibit downward shift to 650 cm^{-1} for nominal $\text{Na}_{0.05}\text{WO}_3$ (PTB_o) and the intensity of the peak decreases as well as broadening increases, whereas the second peak (centered at 809 cm^{-1}) does not shift. The Raman peak centered at 720 cm^{-1} disappears completely for nominal composition $\text{Na}_{0.1}\text{WO}_3$ (PTB_t). However, Egdel *et al.* (1989) reported two Raman peaks centered at about 700 cm^{-1} and 803 cm^{-1} for PTB_t $\text{Na}_{0.1}\text{WO}_3$. This

discrepancy may be due to the use of different laser for excitation. Lee *et al.* (2003) measured the Raman spectra of crystalline thin films of Li_xWO_3 system and reported similar spectral change as obtained for present investigation of crystalline Na_xWO_3 system.

Reflectivity spectra of polycrystalline Na_xWO_3 series (UV-VIS range)

The reflectivity spectra of polycrystalline $\text{PTB}_c \text{Na}_x\text{WO}_3$ is shown in Fig. 18. The minima of the reflectivity spectra shift to low frequencies with decreasing nominal sodium content in Na_xWO_3 . The measured powder reflectivities were directly compared with the single crystal data given by Owen *et al.* (1978).

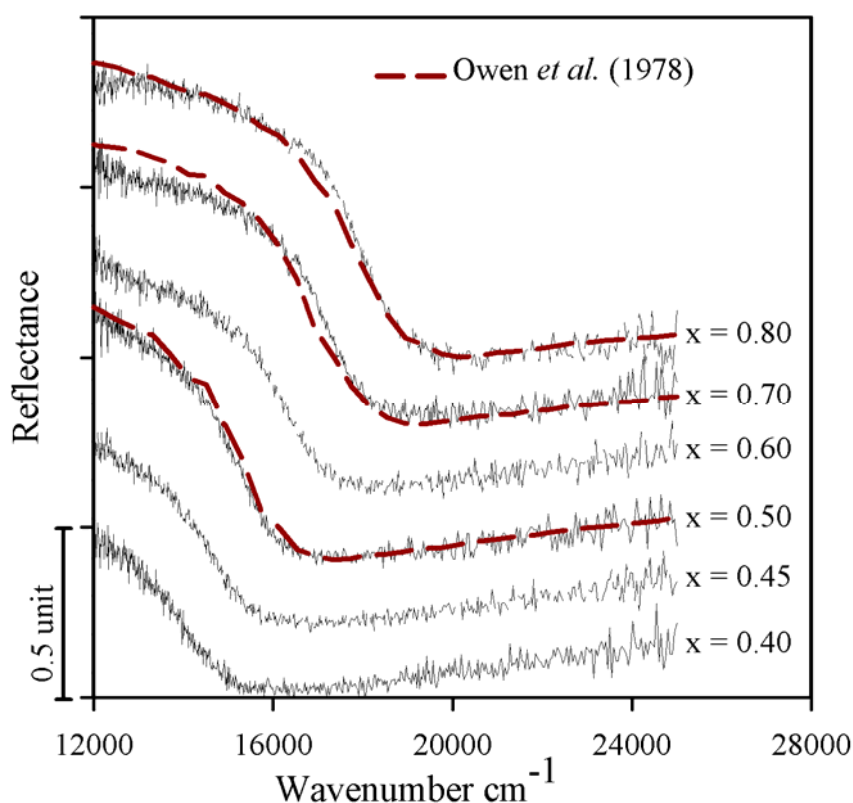


Fig. 18 Powder reflectivity spectra of $\text{PTB}_c \text{Na}_x\text{WO}_3$ series. The spectra are shifted vertically for the sake of clarity. The dashed curves represent the calculated reflectivity from single crystal data of Owen *et al.* (1978).

Owen *et al.* (1978) measured directly the real and imaginary part of complex dielectric function by ellipsometric method. In Fig. 18, single crystal reflectivity was calculated from the reported data of real and imaginary parts of complex dielectric function as described in data evaluation section of experimental part (Eqs. 6, 12 - 14; page 17). The present reflectivity spectra, therefore, shows a direct link between the earlier powder data (Brown *et al.*, 1954 and Dickens *et al.*, 1968), present powder data and earlier single crystal data (Owen *et al.*, 1978). Thus, the

reflectivity of powder samples can be used to follow the shift of the minima and measure the doping effect.

Scanning electron microscopy of polycrystalline Na_xWO_3 series

The scanning electron microscopy (SEM) images of the polycrystalline samples, Na_xWO_3 , are shown in Fig. 19a, b, and c. Crystallites with rectangular, truncated octahedron and cubic morphology are clearly visible in the images.

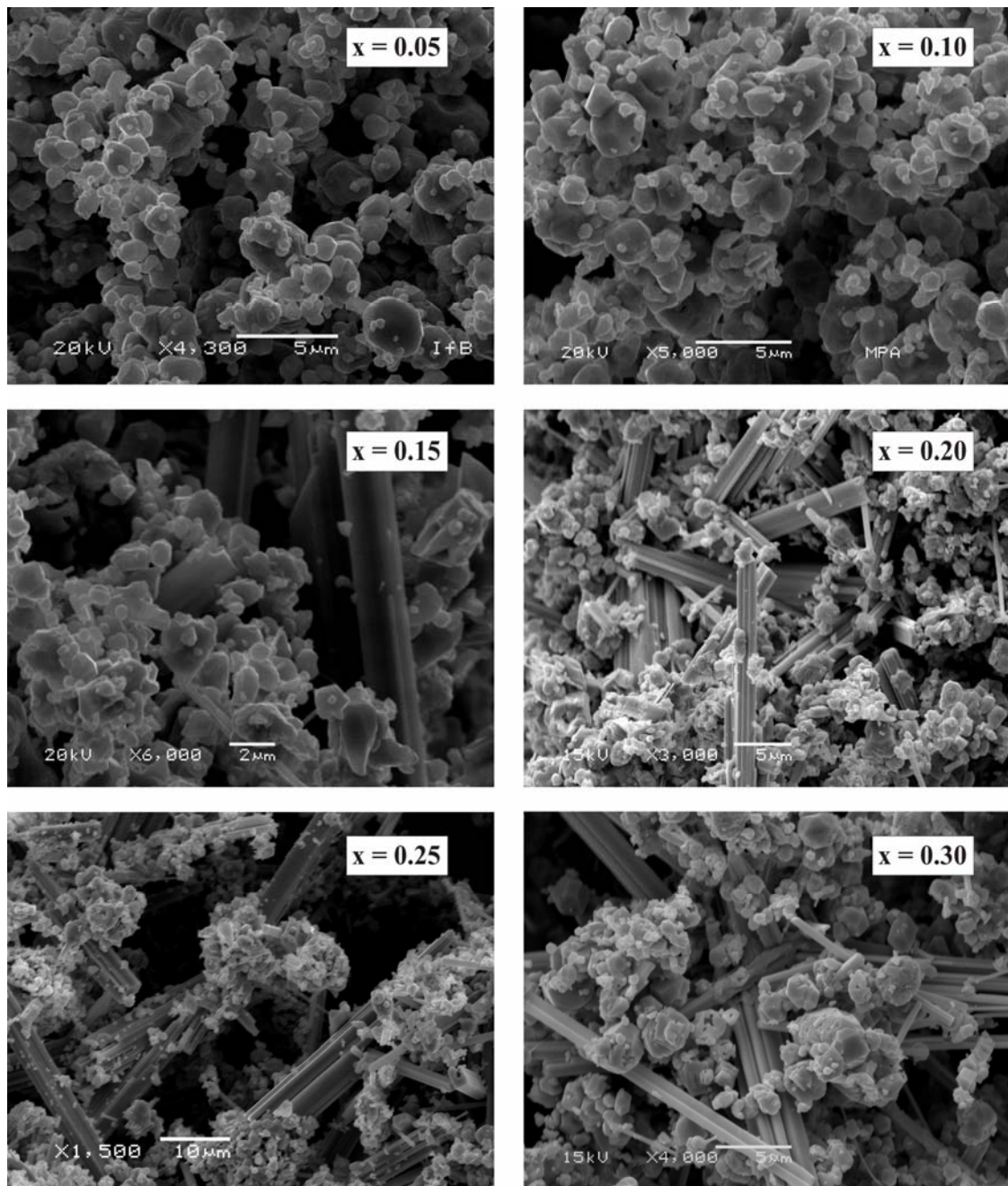


Fig. 19a SEM images of polycrystalline Na_xWO_3 ($x = 0.05 - 0.30$). The needle shaped crystals belong to TTB phase.

For samples $x = 0.05, 0.10$ stubby irregular shaped crystallites can be seen. For $x = 0.15 - 0.35$ samples, long rectangular crystallites (TTB phase) along with stubby irregular shaped crystallites are visible. These rectangular needles are up to $30\ \mu\text{m}$ long and belong to TTB phase as reported for K-TTB system (Debnath *et al.*, 2008b). The crystal shape of $x = 0.4 - 0.5$ samples are truncated octahedron whereas $x = 0.6 - 0.8$ samples show cubic morphology. The sample $x = 0.9$ shows morphology as $x = 0.8$ sample but additionally some needle shaped crystals, which can also be identified in XRD pattern as impurity phase.

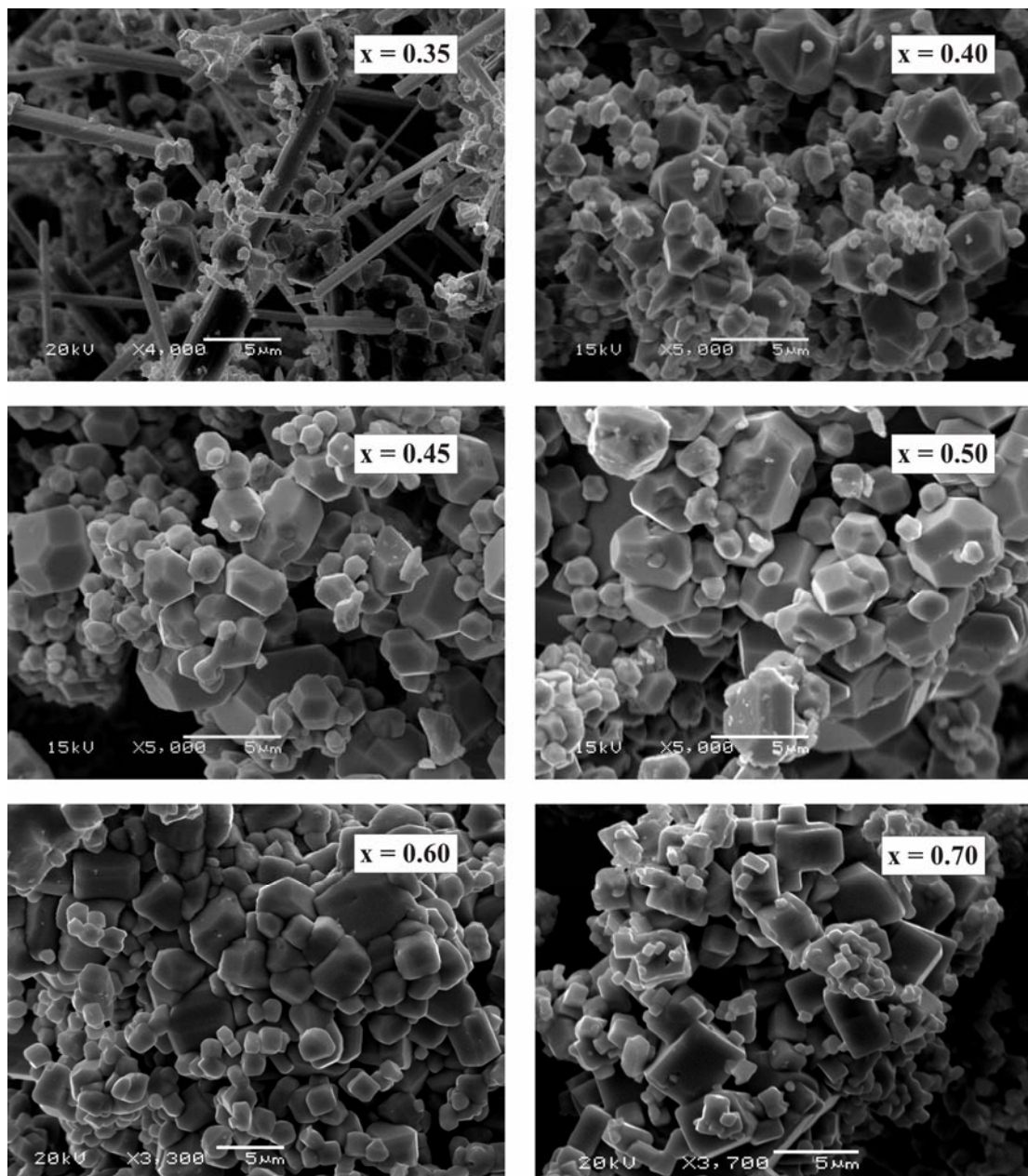


Fig. 19b SEM images of polycrystalline Na_xWO_3 ($x = 0.35 - 0.70$). The SEM images of samples with $x = 0.40, 0.45$, and 0.5 show truncated octahedron shaped crystals, whereas the samples with $x = 0.6$, and 0.7 show the cubic morphology.

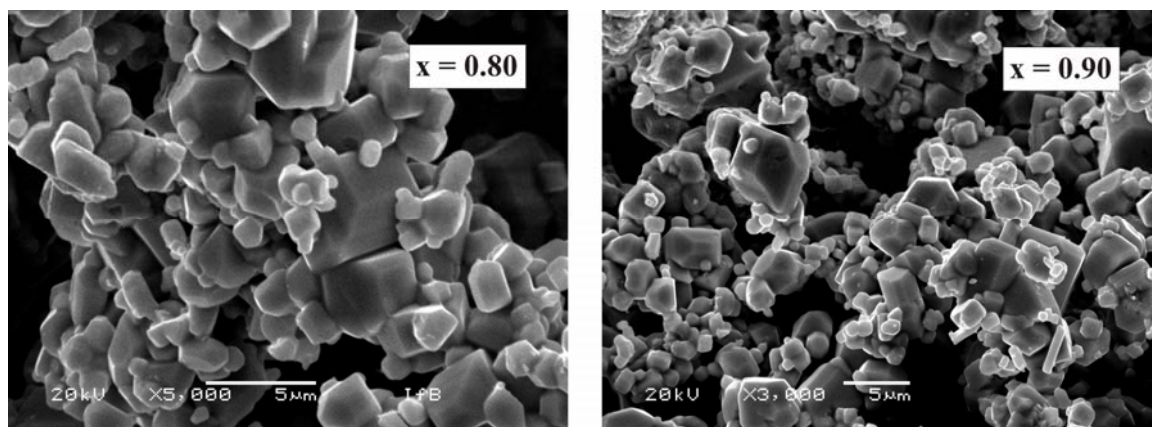


Fig. 19c SEM images of polycrystalline Na_xWO_3 ($x = 0.8, 0.9$). The SEM image of sample with $x = 0.9$ show the presence of some small needles belong to the impurity phase.

4.1.2 Samples (Na_xWO_3) prepared by chemical transport method

It was possible to grow up to about 0.2 mm large crystals, which belong to PTB_0 , TTB , and PTB_c phases. It was, however, not successful to grow PTB_t crystal big enough to study optical reflectivity by available instrumental facilities. The properties and characterization of PTB_0 , TTB , and PTB_c crystals will be described in the following.

PTB_0 crystal

$\text{PTB}_0 \text{Na}_x\text{WO}_3$ was prepared by chemical transport method using HgCl_2 as a transporting agent. Few crystals were crushed into powder for characterization by X-ray diffraction technique and IR absorption spectroscopy. Fig. 20 shows the X-ray diffraction pattern along with Rietveld refinement, which reveals a very good agreement between the experimental and theoretical pattern using space group Pcnb supporting earlier results for PTB_0 phase of WO_3 . Scanning electron microscopy (SEM) images of some selected crystals are shown in Fig. 21a. The crystals show rectangular morphology and crystal size up to $150 \mu\text{m} \times 100 \mu\text{m} \times 80 \mu\text{m}$. A close look of the SEM images (Fig. 21b) show these larger crystals formed by staking of thinner “flake crystals”. The picture of a polished crystal from the same batch is shown in Fig. 21c. Polarized micro reflectivity measurement were carried out on this polished crystal slices in the optical range 550 cm^{-1} to 10000 cm^{-1} using a rectangular aperture of size about $90 \mu\text{m} \times 60 \mu\text{m}$ and the reflectivity spectra are shown in Fig. 22a, which shows highly anisotropy. These reflectivity spectra were fitted using Lorentz oscillator model. Details will be discussed below (page 83). Although the crystal structure is orthorhombic, the polarized reflectivity spectra were measured only in two directions. No attempts was taken to measure the reflectivity in third direction because from the SEM images it is apparent that larger crystals formed by

staking of thinner “flake crystals” and measurement of reflectivity on this inhomogeneous surface may include large error.

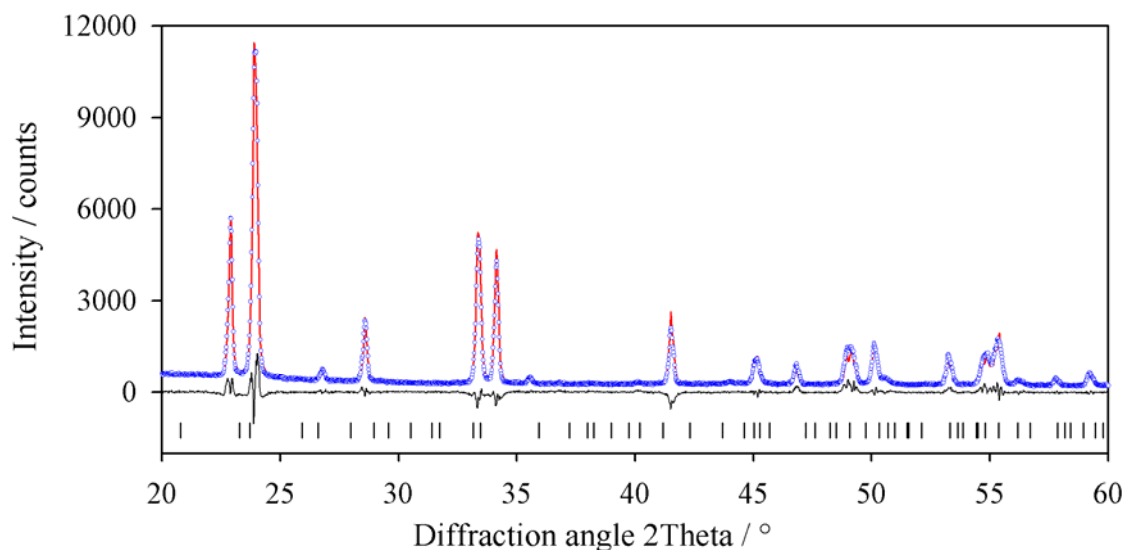


Fig. 20 Rietveld refinement fit for $\text{Na}_{0.037}\text{WO}_3$ (composition from microprobe) sample. The blue dots indicates the observed pattern, the red line through the blue dots indicates the refined pattern. The positions of the refined reflection peaks are shown by the ticks. The black line above the ticks indicates the difference of observed and calculated pattern. Rietveld refinement was done in the range of $2\theta = 20 - 110^\circ$.

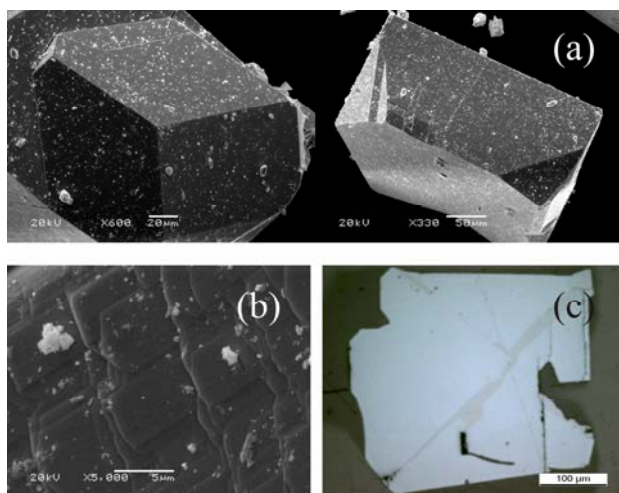


Fig. 21 SEM images(a and b) and optical micrograph of polished crystal (c) of $\text{Na}_{0.037}\text{WO}_3$ (PTB_o). The parallel flake like crystals are clearly visible (b).

The chemical composition was measured by electron microprobe analysis of polished crystal. According to this an average value of $\text{Na}_{0.037(3)}\text{WO}_3$ is obtained. The O stoichiometry was calculated as Na_xWO_3 . The Raman spectrum (Fig. 22b) of polished $\text{Na}_{0.037}\text{WO}_3$ crystal shows

the similar spectral feature that of the polycrystalline PTB_0 phase (compare Fig. 17, page 29). IR absorption spectrum of crushed $\text{Na}_{0.037}\text{WO}_3$ crystals was measured and shown in Fig. 22c. The spectrum shows similar spectral feature with the polycrystalline PTB_0 phase (compare Fig. 15, page 27).

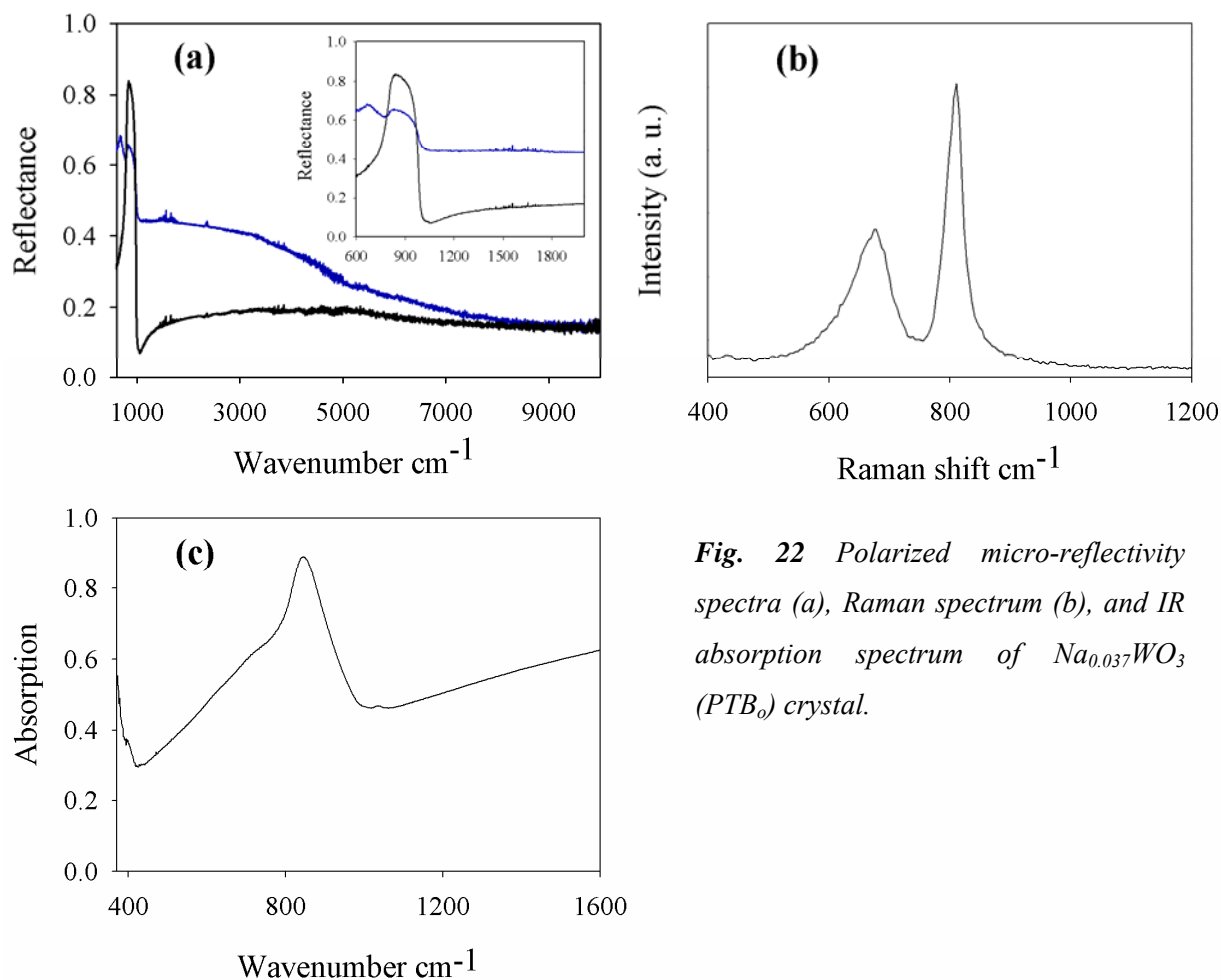


Fig. 22 Polarized micro-reflectivity spectra (a), Raman spectrum (b), and IR absorption spectrum of $\text{Na}_{0.037}\text{WO}_3$ (PTB_0) crystal.

TTB crystal

Tetragonal (TTB) Na_xWO_3 crystal was prepared by using HgCl_2 as a mineralizer. Scanning electron microscopy (SEM) images of TTB crystals (Fig. 23a) show very long needle-type crystals of length up to 250 μm or more. A close look of the SEM image shows parallel growth of many thinner needles. For characterization by X-ray diffraction technique and IR absorption spectroscopy, few crystals were grinded in a mortar. Fig. 23b shows the X-ray diffraction pattern along with Rietveld refinement, which reveals a very good agreement between the experimental and theoretical pattern using space group $\text{P4}/\text{mbm}$ supporting earlier results for TTB phase of Na_xWO_3 .

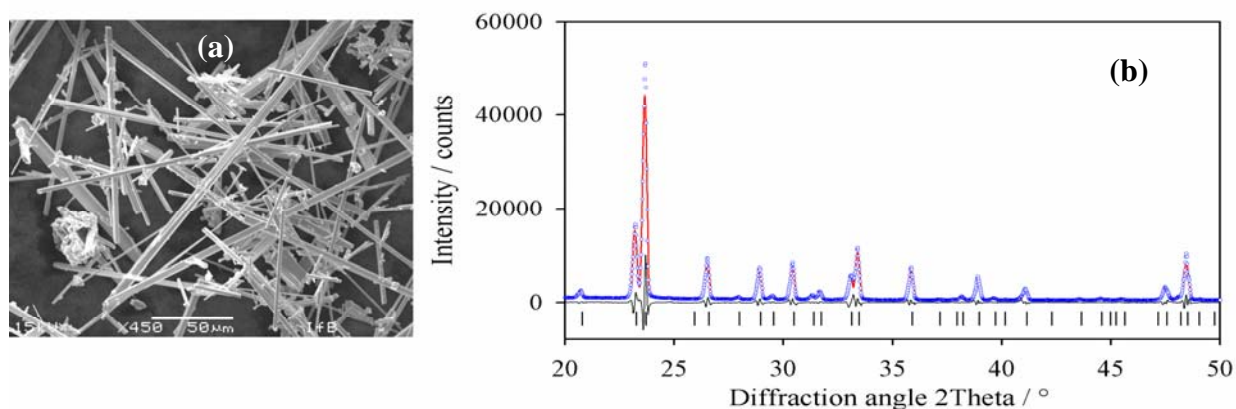


Fig. 23 SEM image (a), and Rietveld refinement fit of XRD pattern (b) for $\text{Na}_{0.38}\text{WO}_3$ (composition from microprobe) sample. The descriptions of the symbols in XRD pattern are same as described in Fig. 20.

The picture of the two biggest polished $\text{Na}_{0.38}\text{WO}_3$ crystals from the same batch is shown in Fig. 24a. Polarized micro reflectivity measurement were carried out on this polished crystal slices in the optical range 2000 cm^{-1} to 18000 cm^{-1} using a rectangular aperture of size about $90\text{ }\mu\text{m} \times 30\text{ }\mu\text{m}$. The reflectivity spectra (Fig. 24b) show strong anisotropy.

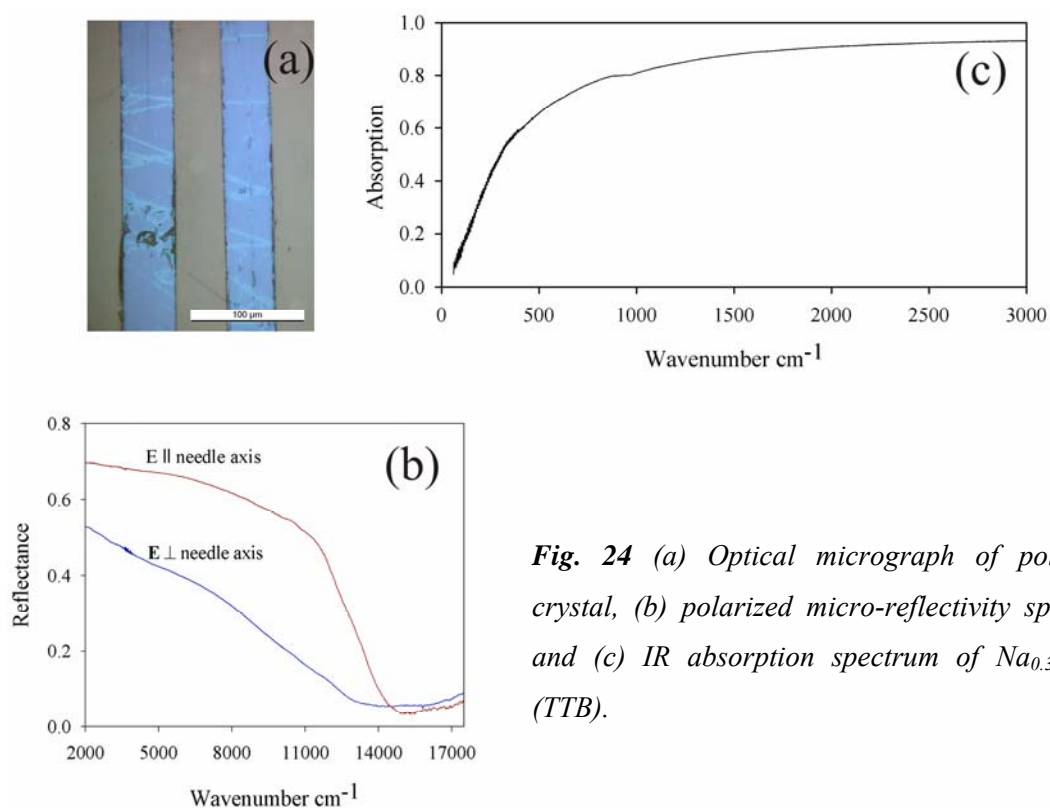


Fig. 24 (a) Optical micrograph of polished crystal, (b) polarized micro-reflectivity spectra, and (c) IR absorption spectrum of $\text{Na}_{0.38}\text{WO}_3$ (TTB).

Due to inadequate crystal size the reflectivity spectra could be measured only above 2000 cm^{-1} . The $E \parallel c$ spectrum could be fitted using Drude equation for reflectivity as well as an over-damped oscillator with high oscillator strength. For $E \perp c$ spectrum, an additional minimum

structure appears at about 4500 cm^{-1} , which was also reported for tetragonal $\text{K}_{0.5}\text{WO}_3$, $\text{K}_{0.6}\text{WO}_3$ (Hussain *et al.*, 1997; Lynch *et al.*, 1973). Lynch *et al.* (1973) explained this minimum feature considering the pentagonal tunnel, which exists in the crystal structure.

The chemical composition obtained by electron microprobe analysis of polished crystal give an average value of $\text{Na}_{0.38(2)}\text{WO}_3$. The IR absorption spectrum of $\text{Na}_{0.38}\text{WO}_3$ is shown in Fig. 24c. The spectrum shows typical spectral feature for metallic oxides e.g., ReO_3 (Feinleib *et al.*, 1968), K_xWO_3 (Hussain *et al.*, 2002).

PTB_c crystal

Attempts were taken to prepare bigger cubic Na_xWO_3 crystal by chemical transport method using HgCl_2 as a transporting agent. Crystals up to $50\text{ }\mu\text{m} \times 40\text{ }\mu\text{m}$ in size could be grown but only very less amount of product has been transported. Fig. 25a shows the optical micrograph of three selected polished crystals. Polarized reflectivity reveals the isotropic nature of these crystals. The typical red color indicates that the sodium content must be more than 0.5 and that the crystal symmetry should be cubic, too.

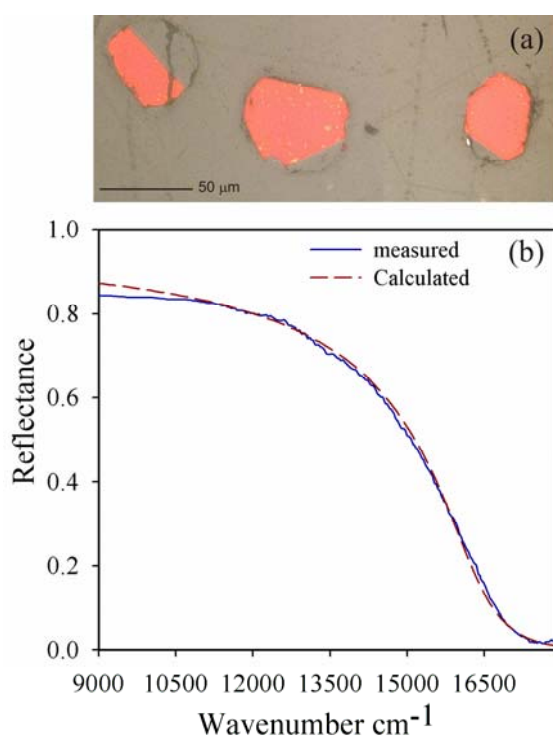


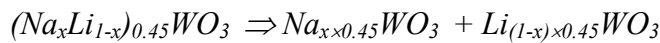
Fig. 25 Optical micrograph (a), and reflectivity spectrum (b) of polished crystals, $\text{Na}_{0.58}\text{WO}_3$ (PTB_c). The spectrum was fitted (dashed curve) with Drude free carrier model. The parameter values are, $\omega_p = 16300\text{ cm}^{-1}$, $\gamma = 1550\text{ cm}^{-1}$, and $\epsilon_\infty = 4.85$.

According to microprobe analysis the chemical composition of these crystal is $\text{Na}_{0.58(2)}\text{WO}_3$. The optical micro-reflectivity was measured above 9000 cm^{-1} . The spectrum can be fitted reasonably with Owen *et al.* (1978) single crystal data and Drude free carrier model (Fig. 25b).

4.2 Characterization of $(\text{Na}_x\text{Li}_{1-x})_{0.45}\text{WO}_3$ ($x = 0.0 - 1.0$) system

A series of polycrystalline samples with nominal composition $(\text{Na}_x\text{Li}_{1-x})_{0.45}\text{WO}_3$ were prepared by conventional solid state method. The SEM images of the samples show cubic morphology (Fig. 26a). The SEM/EDX analysis show that some crystals contain sodium, tungsten and oxygen and some crystals contain only tungsten and oxygen. It was not, however, possible to detect Li due to instrumental limitations. The X-ray diffraction results obtained by Guinier photographic method are listed in Table 5.

Table 5 XRD results of $(\text{Na}_x\text{Li}_{1-x})_{0.45}\text{WO}_3$ system and calculated M in $M_x\text{WO}_3$ ($M = \text{Na} / \text{Li}$).



Nominal composition,		Phase observed, Guinier photographic method	Lattice parameter Na-PTB _c system, Å	Calculated composition x in Na _x WO ₃ (Brown <i>et al.</i> , 1954)	Lattice parameter Li-PTB _c system, Å	Calculated composition, x in Li _x WO ₃ (Eq. 19)
x×0.45	(1-x)×0.45					
0.45	0.0	Single phase, PTB _c	3.8223 (1)	0.460	-	-
0.36	0.09	Single phase, PTB _c	3.8121 (2)	0.337	-	-
0.27	0.18	Two PTB _c phases	3.8050 (2)	0.250	3.7501 (3)	0.297
0.225	0.225	Two PTB _c phases	3.8010 (3)	0.201	3.7448 (3)	0.324
0.135	0.315	Two PTB _c phases	3.7982 (3)	0.167	3.7391 (2)	0.354
0.09	0.36	Two PTB _c phases	3.7980 (4)	0.165	3.7371 (3)	0.364
0.0	0.45	Single phase PTB _c	-	-	3.7223 (2)	0.440

The samples $(\text{Na}_x\text{Li}_{1-x})_{0.45}\text{WO}_3$ show a mixture of two cubic phases for $x = 0.2, 0.3, 0.5$, and 0.6 , which could be related to a Li_xWO_3 phase (smaller lattice parameters values) and a Na_xWO_3 phase (larger lattice parameter values). This assumption is supported by SEM/EDX analysis. Selected samples were further characterized by X-ray diffraction technique using Bruker D8 diffractometer (transmission geometry, CuK_α radiation). As an example the typical XRD pattern of a sample with nominal composition $x = 0.3$ is shown in Fig. 26b. The Na content, x , of cubic Na_xWO_3 phases were calculated by using the Brown and Bank relation (Eq. 18) and Li content is calculated by using a linear extrapolation of lattice parameter values for $\text{Li}_{0.45}\text{WO}_3$ ($a_c = 3.7204(15)$ Å) and $\text{Li}_{0.4}\text{WO}_3$ ($a_c = 3.7301(7)$ Å) to zero as Eq. 19 as taken from Rüscher *et al.* (2008).

$$a_c(x) \text{ in } \text{Å} = 3.7845 + 0.082x \quad \text{Eq. 18}$$

$$a_c(x) \text{ in } \text{Å} = 3.8077 - 0.194x \quad \text{Eq. 19}$$

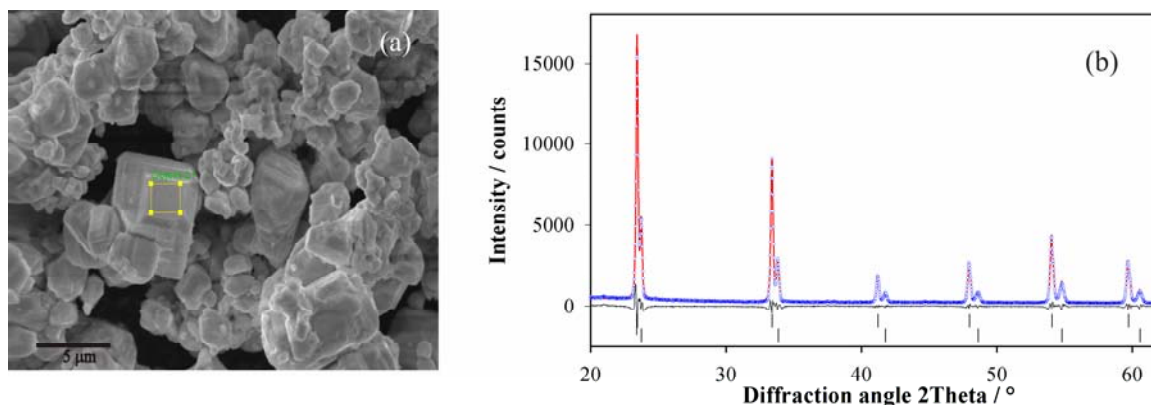


Fig. 26 SEM image (a), and Rietveld refinement fit of XRD pattern (b) of nominal $(\text{Na}_x\text{Li}_{1-x})_{0.45}\text{WO}_3$ ($x = 0.3$) sample. The descriptions of the symbols in XRD pattern are same as described in Fig. 20.

It is seen that the lattice parameter of one PTB_c phase increases with decreasing nominal Li content (\equiv increasing nominal Na content) whereas the lattice parameters of the second PTB_c phase increases. Therefore, it is suggested that the systematic decreasing value is due to the decreasing sodium in Na_xWO_3 and opposite case for Li_xWO_3 . The crystal sizes have been too small (Fig. 26a) for further characterization of their optical properties.

4.3 Characterization of $\text{Na}_{0.8}\text{Nb}_y\text{W}_{1-y}\text{O}_3$ ($y = 0.0 - 0.4$) system

Optical micrographs (reflection mode) of samples with a nominal composition $0.25 \leq y \leq 0.4$ show a mixture of crystallites with three different colors: red-orange, bluish and white. A representative example is shown for a sample of nominal composition $y = 0.4$ in Fig. 27. Micrographs of samples with nominal composition $0.0 \leq y \leq 0.07$ show only red-orange crystals. For $y = 0.1$, bluish particle appears which increases in contribution with increasing nominal y .

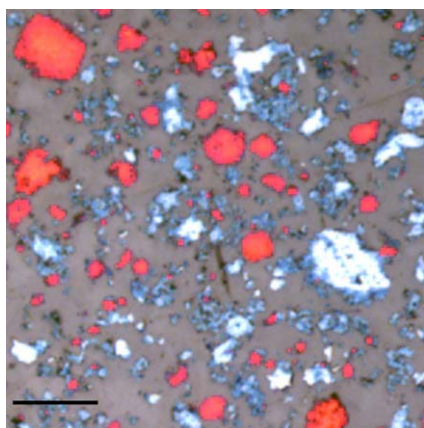


Fig. 27 Optical micrograph of a polished sample of nominal composition $\text{Na}_{0.8}\text{Nb}_{0.4}\text{W}_{0.6}\text{O}_3$ showing a mixture of three different coloured crystals: red, light blue and white. The scale bar is 30 μm .

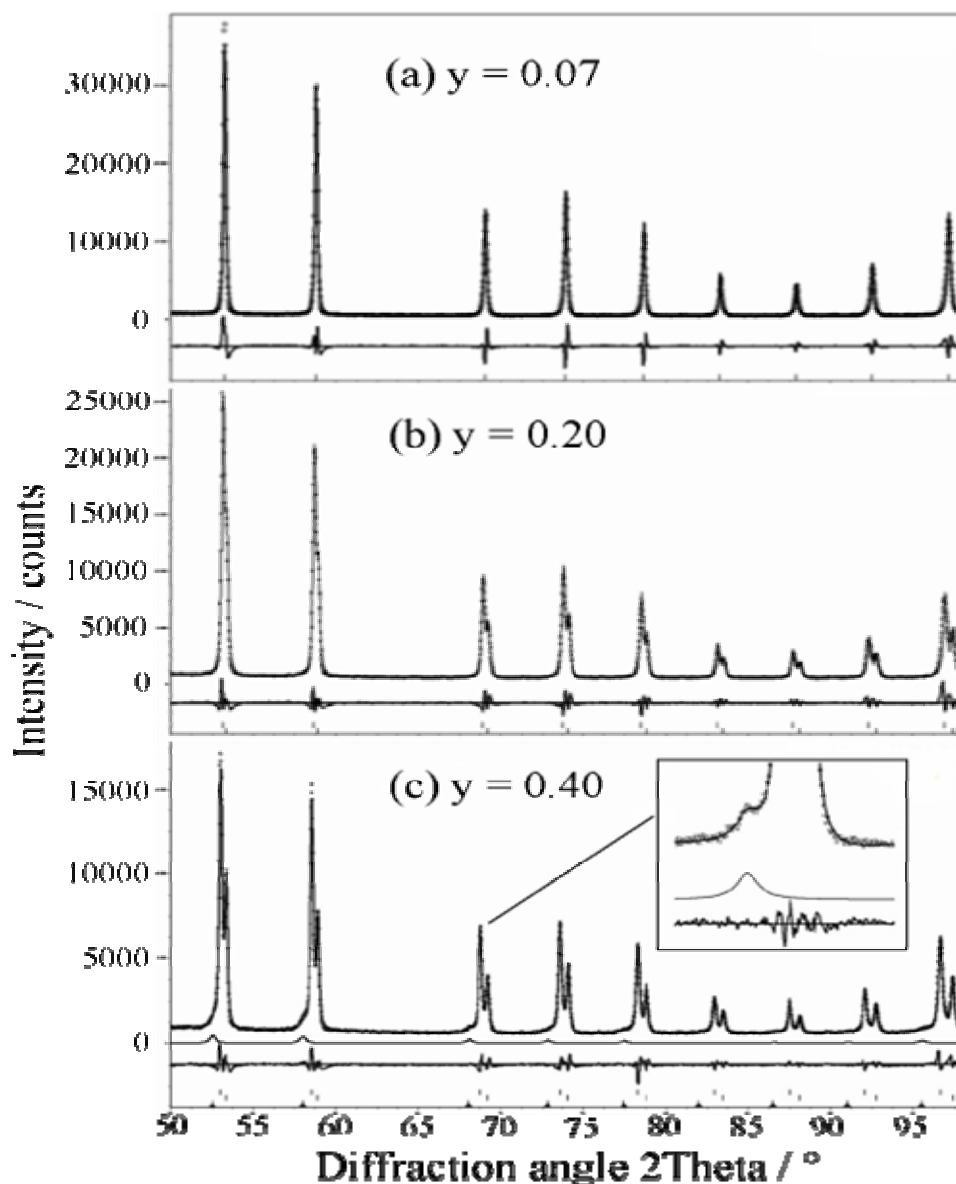


Fig. 28 Observed (dotted) and refined (solid line) XRD pattern for samples of nominal composition $\text{Na}_{0.8}\text{Nb}_y\text{W}_{1-y}\text{O}_3$, (a) $y = 0.07$, (b) $y = 0.20$ and (c) $y = 0.40$. The respective difference curve and indexed peak positions (bars) are also shown. For $y = 0.40$ (c), the additional refined pattern of the third phase is shown separately. Inset shows an enlarge scale for 220 peaks.

The X-ray diffraction pattern for $0.0 \leq y \leq 0.07$ samples could uniquely be refined as single cubic PTB_c phase (Fig. 28a). With a further increase in nominal niobium content ($y \geq 0.1$) there is a splitting of all diffraction peaks corresponding to two cubic phases of well separated lattice parameters as shown for the $y = 0.2$ sample (Fig. 28b).

For the samples with nominal niobium content $y \geq 0.25$, a third characteristic diffraction peak (Fig. 28c) appears. This peak could well be described in a three phase Rietveld refinement as a third cubic phase as shown in Fig. 28c for the $y = 0.4$ sample. For better comparison the effect

of phase separation into the two leading perovskite type phases is shown more clearly in Fig. 29 for the 210 diffraction peak. There is a gradual decrease in peak height together with growing of a low angle shoulder with increasing y which becomes significant in the refinement at $y = 0.10$.

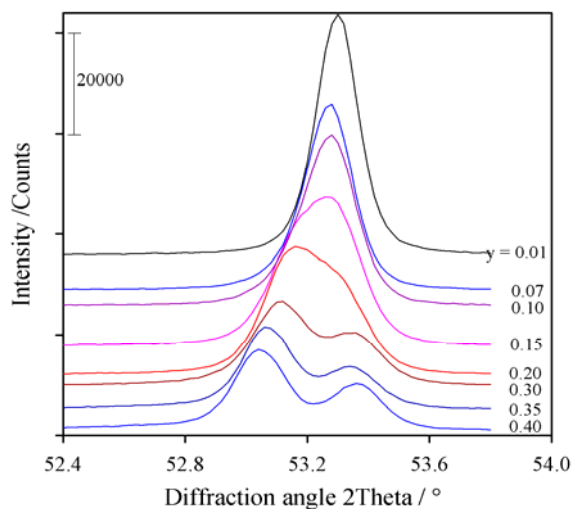


Fig. 29 An enlarge view of 210 X-ray diffraction line of samples $\text{Na}_{0.8}\text{Nb}_y\text{W}_{1-y}\text{O}_3$ showing a systematic development of second phase for $y \geq 0.1$. The peaks are shifted vertically for the sake of clarity.

The refined lattice parameters of the phases and their relative contributions are plotted in Fig. 30 and 31, respectively.

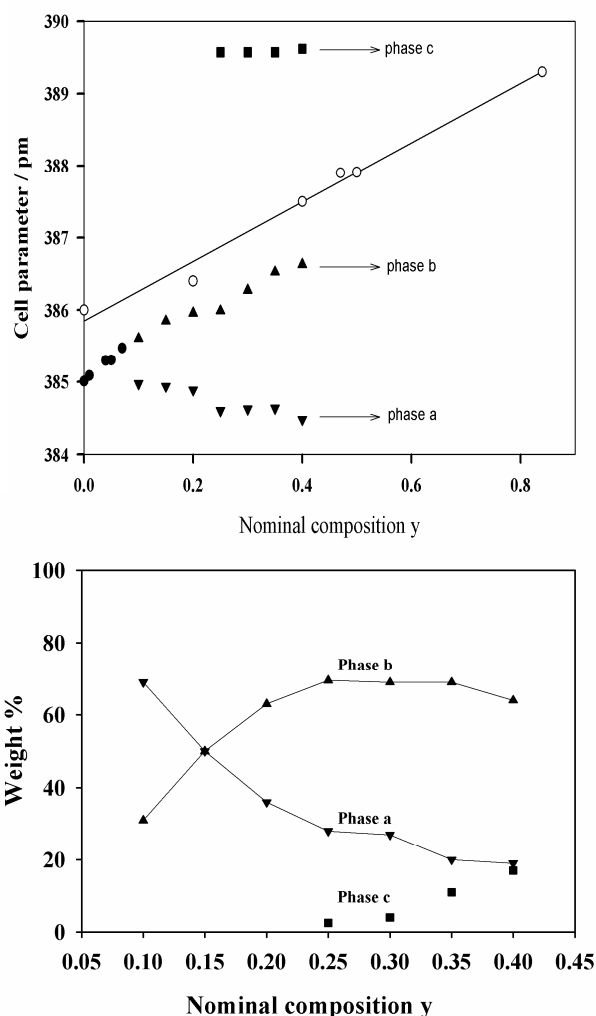


Fig. 30 The refined cell parameter of products from nominal composition $\text{Na}_{0.8}\text{Nb}_y\text{W}_{1-y}\text{O}_3$ (closed symbols) compared with that of the reported (open circles) for cubic and pseudo-cubic $\text{NaNb}_y\text{W}_{1-y}\text{O}_3$ system (Miyamoto et al., 1983). Single phase (closed circles), two phases (closed triangle top down, “phase a”) and three phases (closed triangle top up, “phase b”) and closed square “phase c”) refinement were done for samples with nominal composition $y = 0.0 - 0.07$, $y = 0.10 - 0.20$, and $y = 0.25 - 0.40$, respectively.

Fig. 31 Contribution of different phases according to Rietveld refinement. Two phases and three phases refinements were done for samples $\text{Na}_{0.8}\text{Nb}_y\text{W}_{1-y}\text{O}_3$ with nominal composition $y = 0.10 - 0.20$ and $y = 0.25 - 0.40$, respectively (symbols as given in Fig. 30).

There is a systematic decrease in lattice parameter value for “phase a” and an increase for “phase b” related on increasing nominal y whereas for “phase c” the lattice parameter values remain constant. The X-ray diffraction pattern for $0.0 \leq y \leq 0.07$ samples could uniquely be refined as single cubic PTB_c phase (Fig. 28a). With a further increase in nominal niobium content ($y \geq 0.1$) there is a splitting of all diffraction peaks corresponding to two cubic phases of well separated lattice parameters as shown for the $y = 0.2$ sample (Fig. 28b).

The relative contributions in the two phase range show approximately complementary behavior for a (decrease) and b (increase) up to $y = 0.25$. For $y \geq 0.25$ the contributions of “phase b” saturates or even tend to decrease whereas the contribution of “phase c” strongly increases. With the help of microprobe analysis, it is shown (see below) that “phase a” corresponds to pure sodium tungsten bronze, Na_xWO₃, which appear as red-orange coloured crystals in Fig. 27. The white crystals corresponds to a composition Na_{0.5}NbO_{2.75}, which is related with the y independent cell parameter of about 389.7 pm. Consequently the values of increasing lattice parameters are related to bluish colored crystals in Fig. 27. The systematic increase in lattice parameters of “phase b” is related to an increasing substitution of Nb for W as reported by results of Miyamoto *et al.* (1983), which are given for comparison in Fig. 30. These authors observed an increase in lattice parameter values for NaW_{1-z}Nb_zO₃ for increasing z which could tentatively be described as

$$a(z) \text{ in pm} = 4 \cdot z + 386.66 \quad \text{Eq. 20}$$

The slope here is about half of that reported by Dubson *et al.* (1985) for the system Na_xW_{1-z}Ta_zO₃

$$a(x,z) \text{ in pm} = 8.21 \cdot x + (0.87 + 8.07 \cdot x) \cdot z + 378.45 \quad \text{Eq. 21}$$

Eq. 21 becomes the Brown and Banks relation (Eq. 18) for $z = 0$, which applies for the cubic Na_xWO₃ system. A similar dependency as for the system Na_xW_{1-z}Ta_zO₃ may also be suggested for the Na_xW_{1-y}Nb_yO₃ system. The results of the two phase refinements could imply a successful substitution with x about 0.8 and an increase in z as given by the nominal composition y according to

$$a(x,z) \text{ in pm} = 8.21 \cdot x + 4 \cdot z + 378.4, \text{ for } x \text{ close to } 1 \quad \text{Eq. 22}$$

In Fig. 32 the reflectivity spectra of two powder samples with nominal composition Na_{0.8}Nb_yW_{1-y}O₃ are shown. A decrease in reflectivity minimum for $y = 0.07$ sample compare to $y = 0$, indicates the counter doping effect. The shift of reflectivity minima is also observed for other systems (e.g., K_xNb_yW_{1-y}O₃ (TTB) system, will be shown later). It may note that for

nominal $y \geq 0.1$ samples a mixture of phases appear, which makes the system more complicated to explain further the reflectivity spectra.

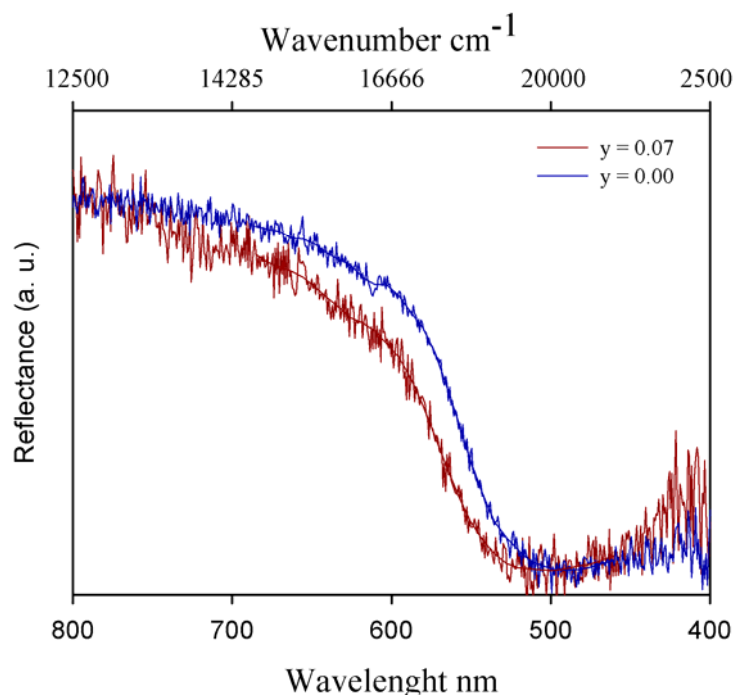


Fig. 32 Reflectivity spectra of powder $\text{Na}_{0.8}\text{Nb}_y\text{W}_{1-y}\text{O}_3$ samples (as denoted) showing the shift of minima towards the low wavenumber after doping Nb.

According to microprobe analysis the “red-orange crystals” contain sodium and tungsten, and no niobium. Quantitative evaluation of the Na / W ratios, show a decrease in x (Table 6) with increasing nominal niobium content in the synthesis batches. The cell parameter decrease from 385.01 to 384.48 pm. Using the Brown and Bank relation (1954) (Eq. 18) the composition of Na in Na_xWO_3 were calculated and show very good agreement to the Na / W ratio that obtained from microprobe analysis (Table 6).

Table 6 Comparison of X-ray diffraction results and electron microprobe analysis results of “red-orange crystals” from the batches of nominal composition $\text{Na}_{0.8}\text{Nb}_y\text{W}_{1-y}\text{O}_3$.

Nominal composition, y	Lattice parameter / pm	Calculated Na content (Na / W) from Eq. 18	Na / W ratio from microprobe analysis
0.0	385.01 (2)	0.80	0.80
0.10	384.97 (1)	0.79	0.77
0.20	384.88 (2)	0.78	0.75
0.25	384.60 (2)	0.75	0.74
0.30	384.62 (2)	0.75	0.74
0.35	384.63 (2)	0.75	0.72
0.40	384.48 (10)	0.74	0.72

A systematic decrease in Na content with increasing nominal y content is also deduced analyzing the optical properties of the red-orange crystals by micro reflection spectroscopy

(Fig. 33). The spectra closely agree with spectra calculated from single crystal data given for the compositions $\text{Na}_{0.805}\text{WO}_3$ and $\text{Na}_{0.695}\text{WO}_3$ by Owen *et al.* (1978). These results thus independently support the systematic decrease in x of red-orange crystals with increasing nominal y as obtained by the decreasing lattice parameter (Fig. 30) and microprobe results.

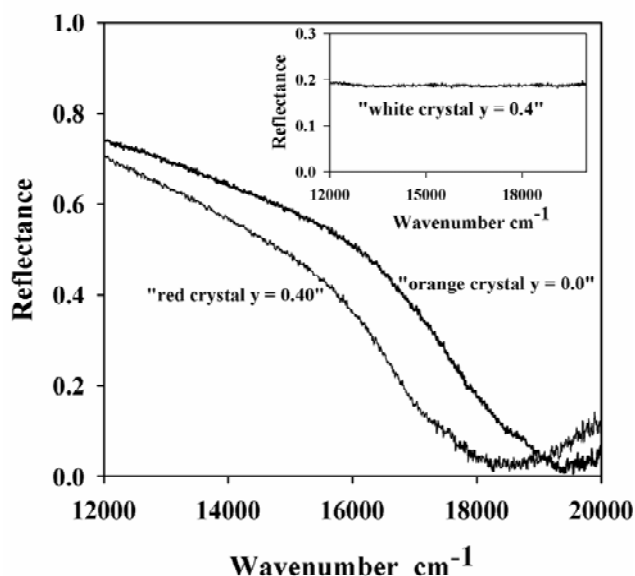


Fig. 33 Optical micro reflectivity spectra of polished crystals, which show Drude type reflectivity for “red-orange” crystals with a systematic change in reflectivity minima with nominal composition $\text{Na}_{0.8}\text{Nb}_y\text{W}_{1-y}\text{O}_3$ ($y = 0.40$ and 0.0), which corresponds to the composition $\text{Na}_{0.72}\text{WO}_3$ and $\text{Na}_{0.8}\text{WO}_3$, respectively (details given in text). The reflectivity of “white” crystals (inset) shows a complete flat behaviour of about 19%.

The optical reflectivity of the white crystals reveals a complete flat behaviour (Fig. 34) down to 1000 cm^{-1} (compare inset in Fig. 33). Below 1000 cm^{-1} the strong increase in reflectivity can be attributed to phonon absorption, which could not be measured to lower wavenumber because of the limited frequency range of the instrument.

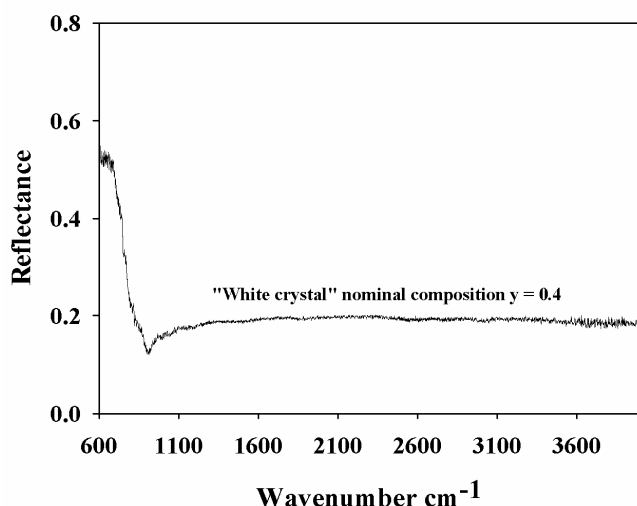


Fig. 34 The reflectivity spectrum of white crystal shows the appearance of strong phonon effect below 1000 cm^{-1} .

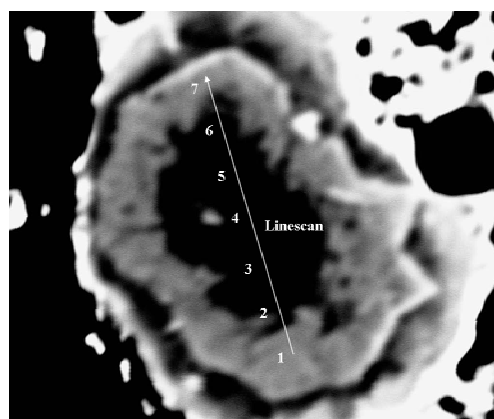


Fig. 35 Backscattered electron picture of a “white” crystal. The white arrow (of length $14\text{ }\mu\text{m}$) corresponds to the position of the microprobe line scan. The numbers are the analyzed points of performed line scan (see Table 7).

Electron beam back scattering pictures of white crystals reveal in most cases a zoned nature concerning their chemical composition (Fig. 35). By scanning along lines as depicted in Fig. 35 obtains that the brighter parts (high scatter) contains Na, W and Nb (Table 7). In the darker inner part the W content is below detection limit and only Na and Nb signals are observed.

Table 7 Results of electron beam line scan of a white crystal which is shown in Fig. 35.

Points	Na / wt%	Nb / wt%	W / wt%	¹ O / wt%	Total / wt%
1	10.13	37.05	25.26	26.07	98.51
2	8.30	55.28	5.79	28.20	97.56
3	8.26	61.34	0.71	29.47	99.78
4	7.40	61.51	0.92	29.30	99.13
5	8.33	61.21	0.52	29.39	99.45
6	10.44	37.80	26.05	26.71	101.00
7	9.61	31.65	32.55	25.47	99.28

¹ O determined by stoichiometry

Data collected on the central part of the white crystals for samples having nominal composition $y = 0.25, 0.30, 0.35$ and 0.40 are given in Table 8. These data are average values from three measurement spots each and only those contributions were taken where the tungsten contents were below the detection limit. The absolute values were calibrated against albite ($\text{NaAlSi}_3\text{O}_8$), niobium(V)oxide (Nb_2O_5) and niobium(IV)oxide (NbO_2) as standards. The values given in Table 8 for Na and Nb are measured absolute values in wt % elemental concentrations.

Table 8 Results of electron microprobe analysis for white crystals from batches of nominal composition $\text{Na}_{0.8}\text{Nb}_y\text{W}_{1-y}\text{O}_3$.

Nominal composition, y	Average Na / wt%	Average Nb / wt%	Average ¹ O / wt%	Total / wt%	Corresponding stoichiometry
0.25	7.40	63.71	30.00	101.11	$\text{Na}_{0.47}\text{NbO}_{2.73}$
0.30	7.99	61.35	29.39	99.45	$\text{Na}_{0.52}\text{NbO}_{2.78}$
0.35	7.53	62.28	29.58	99.95	$\text{Na}_{0.49}\text{NbO}_{2.76}$
0.40	7.62	61.80	29.42	99.39	$\text{Na}_{0.50}\text{NbO}_{2.76}$

¹ O determined by stoichiometry

The oxygen content has been calculated assuming Nb as +5 and alternatively for Nb^{4+} . With Nb taken as +5 lead to a total wt% in the range between 99.4 and 100.2 whereas for Nb^{4+} the values would become between 94.0-93.0 +/- 0.2 wt%. The values close to 100 % are very significant and indicate that Nb can be taken as +5. As an independent check we investigated the crystals of NbO_2 and Nb_2O_5 phases from samples characterized earlier (Rüscher, 1992). The measured data (all in wt %) for the Nb content are 74.6 and 70.11 for NbO_2 and Nb_2O_5 crystals,

respectively. With the oxidation state of Nb in NbO_2 (+4) and Nb_2O_5 (+5) the total wt% comes out at 100.2. According to this there is a very good reproduction for the calculation of these oxidation states using microprobe measurements. Therefore, the corresponding composition of the “white crystals” (central part) can be written as $\text{Na}_{0.5 \pm 0.05}\text{NbO}_{2.75}$.

Raman spectroscopic study of white crystals (Fig. 36) show the high intensity peak centered at about 618 cm^{-1} , which is in the same range as observed for the room temperature phase of lushite, NaNbO_3 (Shen *et al.*, 1998 and Yuzyuk *et al.*, 2004). Yuzyuk *et al.* (2004) reported Nb-O stretching bands at 557 and 601 cm^{-1} . The much broader peaks for $\text{Na}_{0.5}\text{NbO}_{2.75}$ compared to those for NaNbO_3 can be related to the high number of vacancies and their random distribution conserving the higher symmetry. Yuzyuk *et al.* (2004) assigned a high frequency Raman peak centered at 875 cm^{-1} as an “impurity band”. However, for $\text{Na}_{0.5}\text{NbO}_{2.75}$ the peak can be related to stretching mode of terminal $-\text{M}=\text{O}$ ($\text{M} = \text{Nb}/\text{W}$) bonds as in pyrochlore type phase (KNbWO_6) (Debnath *et al.*, 2008b) and in NaNbWO_6 phase (Kuhn *et al.*, 2004).

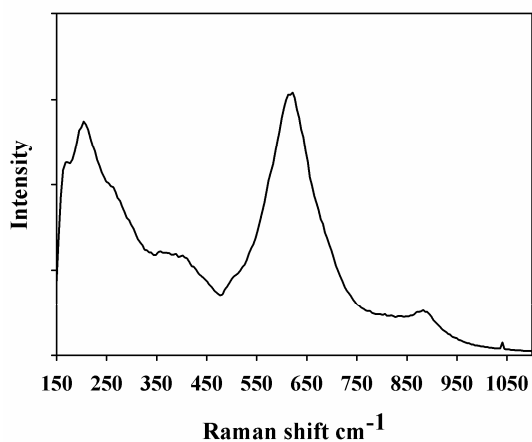


Fig. 36 Raman spectrum of white crystal of composition $\text{Na}_{0.5}\text{NbO}_{2.75}$.

In all the Rietveld refinements, concerning this system, the cubic perovskite structure with space group Pm-3m have been used since the XRD pattern did not give any hint of unit cell doubling or a significant lowering of the symmetry. Thus for $\text{Na}_{0.5}\text{NbO}_{2.75}$ calculation were carried out with Nb ($\frac{1}{2} \frac{1}{2} \frac{1}{2}$), O ($\frac{1}{2} \frac{1}{2} 0$) and Na ($0 0 0$) with occupation factors 1, 2.75/3 and 1/2, respectively. The lattice parameter obtained in the refinement reads 389.7 pm. Darlington and Knight (1999) reported for cubic lushite lattice parameter values for temperatures between 920 and 1030 K, which show a linear increase with temperature according to

$$a_c(T) \text{ in pm} = 0.008 \cdot T + 386.9 \quad \text{Eq. 23}$$

Using Eq. 23, the lattice parameter of a hypothetical room temperature form of cubic lushite is estimated to be 389.2 pm at 290 K. The value obtained in this investigation for the cubic

perovskite $\text{Na}_{0.5}\text{NbO}_{2.75}$ is very close to the extrapolated value for the hypothetical room temperature form of a defect free cubic lushite.

The elemental composition of the bluish crystals obtained by microprobe analysis vary from crystal to crystal and imply always too large Na and Nb contents as expected from the variation in lattice parameter values (Eq. 22). This variation may be due to varying intergrowth of bluish and white crystals.

4.4 Characterisation of $\text{Na}_{0.6}\text{Nb}_y\text{W}_{1-y}\text{O}_3$ ($y = 0.0 - 0.15$) system

The X-ray powder diffraction patterns of samples with nominal composition $\text{Na}_{0.6}\text{Nb}_y\text{W}_{1-y}\text{O}_3$ are given in Fig. 37. The samples having nominal composition $y = 0.0$ and 0.05 are pure single phase and could be indexed as PTB_c type phase. The samples with nominal niobium content $y = 0.10, 0.15$ show PTB_c phase and an additional phase, which could be indexed as a non-bronze phase, $\text{Na}_7\text{Nb}_{15}\text{W}_{13}\text{O}_{80}$ (ICSD-30722). For the PTB_c phase Rietveld refinements reveal a very good agreement between the experimental and theoretical pattern using space group Im-3 . The refined lattice parameters (Table 9) show a very less increase in lattice parameters up to $y = 0.05$, and decrease for further increase in y . This increase in lattice parameters could be related to the partial substitution of W by Nb in $\text{Na}_{0.6}\text{Nb}_y\text{W}_{1-y}\text{O}_3$ as reported for $\text{Na}_{0.8}\text{Nb}_y\text{W}_{1-y}\text{O}_3$ series (Debnath *et al.*, 2008a). However, the decrease in lattice parameters as well as appearance and subsequent increase in second phase for $y \geq 0.1$ indicate that further niobium is used for the formation of non-bronze phase and equivalent amount of sodium may also be used by the non-bronze phase under present experimental conditions.

Table 9 List of lattice parameters of nominal $\text{Na}_{0.6}\text{Nb}_y\text{W}_{1-y}\text{O}_3$ samples.

Nominal composition, y	Phase observed	Lattice parameter, $a / \text{\AA}$	Lattice parameter, $a_c = (a/2) / \text{\AA}$
0.00	PTB_c	7.6595 (2)	3.8298 (2)
0.05	PTB_c	7.6599 (2)	3.8300 (2)
0.10	$\text{PTB}_c + \Delta$	7.6566 (3)	3.8283 (3)
0.15	$\text{PTB}_c + \Delta$	7.6541 (2)	3.8271 (2)

Δ = few extra diffraction lines of $\text{Na}_7\text{Nb}_{15}\text{W}_{13}\text{O}_{80}$ phase.

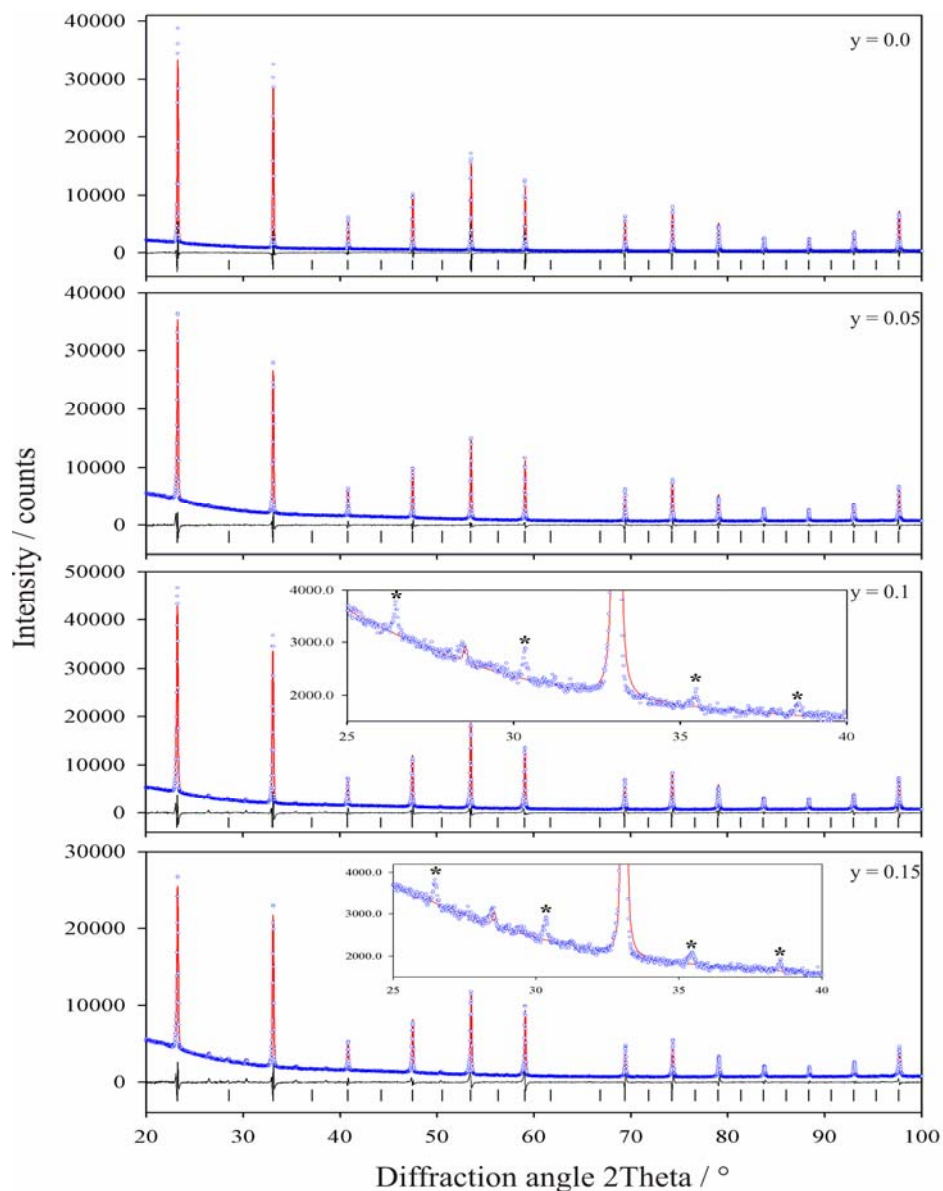


Fig. 37 Rietveld refinement of nominal $\text{Na}_{0.6}\text{Nb}_y\text{Nb}_{1-y}\text{O}_3$ samples (as denoted). The descriptions of the symbols in XRD patterns are same as described in Fig. 20. Samples with nominal composition $y = 0.1$ and 0.15 show (inset, marked as star) the presence of additional phase, which was not included in the refinement.

4.5 Characterization of $K_{0.55}Nb_yW_{1-y}O_3$ ($y = 0.0 - 0.55$) system

The X-ray diffraction patterns of the samples having nominal composition $y = 0.0$, 0.05, and 0.07 show pure single phase and could be indexed as TTB type phase (Fig. 38a-c).

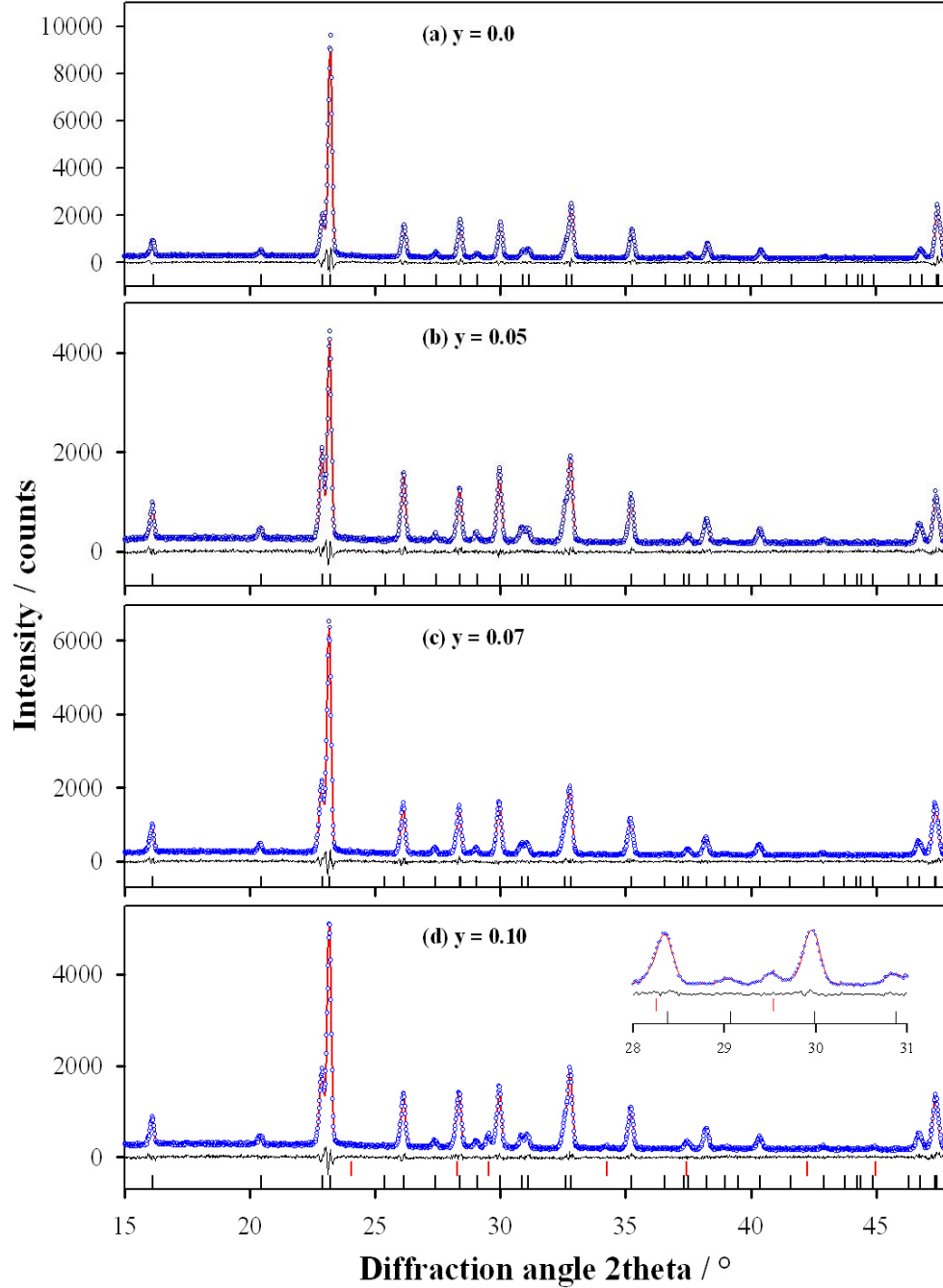


Fig. 38 Observed X-ray diffraction pattern (dotted) and calculated pattern (solid line) using the Rietveld method for samples (a) $y = 0$; (b) $y = 0.05$; (c) $y = 0.07$ and (d) $y = 0.10$. The respective difference curve and indexed peak positions (bars) are also shown. The black and red “bars” show the calculated peak positions of TTB and pyrochlore type phase, respectively. Inset ((c), $y = 0.1$) shows the 222 diffraction line at $2\theta = 29.55^\circ$ for pyrochlore type phase. Rietveld refinements were done in whole measured range ($2\theta = 10 - 100^\circ$).

The samples with nominal niobium content $0.10 \leq y \leq 0.40$ show TTB phase and also an additional phase, which could be indexed as a cubic pyrochlore type phase (ICDD 21-1003) (Raveau *et al.*, 1968) (Fig. 38d). For $y = 0.50$ and 0.55 samples TTB phase was absent. Here a mixture of cubic pyrochlore type phase and a non-bronze phase ($\text{K}_2(\text{NbO})_2\text{Si}_4\text{O}_{12}$, ICSD-72111) was identified. For the TTB phase Rietveld refinements reveal a very good agreement between the experimental and theoretical pattern using space group P4/mbm supporting earlier results for TTB phases of composition K_xWO_3 (Hussain, 1978). Data of present investigation show that Nb substituted forms are isostructural with the TTB phase. As a typical example, the detail of the structural parameters, obtained for the sample $y = 0.07$ by Rietveld method, are given in Table 10 and Table 11.

Table 10 Crystallographic data for $\text{K}_{0.47}\text{Nb}_{0.07}\text{W}_{0.93}\text{O}_3$. *Rp*, *Rwp* and *GOF* refer to the Rietveld criteria of fit as defined in the manual of the “TOPAS Diffrac Plus” program.

Formula	$\text{K}_{0.47}\text{Nb}_{0.07}\text{W}_{0.93}\text{O}_3$
Temperature [K]	298
Space group	P4/mbm
Z	10
a [Å]	12.2826(3)
b [Å]	12.2826(3)
c [Å]	3.8332(1)
V [Å ³]	578.275(29)
ρ -cal [g/cm ³]	6.8680(4)
2 θ range [°]	10-100
Step size [°2 θ]	0.02
Wavelength [Å]	CuK α radiation
Rp	6.15 %
Rwp	7.81 %
GOF	1.26

Table 11 Atomic coordinates and displacement parameter of $\text{K}_{0.47}\text{Nb}_{0.07}\text{W}_{0.93}\text{O}_3$.

Atom	Site	x	y	z	Occ.	B _{iso}
K	2a	0.00000	0.00000	0.00000	0.207(2)	2.78(3)
K	4g	0.1723(6)	0.6723(6)	0.00000	0.982(3)	2.78(3)
W	2c	0.00000	0.50000	0.50000	0.907(6)	1.458(4)
W	8j	0.0754(1)	0.2080(1)	0.50000	0.891(7)	1.458(4)
Nb	2c	0.00000	0.50000	0.50000	0.0931	1.458(4)
Nb	8j	0.0754(1)	0.2080(1)	0.50000	0.1093	1.458(4)
O	2d	0.00000	0.50000	0.00000	1	2.04(2)
O	8i	0.0740(2)	0.2103(15)	0.00000	1	2.04(2)
O	4h	0.2899(2)	0.7899(14)	0.50000	1	2.04(2)
O	8j	0.9980(10)	0.3485(17)	0.50000	1	2.04(2)
O	8j	0.1457(2)	0.0754(21)	0.50000	1	2.04(2)

A distorted cubic pyrochlore type phase along with TTB found as second phase in the XRD pattern of nominal compositions $y \geq 0.1$ was included in the refinement using space group $Fd\bar{3}m$ (Fig. 38d). The XRD patterns of other samples with nominal composition $y = 0.2, 0.25, 0.3, 0.35, 0.4, 0.5$, and 0.55 is shown in Fig. 39. The XRD patterns of samples with nominal composition $K_{0.55}WO_3$ (i.e., $y = 0$) and $KNbWO_6$ are also included in Fig. 39. The results of quantitative Rietveld refinement with estimated weight fraction of different phases are listed in Table 12.

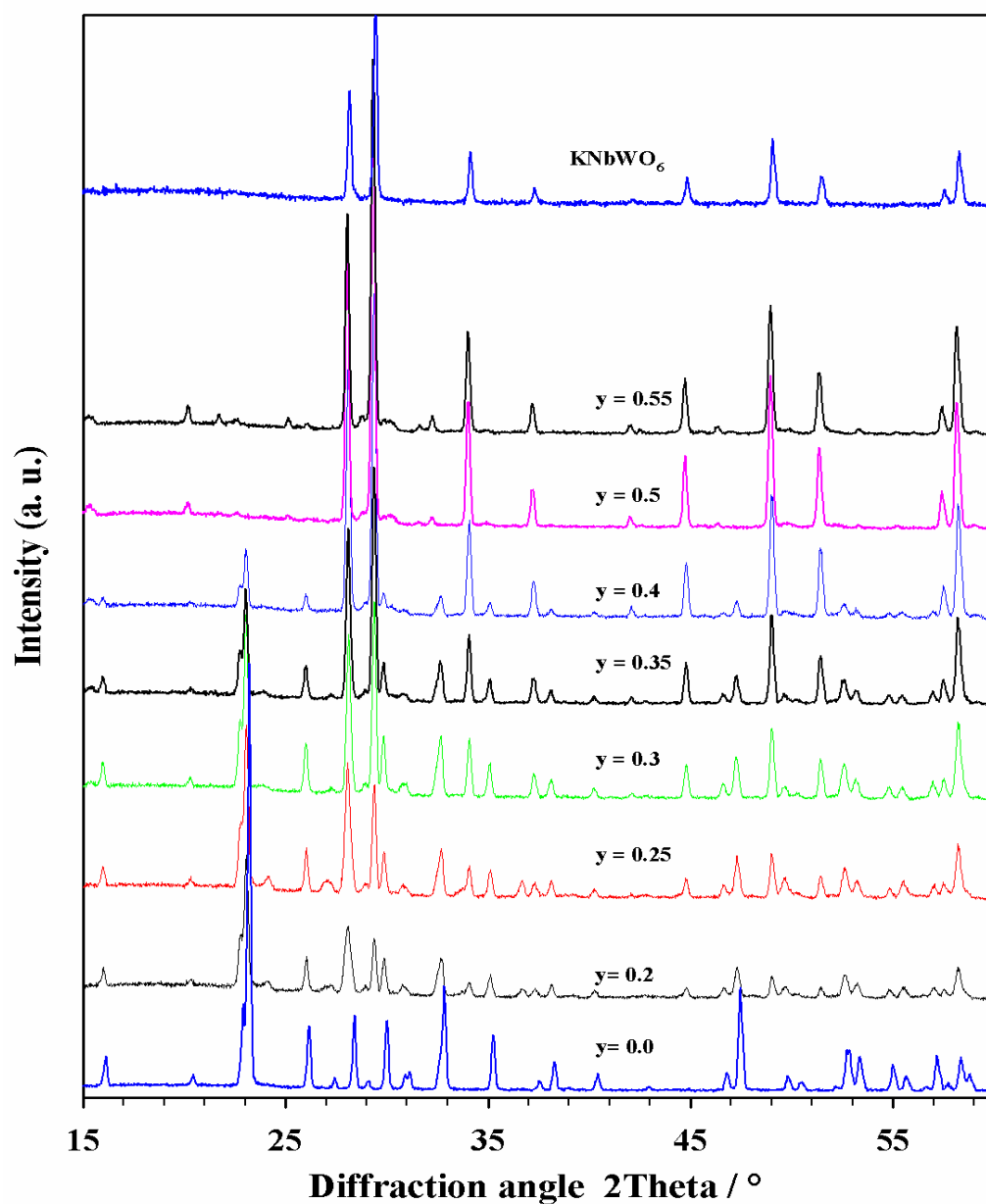


Fig. 39 The XRD patterns of $KNbWO_6$ and samples with nominal composition $y = 0.0, 0.2, 0.25, 0.3, 0.35, 0.4, 0.5$, and 0.55 .

Table 12 Collection of cell parameters and microprobe analysis of nominal $K_xNb_yW_{1-y}O_3$ system.

Composition x		Composition y		Crystal structure	Lattice parameter (Diffractometer)		Lattice parameter (Guinier)	
Nominal	Microprobe	Nominal	Microprobe		$a / \text{\AA}$	$c / \text{\AA}$	$a / \text{\AA}$	$c / \text{\AA}$
0.55	0.46(1)	0.00	0.0	TTB (single phase)	12.2647(3)	3.8271(1)	12.278(1)	3.8288(8)
0.55	0.46(2)	0.05	0.03(1)	TTB (single phase)	12.2798(4)	3.8318(1)	12.295(2)	3.8354(2)
0.55	0.47(1)	0.07	0.07(2)	TTB (single phase)	12.2826(3)	3.8332(1)	12.296(1)	3.8363(8)
0.55	0.48(1)	0.10	0.06(2)	TTB (about 94%),	12.2823(4)	3.8332(2)	-	-
	0.47(3)		0.49(2)	Cubic (about 6%),	10.4883(4)	-	-	-
0.55	0.46(3)	0.15	0.06(2)	TTB (about 90%),	12.2810(5)	3.8336(4)	-	-
	0.46(3)		0.48(2)	Cubic (about 10%),	10.4879(6)	-	-	-
0.55	0.47(2)	0.20	0.05(2)	TTB (about 55%),	12.2656(6)	3.8304(2)	-	-
	0.47(2)		0.49(2)	Cubic (about 45%),	10.4790(5)	-	-	-
0.55	-	0.25	-	TTB (about 48%),	12.2691(5)	3.8298 (3)	-	-
	-		-	Cubic (about 52%),	10.4757(4)	-	-	-
0.55	0.46(2)	0.30	0.06(2)	TTB (about 44%),	12.2812(5)	3.8340(7)		
	0.48(2)		0.48(3)	Cubic (about 56%),	10.4780(6)			
0.55	-	0.35	-	TTB (about 32%),	12.2804(5)	3.8345(5)		
	-		-	Cubic (about 68%),	10.4799(3)	-		
0.55	0.46(2)	0.40	0.06(2)	TTB (about 15%),	12.2791(9)	3.8341(4)		
	0.47(2)		0.49(2)	Cubic (about 85%),	10.4811(3)	-		

The unit cell parameters of the corresponding samples are also given in Table 12. There is a slight increase in lattice parameters with increasing Nb content. The values obtained from the diffractometer data are systematically less by about 1 pm than that of the Guinier data. Such deviations are generally accepted when cell parameters are determined from these two methods.

Scanning electron microscopy (SEM) images (Fig. 40) show crystallites with rectangular morphology are clearly visible in the images. The maximum size of the rectangular crystals is up to $5 \mu\text{m} \times 5 \mu\text{m} \times 40 \mu\text{m}$. The SEM images of the sample with nominal $y \geq 0.10$ shows some additional octahedral shaped crystals up to $10 \mu\text{m}$ size edges. It is observed that the octahedral shaped crystals are pyrochlore type phase.

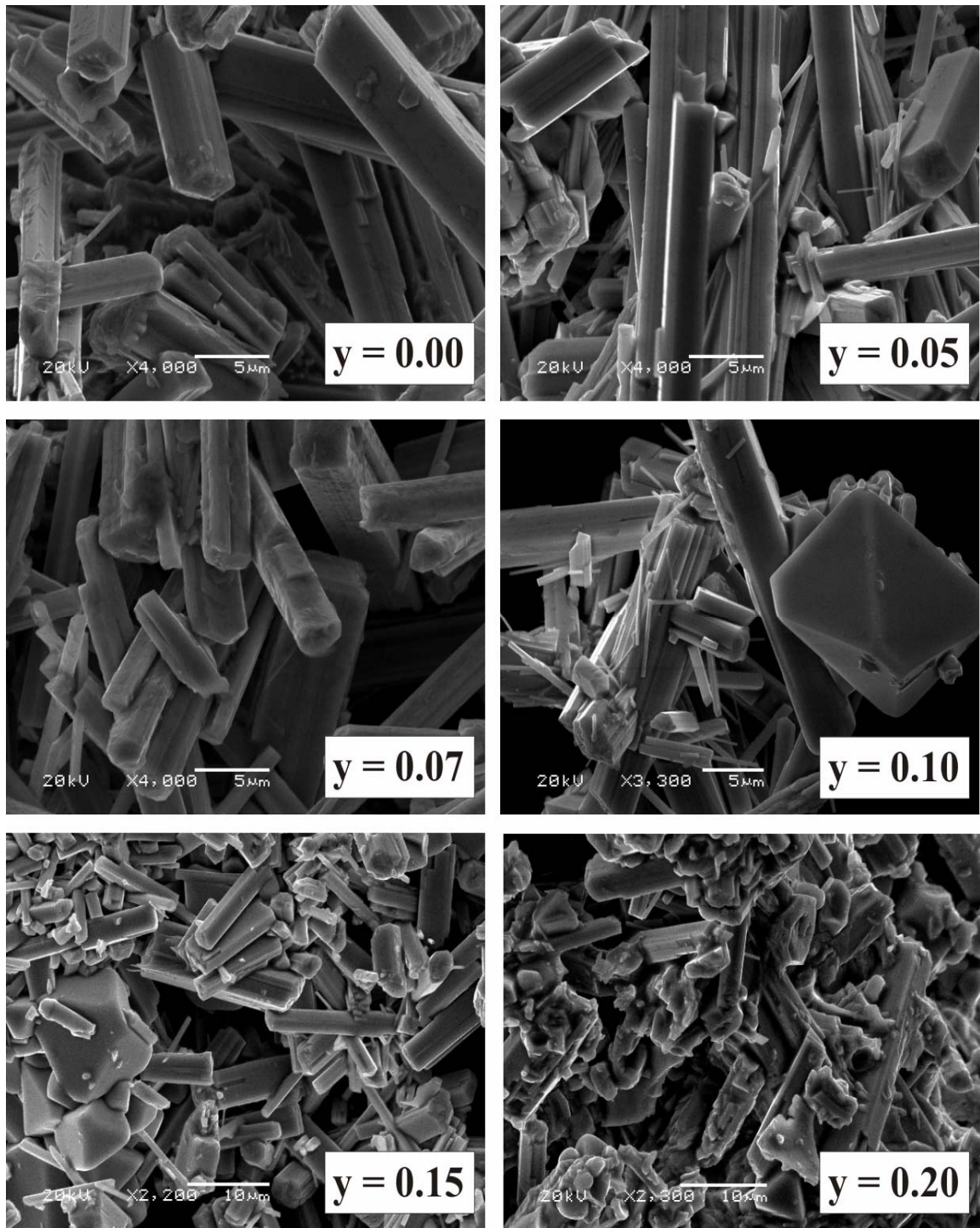


Fig. 40a Scanning electron micrograph (SEM) of $K_{0.55}Nb_yW_{1-y}O_3$ ($y = 0.0, 0.05, 0.07, 0.10, 0.15$, and 0.20) samples showing typical TTB phase (needle type crystals) in all compositions but pyrochlore type phase (octahedral shaped crystals) can be seen only when gross composition, $y \geq 0.1$.

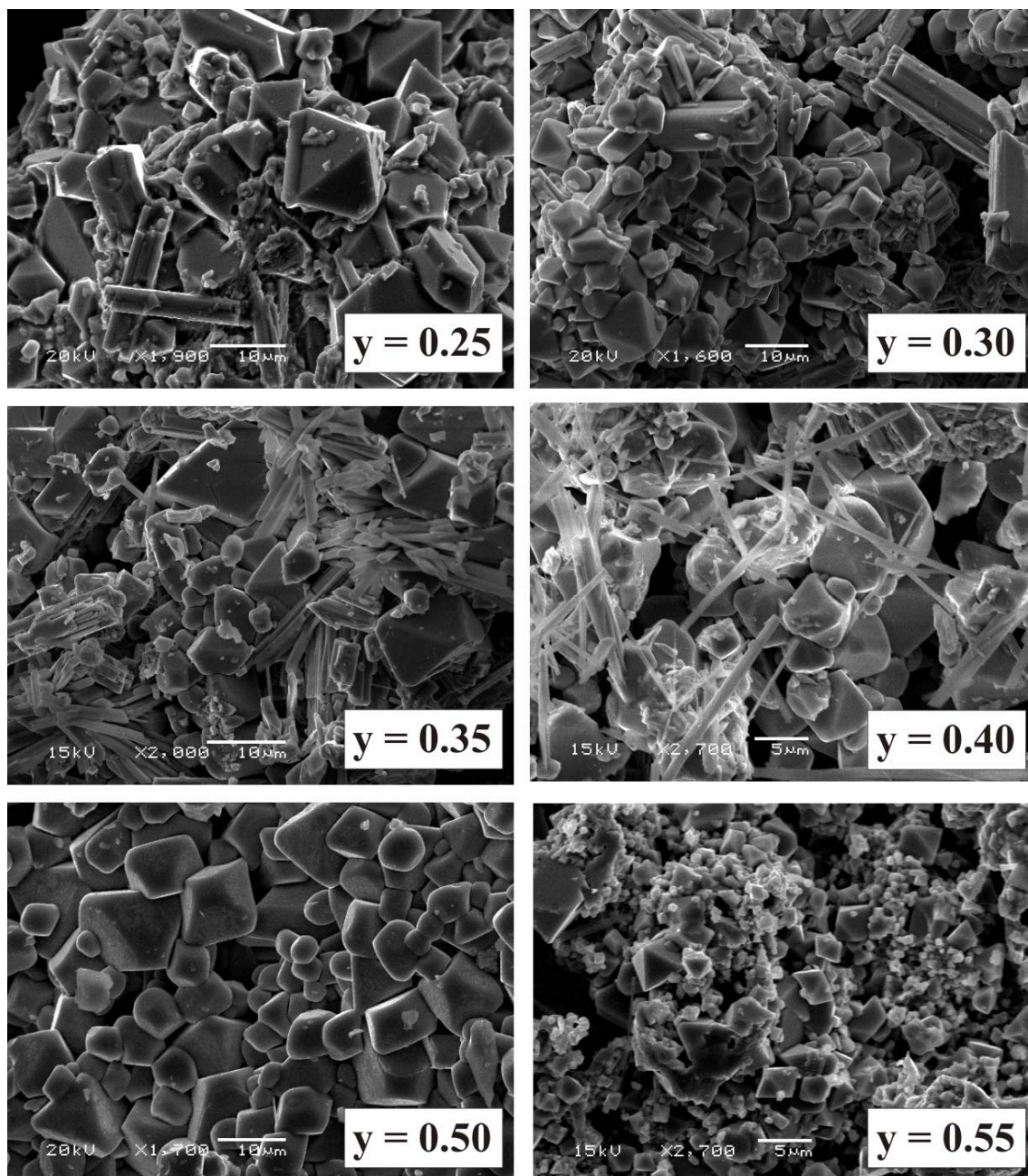


Fig. 40b Scanning electron micrograph (SEM) of samples with nominal composition $K_{0.55}Nb_yW_{1-y}O_3$ ($y = 0.25, 0.30, 0.35, 0.40, 0.50, \text{ and } 0.55$).

The results of microprobe analysis are given in Table 12. The experimental Nb content of the TTB phase fits well with the nominal composition of the samples up to $y = 0.07$. The samples with nominal composition $y > 0.07$ show Nb content is about 0.06(2) for the needle shaped crystals, which supports that the maximum amount of doped Nb is about 0.07(2) in TTB phase. The pyrochlore type crystals (octahedral shape crystals) show Nb content 0.49(2). The potassium contents range in all cases between 0.46 - 0.48, which is systematically lower than the nominal value (0.55) implying a systematical loss during synthesis. The potassium content

(TTB phase, $y = 0.0$) calculated from the cell parameters (Magnéli, 1949 and Hussain, 1978) is between 0.45 - 0.50, which is also a bit less than the nominal composition, $x = 0.55$. An increase in lattice parameter values with increasing amount of substitution of Nb^{5+} or Ta^{5+} has been observed in cubic perovskite tungsten bronzes, $\text{Na}_x\text{Nb}_y\text{W}_{1-y}\text{O}_3$ and $\text{Na}_x\text{Ta}_x\text{W}_{1-y}\text{O}_3$ (Miyamoto *et al.*, 1983; Debnath *et al.*, 2008a; Dubson *et al.*, 1985). This trend is also observed in $\text{K}_x\text{Nb}_y\text{W}_{1-y}\text{O}_3$, too. The composition found for the pyrochlore type phase (ICDD 21-1003) from the microprobe analysis is $\text{K}_{0.47(3)}\text{Nb}_{0.49(2)}\text{W}_{0.51(2)}\text{O}_3$. Taking into account the standard deviation of the microprobe analysis, the composition may be written as $\text{K}_{0.50}\text{Nb}_{0.50}\text{W}_{0.50}\text{O}_3$ ($\equiv \text{KNbWO}_6$). The formation of pyrochlore type phase in this field is not unexpected and has been reported during the synthesis of bronzoid type phase, too (Deschanvres *et al.*, 1968; Raveau *et al.*, 1968; Darriet *et al.*, 1970).

The VIS-NIR reflectivity of the samples was measured in the spectral range between 8500 and 20000 cm^{-1} .

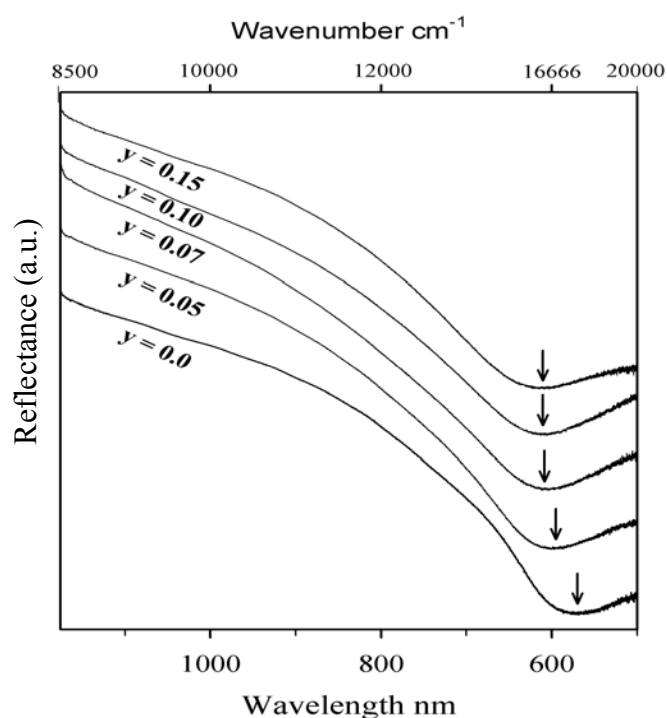


Fig. 41 VIS-NIR reflectivity spectra of powder samples showing the shift of minima towards the low wavenumber (as marked with arrow) with increasing Nb content up to $y = 0.07$. The spectra are shifted vertically for the sake of clarity.

The pure TTB (i.e. $y = 0$) sample shows a pronounced minimum at about 17500 cm^{-1} together with a sharp increase in reflectivity towards lower wavenumber (Fig. 41). For $y = 0.05$ and 0.07 sample the minima position is shifted to about 16700 and 16400 cm^{-1} , respectively. The position of the minima for the $y = 0$ sample is in very good agreement with the minima reported earlier (Hussain *et al.*, 1997) for K-TTB single crystals of composition $\text{K}_{0.5}\text{WO}_3$ for the

electrical field polarized parallel to the c axis ($E//c$). Having the potassium content fixed as authenticated by microprobe for the series here the shift of the reflectivity minima towards lower wavenumber can entirely be related to the effect of Nb substitution which thus decreases the effective amount of W^{5+} . Similar effect has been reported by Hussain *et al.* (2002) for $Rb_xNb_yW_{1-y}O_3$ HTB system. In a simple free carrier picture for a rigid lattice, the position of the reflectivity minimum related to the plasma edge of the carriers is proportional to the square root of the relative charge carrier concentration (Eq. 24).

$$\omega_p = \sqrt{\frac{Ne^2}{m^* \epsilon_\infty}} \quad \text{Eq. 24}$$

(ω_p = plasma frequency, N = concentration of carriers, e = charge of electron, m^* = effective electron mass, and ϵ_∞ = effective high frequency dielectric constant.)

The effect of Nb doping may be written formally as $K_x(Nb^{5+}_y W^{5+}_{x-y} W^{6+}_{1-x})O_3$. Considering the chemical formula for sample with nominal composition $y = 0.07$ ($\equiv K_{0.5}Nb^{5+}_{0.07}W^{5+}_{0.43}W^{6+}_{0.5}O_3$), the concentration of effective charge carriers would be 0.43 (i.e., $x-y$). Thus, for a counterdoping effect of $y = 0.07$ a shift of the minima by a factor of $(0.43/0.5)^{1/2}$ can be expected for $K_{0.5}Nb_{0.07}W_{0.93}O_3$, i.e. to about 16230 cm^{-1} which is close to the value observed experimentally. For the $y \geq 0.1$ samples, no further shift is observed indicating that a maximum of counterdoping effect has been reached for y less than 0.1.

Fig. 42 shows the IR spectra of nominal $K_{0.55}Nb_yW_{1-y}O_3$ series, where the samples $0.0 \leq y \leq 0.07$ show the characteristic increase, typical for metallic samples (e.g. ReO_3) (Feinleib *et al.*, 1968), which could be explained as proportional to $(1-R)$, where R is the Drude reflectivity. Similar results has been reported for Nb doped HTB system (Hussain *et al.*, 2002). The appearance of broad peak for nominal $y \geq 0.10$ is due to the systematic development of second phase (pyrochlore type, $KNbWO_6$) (see XRD results, Table 12). For direct comparison, the IR absorption spectrum of pure $KNbWO_6$ phase is included in Fig. 42a. Calculated IR absorption spectrum using the as measured IR absorption spectra of 90 % pure TTB ($y = 0.07$) + 10% pure $KNbWO_6$ generate almost similar feature as for the IR absorption spectrum of nominal $y = 0.15$ (Fig. 42a), which support the XRD results where a mixture of about 90 % TTB and 10 % $KNbWO_6$ has been estimated (Table 12). The IR absorption peaks of pure $KNbWO_6$ centered at about 650 cm^{-1} is due to the M-O ($M = Nb$ or W) stretching mode, which can be compared with the IR absorption spectrum of $NaNbWO_6$ (Kuhn *et al.*, 2004). The absorption peaks below 450 cm^{-1} is likely to be due to the bending mode of M-O. The samples $y = 0.50$ and 0.55 show two additional peaks at about 1000 and 1200 cm^{-1} which could be related to $K_2(NbO)_2Si_4O_{12}$ phase (formed due to the silica attack from silica glass tube) as observed in XRD patterns.

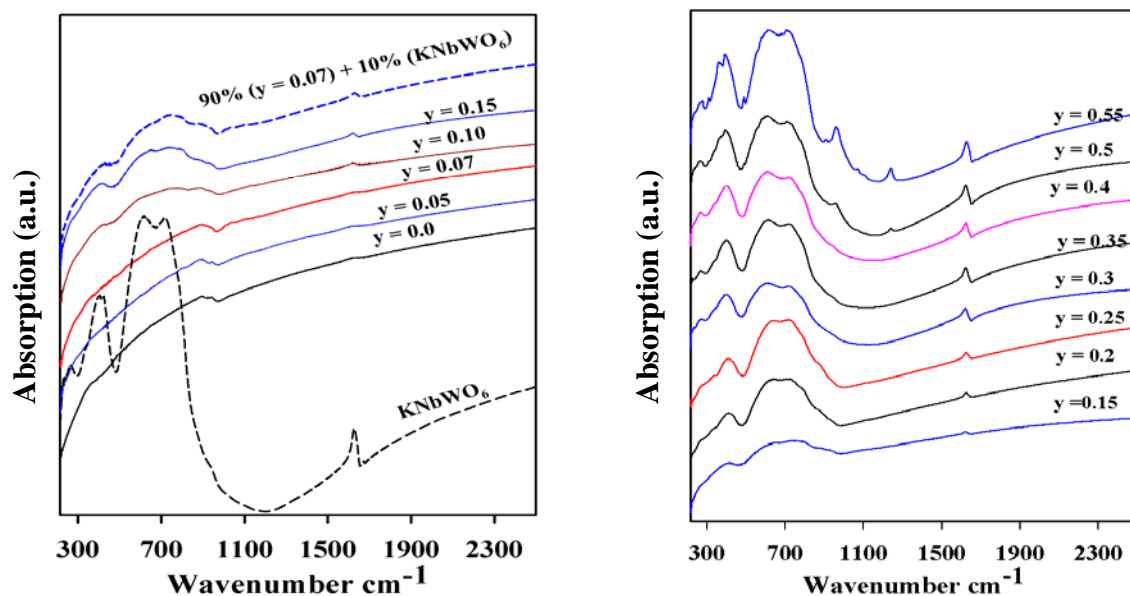


Fig. 42 IR absorption spectra (KBr-method) of nominal $K_{0.55}Nb_yW_{1-y}O_3$ series. The spectra are shifted vertically for the sake of clarity. The broad peaks below 1000 cm^{-1} for samples $y \geq 0.1$ is due to the presence of pyrochlore type phase. (a) The IR absorption spectrum of pure $KNbWO_6$ is also included (as denoted). Calculated spectrum (as denoted), adding as measured spectra of 90% ($y = 0.07$) + 10% $KNbWO_6$, shows similar IR absorption feature of nominal $y = 0.15$ sample. (b) The spectra of samples of nominal composition $y = 0.0 - 0.55$, where $y = 0.5$ and 0.55 samples show some additional peaks (as denoted), which may be due to the presence of $K_2(NbO)_2Si_4O_{12}$ phase.

Optical micrographs of polished samples show (Fig. 43) the presence of additional “white crystallites” for nominal $y \geq 0.1$, which are related to the formation of pyrochlore type phase as explained before (by XRD, Microprobe, IR absorption spectra). The needle shaped red and blue crystallites are from the same TTB phase. This pleochroism coincides with the strong anisotropy in optical properties as observed for single crystal K_xWO_3 (TTB) (Hussain *et al.*, 1997). The optical micrographs confirm that the limit of TTB phase formation is in between $y = 0.4$ and 0.50 as the photograph for $y = 0.5$ does not show any blue or red crystallites as observed by XRD pattern of $y = 0.5$ sample (compare Fig. 39, Table12).

The micro-reflectivity of “white crystallites” measured on polished samples for nominal composition $y \geq 0.10$ are shown in Fig. 44. The spectra are identical in all samples. The phonon peak with maximum at about 745 cm^{-1} can be assigned to the M-O ($M = Nb/W$) stretching mode.

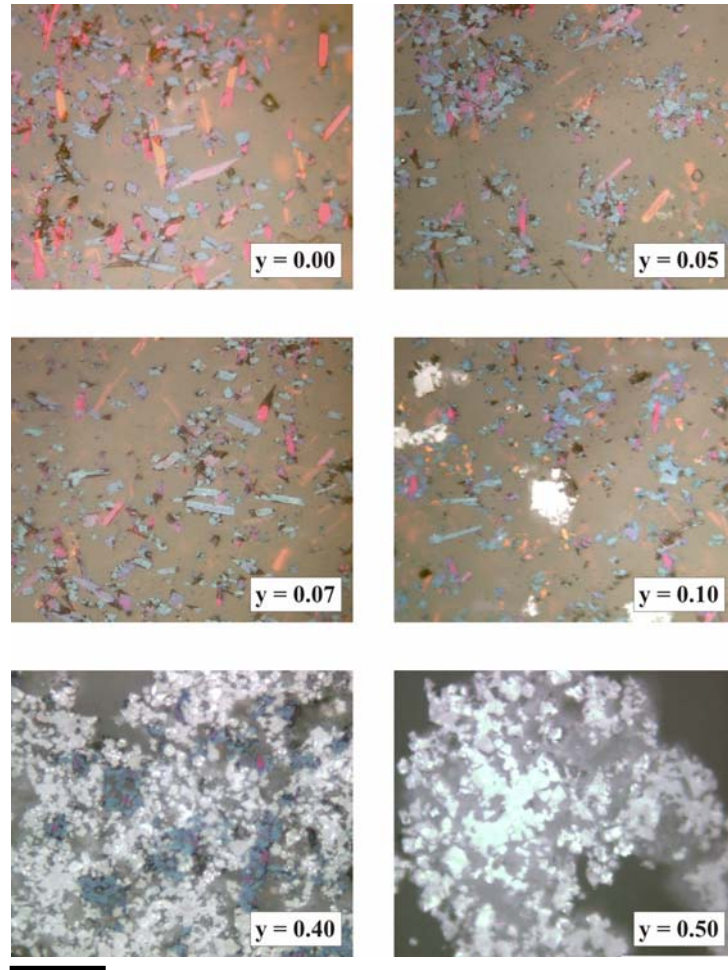


Fig. 43 Optical micrograph of polished samples of nominal compositions $K_{0.55}Nb_yW_{1-y}O_3$. The “white crystallites” for nominal $y \geq 0.1$ shows the presence of pyrochlore type phase. The needle shaped red and blue crystallites are from the same TTB phase. This pleochroism is due to the strong anisotropy in optical properties as observed for single crystal K_xWO_3 (TTB) (Hussain et al., 1997). The stability limit of TTB phase formation is in between $y = 0.4$ and 0.50 as the photograph for $y = 0.5$ does not show any blue or red crystallites. The scale bar is $50 \mu m$.

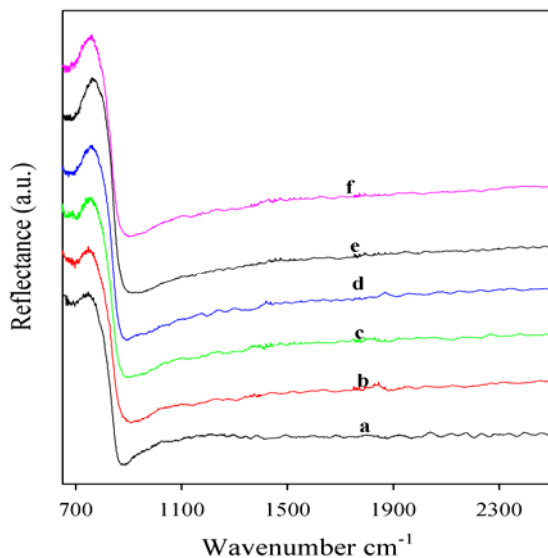


Fig. 44 Micro-reflectivity spectra of “white crystallites” (pyrochlore type phase) observed within samples (a) $y = 0.1$, (b) $y = 0.15$, (c) $y = 0.2$, (d) $y = 0.3$, (e) $y = 0.4$, and (f) $y = 0.5$. The spectra are shifted vertically for the sake of clarity.

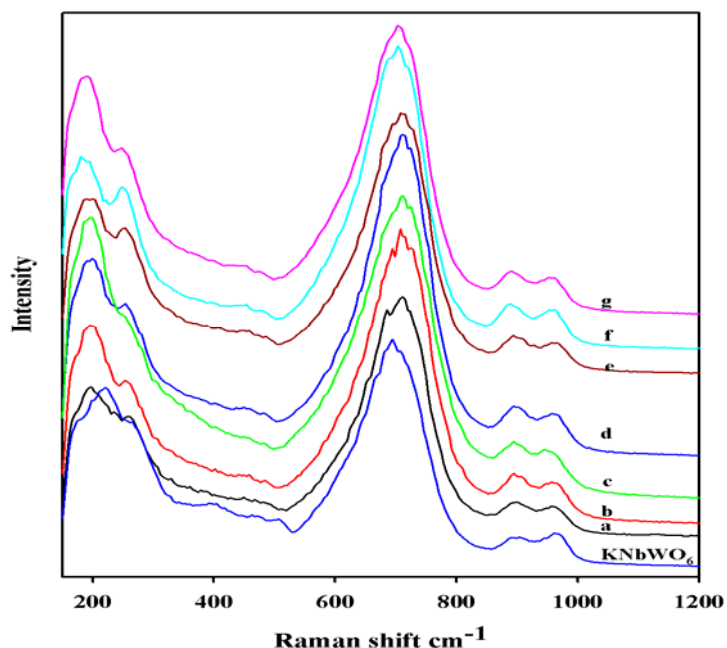


Fig. 45 Raman spectra of “white crystallites” (pyrochlore type phase) of samples with nominal (a) $y = 0.1$, (b) $y = 0.15$, (c) $y = 0.2$, (d) $y = 0.3$, (e) $y = 0.4$, and (f) $y = 0.5$. Raman spectrum of KNbWO_6 is also included (as denoted). The spectra are shifted vertically for the sake of clarity.

The Raman spectra of “white crystallites” (Fig. 45) are characteristic for KNbWO_6 . For direct comparison, the Raman spectrum of single phase KNbWO_6 is included in Fig. 45. Moreover, the main peaks in Raman spectrum of pyrochlore type phase can be described considering the Raman study of NaNbWO_6 , $\text{Na}_{1.2}\text{Nb}_{1.2}\text{W}_{0.8}\text{O}_6$, and KNbW_2O_9 from the literatures (Kuhn *et al.*, 2004; Sanjuán *et al.*, 2008; Maczka *et al.*, 2001). The Raman peak above 900 cm^{-1} can be assigned to the stretching mode of terminal $-\text{M}=\text{O}$ ($\text{M} = \text{Nb}/\text{W}$) bonds. The highest intense peak at about 700 cm^{-1} and the peaks below 450 cm^{-1} can be assigned to the stretching and bending modes of MO_6 octahedra, respectively.

4.6 Polarized micro-reflectivity of HTB $M_x\text{WO}_3$ single crystals ($M = \text{K}, \text{Cs}$ and $x = 0.20, 0.25$) and Kramers-Kronig analysis

The reflectivity spectra for the electric field polarized parallel ($E \parallel c$) and perpendicular ($E \perp c$) to the c -axis (needle-axis) for $M_x\text{WO}_3$ ($M = \text{K}, \text{Cs}$ and $x = 0.20, 0.25$) crystals are shown in Fig. 46. The direction of the c -axis is along the direction of the needle type crystal as shown in inset in Fig. 46. Measured range is as denoted in the figures. The spectra have been extended down to 550 cm^{-1} with more sophisticated detector system. Good agreement with the data given by Hussain *et al.* (1997) was obtained in the range between 1000 and 4000 cm^{-1} .

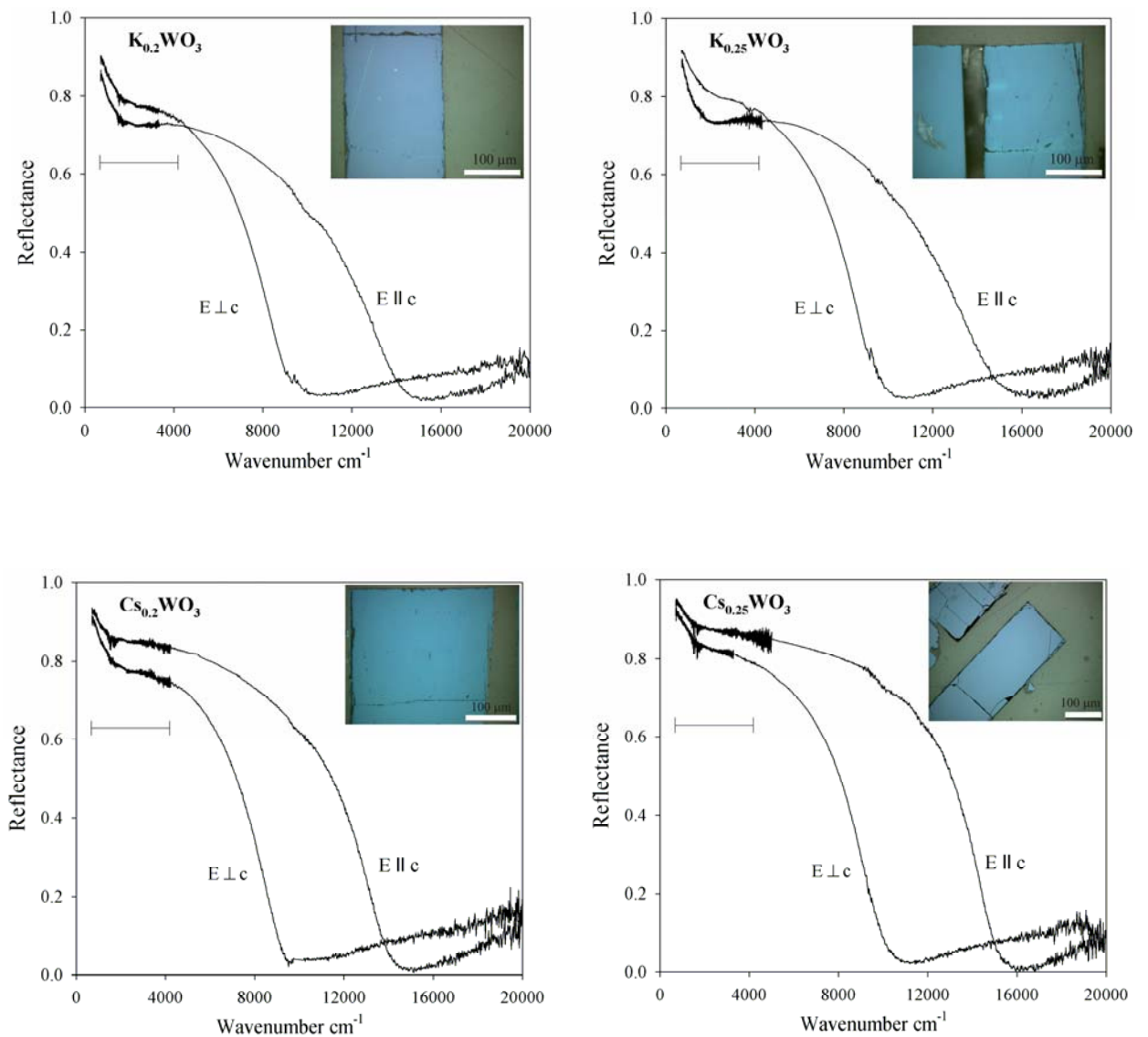


Fig. 46 Polarized reflectivity spectra of $M_x\text{WO}_3$ ($M = \text{K}, \text{Cs}$ and $x = 0.20, 0.25$) crystals (as denoted). Inset show the optical micrograph of corresponding crystals (as denoted).

These reflectivity spectra were further analyzed with Kramers-Kronig transformation (as explained in data evaluation part of the experimental section) and Drude-Lorentz oscillator fitting procedure. The results are shown in Fig. 47 - 54 along with the fitted curves reported earlier (Hussain *et al.*, 1997).

The reflectivity $R(\omega)$ measured parallel to the c axis ($E \parallel c$) of $K_{0.25}WO_3$ (Fig. 47a) exhibits a metallic-like behavior with a well defined pseudo-plasma edge around 16000 cm^{-1} . A tentative plot of reflectivity taking the parameters reported by Hussain *et al.* (1997) using Drude model for free carriers (black curve) as well as a completely over damped oscillator (blue curve) is shown in Fig. 47a. It is seen that only for $\omega > 5000 \text{ cm}^{-1}$, the calculated reflectivity fits well both with Drude free carriers and oscillator description. For $\omega < 5000 \text{ cm}^{-1}$, a significant deviation between the fit results by Hussain *et al.* (1997) and the experimental data are observed.

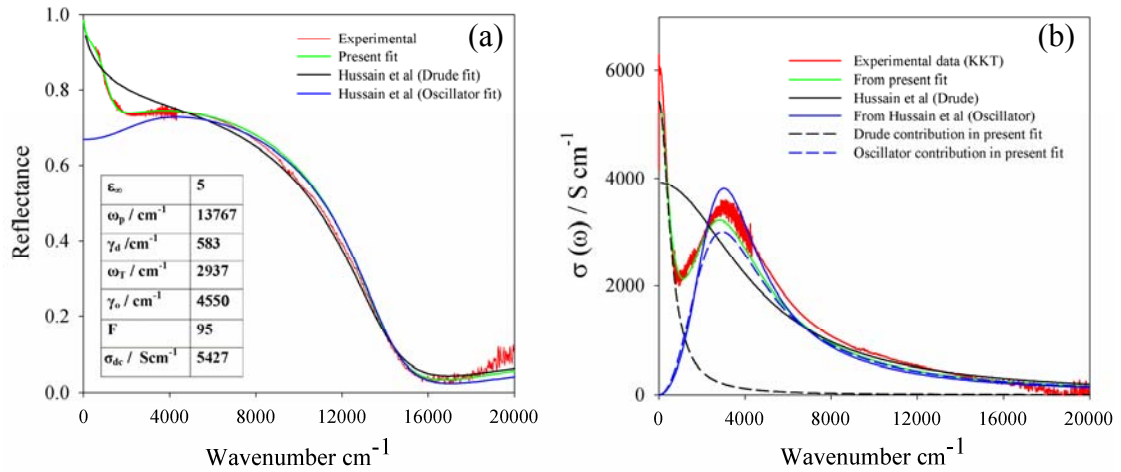


Fig. 47 (a) $E \parallel c$ reflectivities of $K_{0.25}WO_3$: experimental (red curve), Drude fit by Hussain *et al.* (1997) (black curve), oscillator fit by Hussain *et al.* (1997) (blue curve), and Drude-Lorentz oscillator fit in this work (green curve). (b) The frequency dependence of the conductivities of $K_{0.25}WO_3$ for $E \parallel c$ direction: obtained after KKT of extrapolated experimental reflectivity (red curve), Drude fit (black curve), oscillator fit (blue curve), Drude-Lorentz oscillator fit (green curve), contribution of oscillator part of Drude-Lorentz oscillator fit (dashed black curve), and Drude part of Drude-Lorentz oscillator fit (dashed pink curve).

The fit result can be improved considerably (as shown in Fig. 47, present fit) by considering a combination of a Drude plasma edge in the low frequency region and an over damped oscillator with eigen frequency in the mid-infrared region. This result has been achieved calculating the frequency dependence of the conductivity $\sigma(\omega)$ (Fig. 47b.) from the experimental $R(\omega)$ by usual Kramers-Kronig transformations. The separated contribution of optical conductivity of Drude

part (dashed black curve) and oscillator part (dashed pink curve) as well as fit parameters values are also shown in Fig. 47b. There is a clear change of slope in $R(\omega)$ around 2000 cm^{-1} , which directly motivates the separation into two different contributions to $\sigma(\omega)$.

Similar results are obtained for the reflectivity $R(\omega)$ measured perpendicular to the c axis ($E \perp c$) of $\text{K}_{0.25}\text{WO}_3$ (Fig. 48a). A tentative plot of the reflectivity using Drude model for free carriers (black curve) as well as an over damped oscillator (blue curve) is shown in Fig. 48a along with the fit parameters values. Also here a separation into two contributions (Fig. 48a and b), i.e., a low lying Drude free carrier contribution and a highly damped oscillator function is clearly obtained using the present analyzing method.

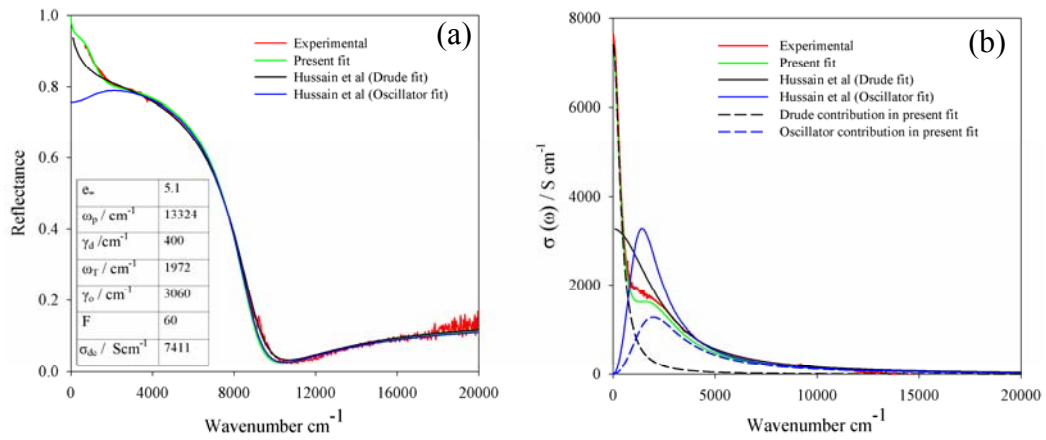


Fig. 48 Reflectivities (a), and the frequency dependence of the conductivities (b) of $\text{K}_{0.25}\text{WO}_3$ crystal for $E \perp c$ direction. The symbols are same as described for Fig. 47.

The polarized micro-reflectivity spectra of other investigated HTB samples (e.g., $\text{K}_{0.2}\text{WO}_3$, $\text{Cs}_{0.25}\text{WO}_3$ and $\text{Cs}_{0.2}\text{WO}_3$) have also been analyzed using same technique as described for $\text{K}_{0.25}\text{WO}_3$ sample.

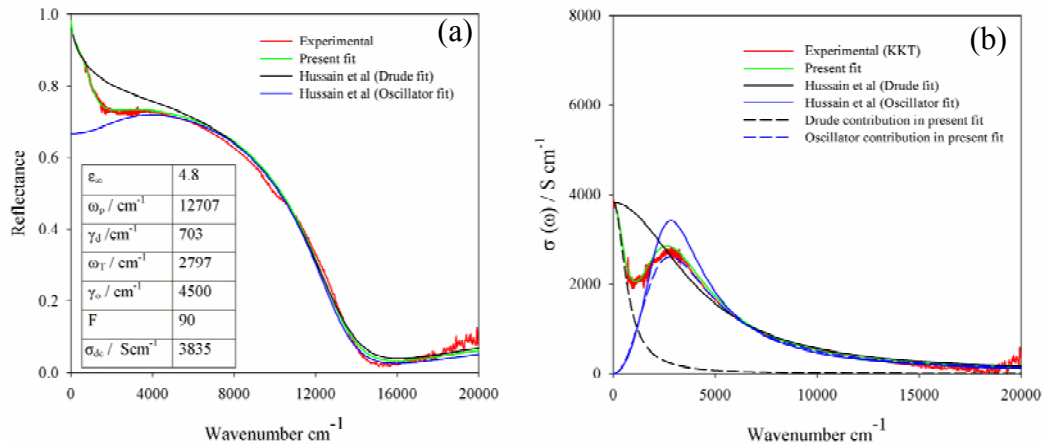


Fig. 49 Reflectivities (a), and the frequency dependence of the conductivities (b) of $\text{K}_{0.20}\text{WO}_3$ crystal for $E \parallel c$ direction. The symbols are same as described for Fig. 47.

Fig. 49, 50, 51, 52, 53, and 54 show the tentative plot of the reflectivities using data from literature (Hussain *et al.*, 1997) as well as present fit considering a combination of a Drude plasma edge and an over damped oscillator for samples $K_{0.2}WO_3$, $Cs_{0.25}WO_3$, and $Cs_{0.2}WO_3$, respectively along with the corresponding fit parameters values. Hussain *et al.* (1997) did not consider the oscillator fit for Cs_xWO_3 series. Attempts was also taken to describe the measured reflectivity using oscillator model only, which, however, does not fit in MIR region.

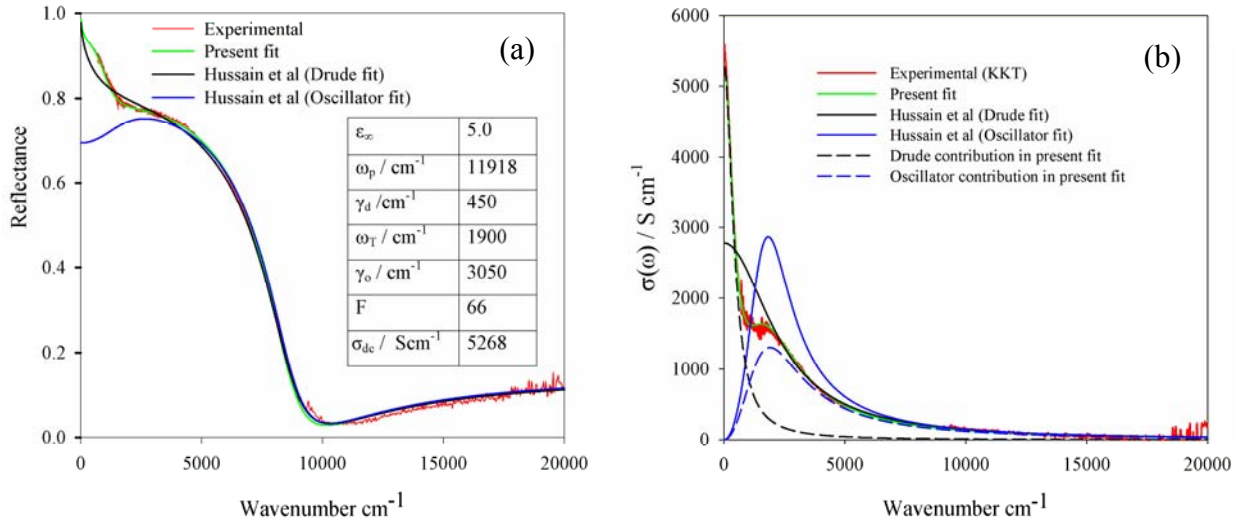


Fig. 50 Reflectivities (a), and the frequency dependence of the conductivities (b) of $K_{0.20}WO_3$ crystal for $E \perp c$ direction. The symbols are same as described for Fig. 47.

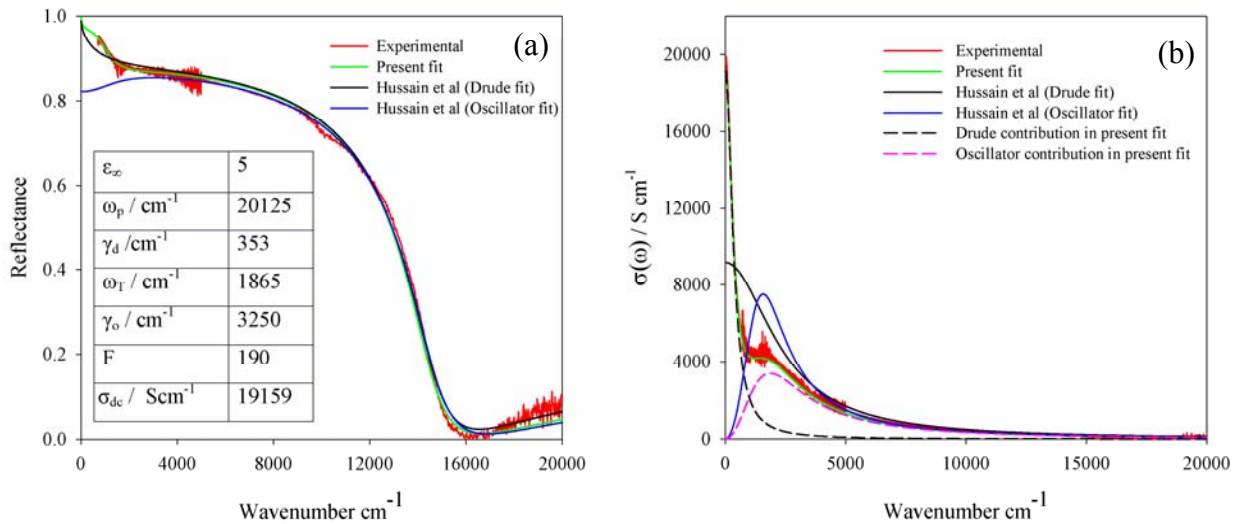


Fig. 51 Reflectivities (a), and the frequency dependence of the conductivities (b) of $Cs_{0.25}WO_3$ crystal for $E \parallel c$ direction. The symbols are same as described for Fig. 47.

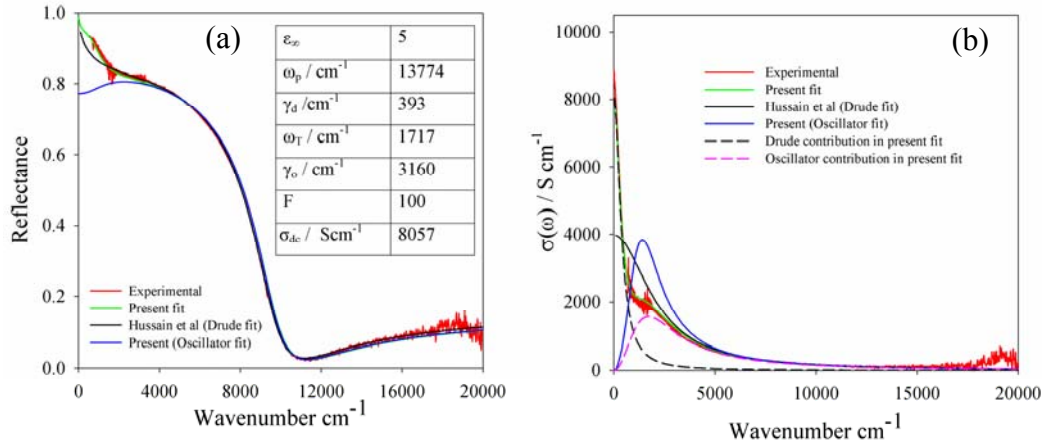


Fig. 52 Reflectivities (a), and the frequency dependence of the conductivities (b) of $\text{Cs}_{0.25}\text{WO}_3$ crystal for $E \perp c$ direction. The symbols are same as described for Fig. 47.

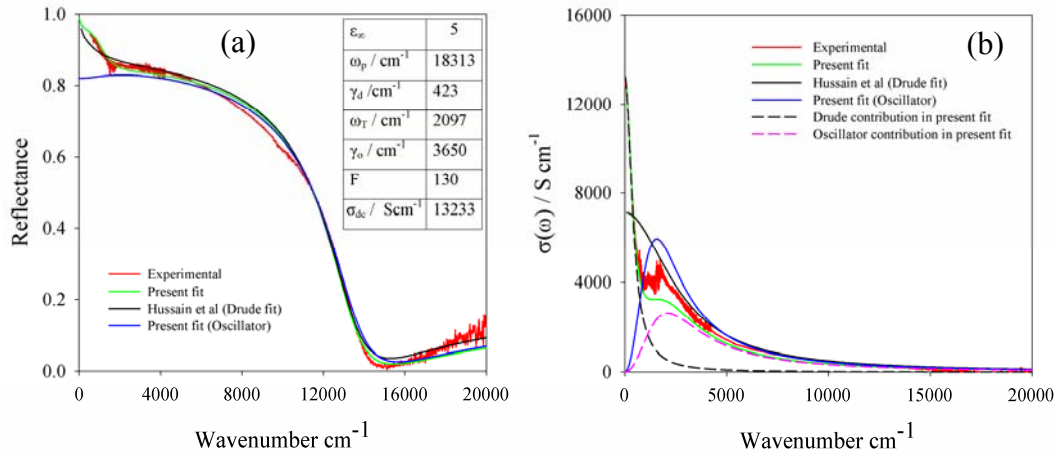


Fig. 53 Reflectivities (a), and the frequency dependence of the conductivities (b) of $\text{Cs}_{0.2}\text{WO}_3$ crystal for $E \parallel c$ direction. The symbols are same as described for Fig. 47.

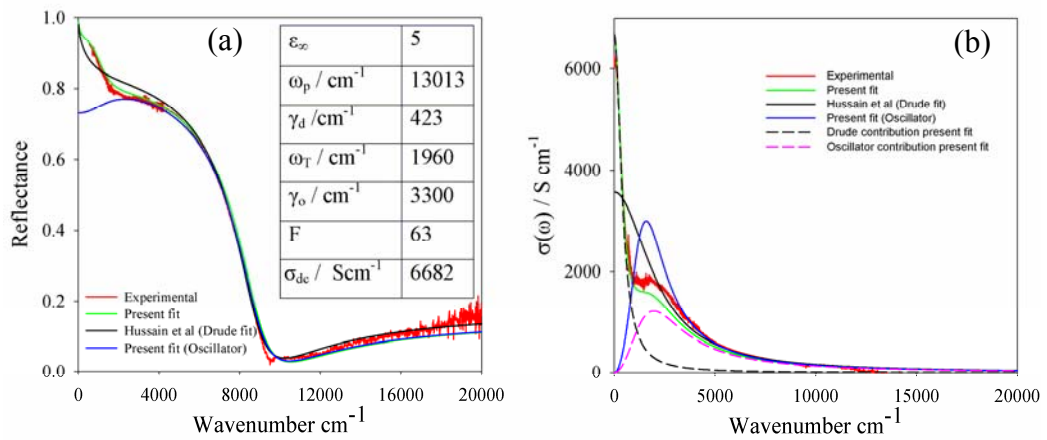


Fig. 54 Reflectivities (a), and the frequency dependence of the conductivities (b) of $\text{Cs}_{0.2}\text{WO}_3$ crystal for $E \perp c$ direction. The symbols are same as described for Fig. 47.

Thus in all samples, $\sigma(\omega)$ exhibits two well-defined components in the infrared: a Drude term which is dominating in low frequency range and a broad band in the high frequency range.

In turn, the strong Drude term accounts for the good dc conductivity of these compounds. Therefore the present data show a coexistence of free and bound charges in the K- and Cs-HTB at $x = 0.20, 0.25$, a doping value which provides experimentally metallic dc conductivity.

4.7 Micro-reflectivity of metallic Li_xWO_3 single crystals ($x = 0.45 - 0.35$) and Kramers-Kronig analysis

The reflectivity spectra of metallic Li_xWO_3 series were reinvestigated as shown in Fig. 55a for $\text{Li}_{0.45}\text{WO}_3$ crystal.

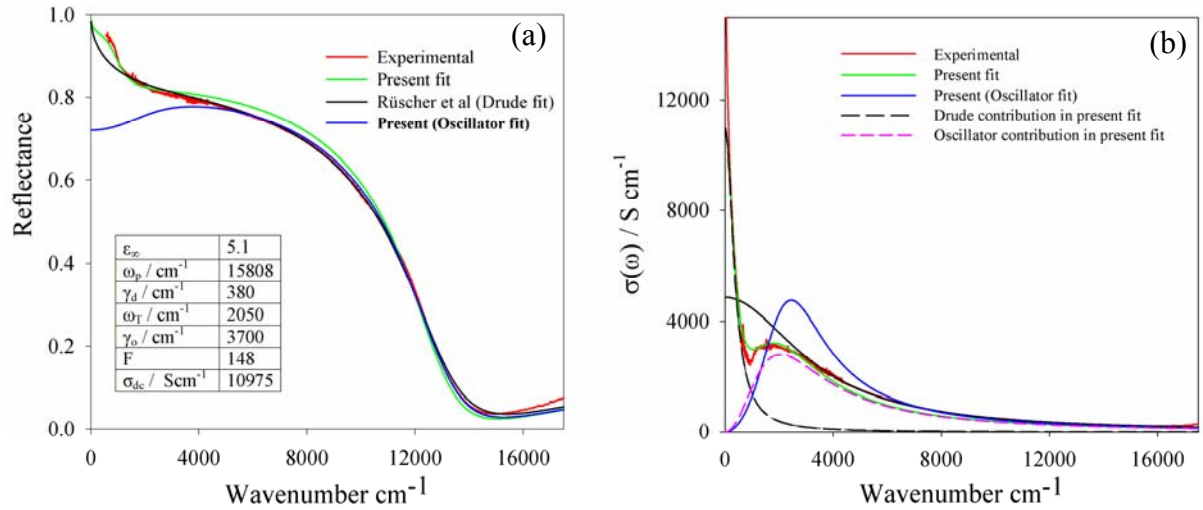


Fig. 55 Reflectivities (a), and the frequency dependence of the conductivities (b) of $\text{Li}_{0.45}\text{WO}_3$ crystal. The symbols are same as described for Fig. 47.

The crystals were taken from earlier study (Rüscher *et al.*, 2008). The spectrum shows a metallic-like behavior with well evident pseudo-plasma edge around 15000 cm^{-1} . Fig. 55a shows also a tentative plot of reflectivity using data as reported by Rüscher *et al.* (2008) using Drude model for free carriers (black curve).

It is seen that for $\omega > 1500 \text{ cm}^{-1}$, the calculated reflectivity fits well with Drude free carriers description but for $\omega < 1500 \text{ cm}^{-1}$, significant deviation occur. The reflectivity curve can, however, be fitted reasonably well by considering a combination of a Drude plasma edge in the low frequency region and an over damped oscillator with eigen frequency in the mid-infrared region. The frequency dependence of the conductivity $\sigma(\omega)$ (red curve), extracted from the

experimental $R(\omega)$ by usual Kramers-Kronig transformations is shown in Fig. 55b along with the calculated curves including the contribution of optical conductivity of Drude part (dashed black curve) and oscillator part (dashed pink curve) from the present Drude-Lorentz oscillator fit. The fit parameters values are given in Fig. 55a. There is a clear change of slope in $R(\omega)$ around 1500 cm^{-1} , indicative of two different contributions to $\sigma(\omega)$.

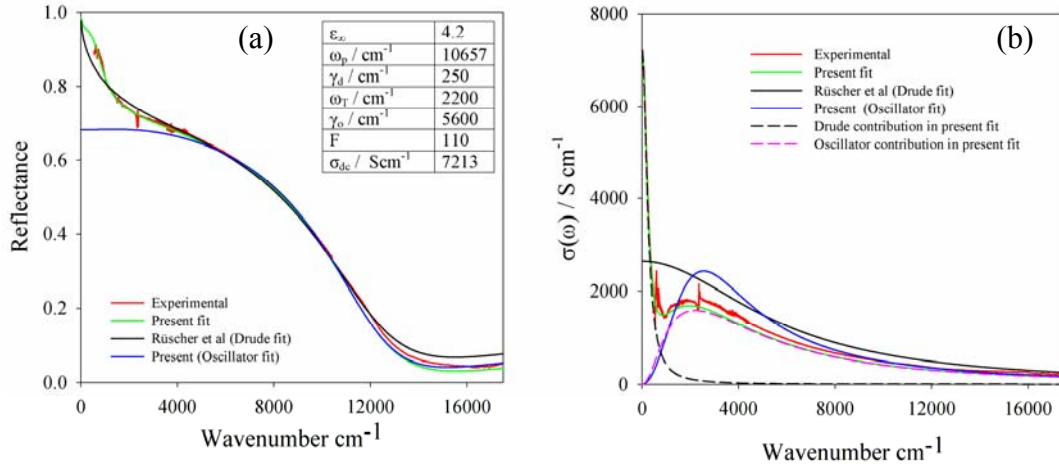


Fig. 56 Reflectivities (a), and the frequency dependence of the conductivities (b) of $\text{Li}_{0.4}\text{WO}_3$ crystal. The symbols are same as described for Fig. 47

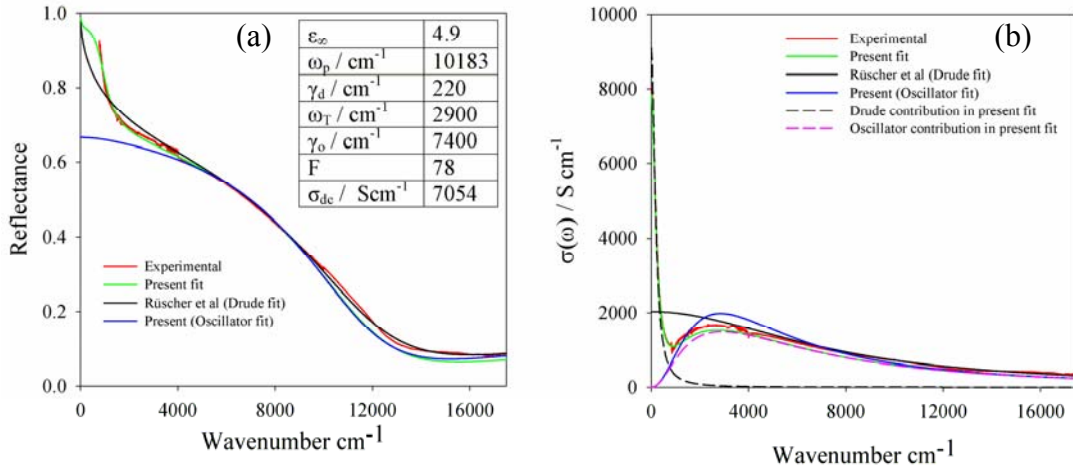


Fig. 57 Reflectivities (a), and the frequency dependence of the conductivities (b) of $\text{Li}_{0.35}\text{WO}_3$ crystal. The symbols are same as described for Fig. 47

The reflectivity spectra of $\text{Li}_{0.4}\text{WO}_3$ and $\text{Li}_{0.35}\text{WO}_3$ (dark part) crystals were reinvestigated using same technique as described for $\text{Li}_{0.45}\text{WO}_3$ crystal. The results are shown in Fig. 56 and Fig. 57. It should be noted that the optical micrograph of $\text{Li}_{0.35}\text{WO}_3$ crystal appears inhomogeneous with thin bright slabs and larger dark areas (Rüscher *et al.*, 2008). In present case the reflectivity spectrum of dark areas are only considered.

4.8 Polarized micro-reflectivity of $\text{Nb}_{18-x}\text{W}_{8+x}\text{O}_{69}$ ($x = 0, 2, \dots, 9$) with block type structure and Kramers-Kronig analysis

It has been shown that compositions $\text{Nb}_{18-x}\text{W}_{8+x}\text{O}_{69}$ with $x = 0, 2, \dots, 9$ form a series where x electrons can be doped per 5×5 block layer (Gatehouse *et al.*, 1964; Roth *et al.*, 1965a). In the present case, the optical properties of the whole series were remeasured particularly in the MIR spectral range using polarized micro-reflectivity technique. Good agreements with the published spectra were obtained above 1000 cm^{-1} . All crystals investigated were needle-shaped (typically $1 \times 0.5 \times 0.5 \text{ mm}^3$). The growth axis of the crystals is always parallel to the y -axis of the crystal lattice and coincides with the direction of infinite extension of the blocks.

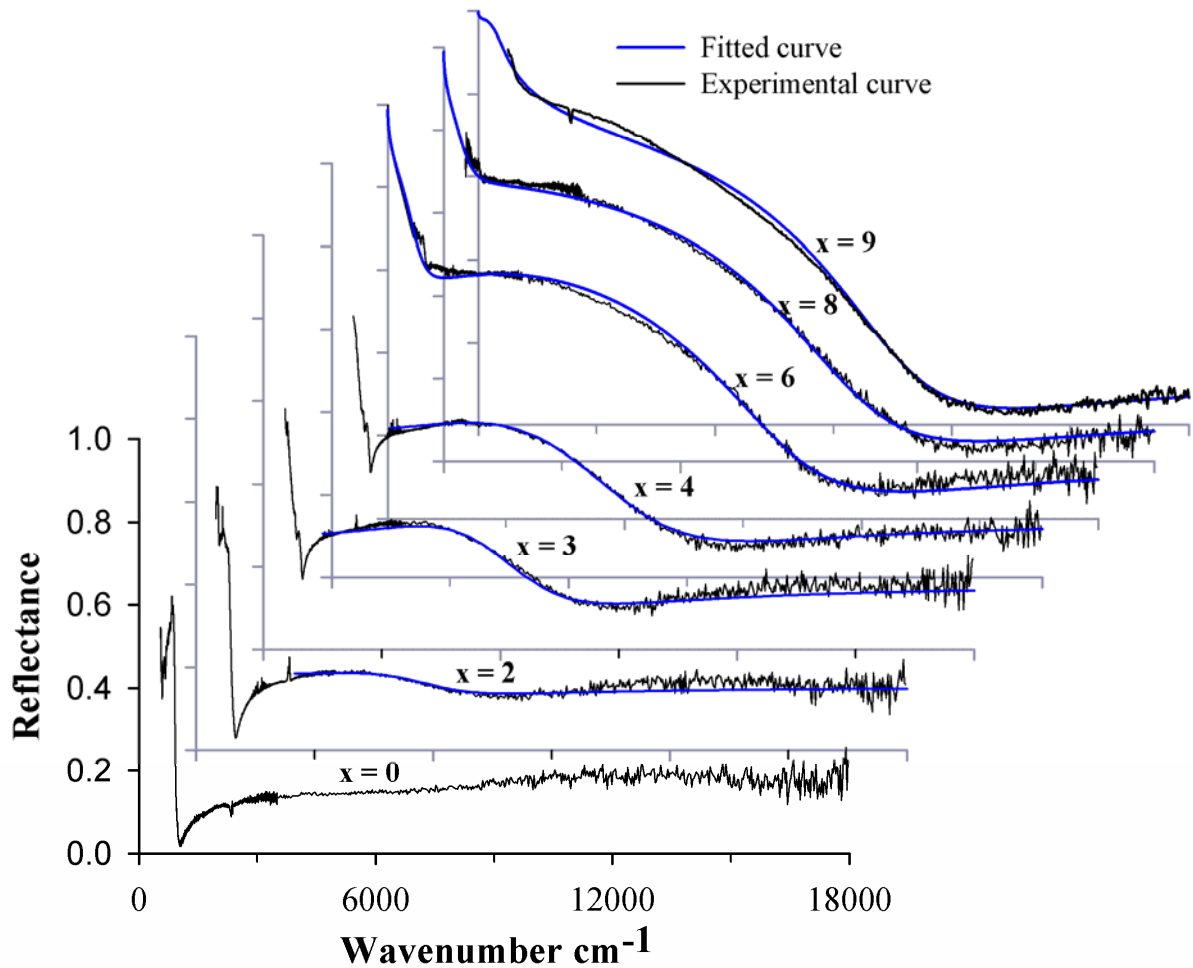


Fig. 58 Polarized micro-reflectivity spectra (black lines) of $\text{Nb}_{18-x}\text{W}_{8+x}\text{O}_{69}$ ($x = 0, 2, \dots, 9$) crystals (as denoted) for $E \parallel c$ direction. The spectra have been fitted (blue lines) using Drude-Lorentz oscillator model for $x = 9, 8$, and 6 samples and Lorentz oscillators for $x = 4, 3$, and 2 samples.

The crystals were glued to the sample holder (glass plate) with such an orientation that one could measure the reflectivity of the plane with the y-axis within and perpendicular to the crystal surfaces. The spectra for the electric field polarized parallel to the y-axis including reported data (Rüscher *et al.*, 1993) and new MIR data are shown in Fig. 58. The undoped sample ($x = 0$) shows typical insulator spectrum with phonons below 900 cm^{-1} . For $x = 2, 3$, and 4 samples, a resonance like feature increases that can typically be described by a Lorentz oscillator with systematic decrease in eigen frequency starting from about 5000 cm^{-1} for the electric field polarized parallel to the y-axis (i.e. $E \parallel c$). For $x = 6, 8$, and 9 samples, metallic-like reflectivities with a well evident pseudo-plasma edge around 13000 cm^{-1} is observed (Fig. 58, as denoted). However a tentative data evaluation implies that reflectivity contains a combination of a Drude plasma edge in the low frequency region and an over damped oscillator with eigen frequency in the mid-infrared region, which is also shown in the figure. This result has been obtained by Kramers-Kronig analysis, followed by further data evaluation. The real part of the optical dielectric functions (ϵ_1) and optical conductivity $\sigma(\omega)$ were extracted from the experimental $R(\omega)$ by usual Kramers-Kronig transformations. The results are shown in Fig. 59 together with the results of Drude-Lorentz oscillator fitting procedure. The contribution of optical conductivity of Drude part and oscillator part from the present fit is also shown in corresponding figures. The fit parameters values for $E \parallel c$ reflectivities are listed in Table 13.

Table 13 High frequency dielectric constant (ϵ_∞), Drude plasma frequency (ω_p), damping constant (γ_d) from Drude part, transversal optical mode (ω_T) of the oscillator, damping constant (γ_o) of the oscillator, and oscillator strength (F) obtained using Drude-Lorentz oscillator model for $x = 9, 8$, and 6 samples and Lorentz oscillator for $x = 4, 3$, and 2 samples for the description of reflectivity for $E \parallel c$ direction of 5×5 block type $\text{Nb}_{18-x}\text{W}_{8+x}\text{O}_{69}$ compounds (x = number of electron doped).

	Parameters	Samples, $\text{Nb}_{18-x}\text{W}_{8+x}\text{O}_{69}$					
		9e	8e	6e	4e	3e	2e
	ϵ_∞	4.5	4.5	5.1	4.9	5.3	5.2
Drude	$\omega_p / \text{cm}^{-1}$	9546	6364	5940	-	-	-
	$\gamma_d / \text{cm}^{-1}$	150	600	650	-	-	-
Oscillator	$\omega_T / \text{cm}^{-1}$	1700	2450	3300	4700	5150	5750
	$\gamma_o / \text{cm}^{-1}$	5100	5100	5300	5200	4200	4000
	F	160	82	46	10.7	5.0	1.0

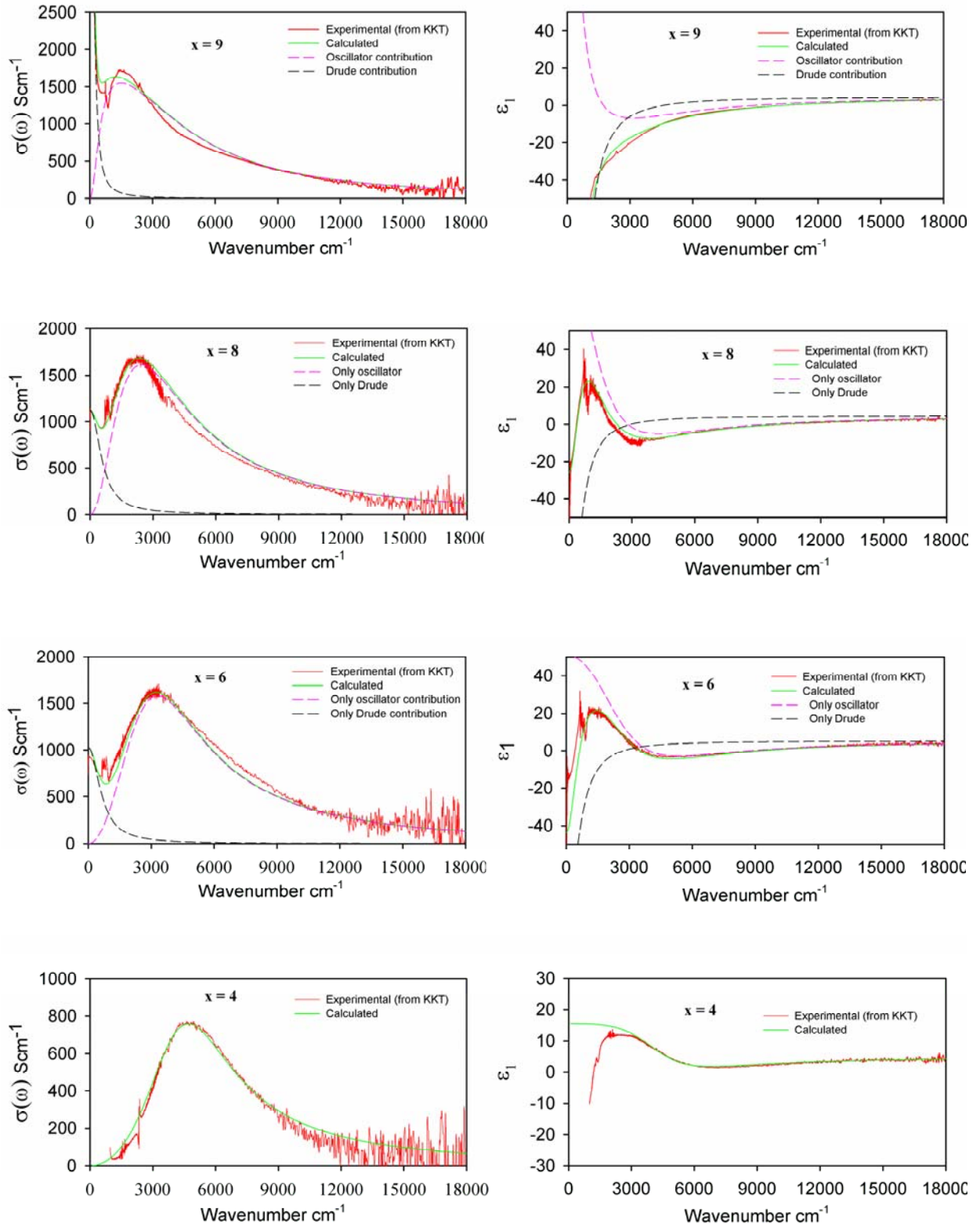


Fig. 59 (a) The frequency dependence of the conductivities ($\sigma(\omega)$), and (b) real part of dielectric function (ϵ_1), of $\text{Nb}_{18-x}\text{W}_{8+x}\text{O}_{69}$ ($x = 9, 8, 6, \text{ and } 4$) crystals (as denoted) for $E \parallel c$ direction: obtained after KKT of extrapolated experimental reflectivity (red curve), Drude-Lorentz oscillator fit (green curve), contribution of oscillator part of Drude-Lorentz oscillator fit (dashed black curve), and Drude part of Drude-Lorentz oscillator fit (dashed pink curve).

Similar to 5000 cm^{-1} feature in the E||c spectra, but less intense, a feature centered at about 12000 cm^{-1} evolves with increasing doping in the E⊥c spectra (Fig. 60). The spectra have been fitted considering one oscillator with eigen frequency at about 11000 cm^{-1} and three phonon lines below 900 cm^{-1} . The E⊥c reflectivities are also shown in Fig. 61 for spectral range $600 - 2500\text{ cm}^{-1}$ to show the existing phonon peaks (below 900 cm^{-1}) clearly. The fit parameters values for E⊥c reflectivities are listed in Table 14.

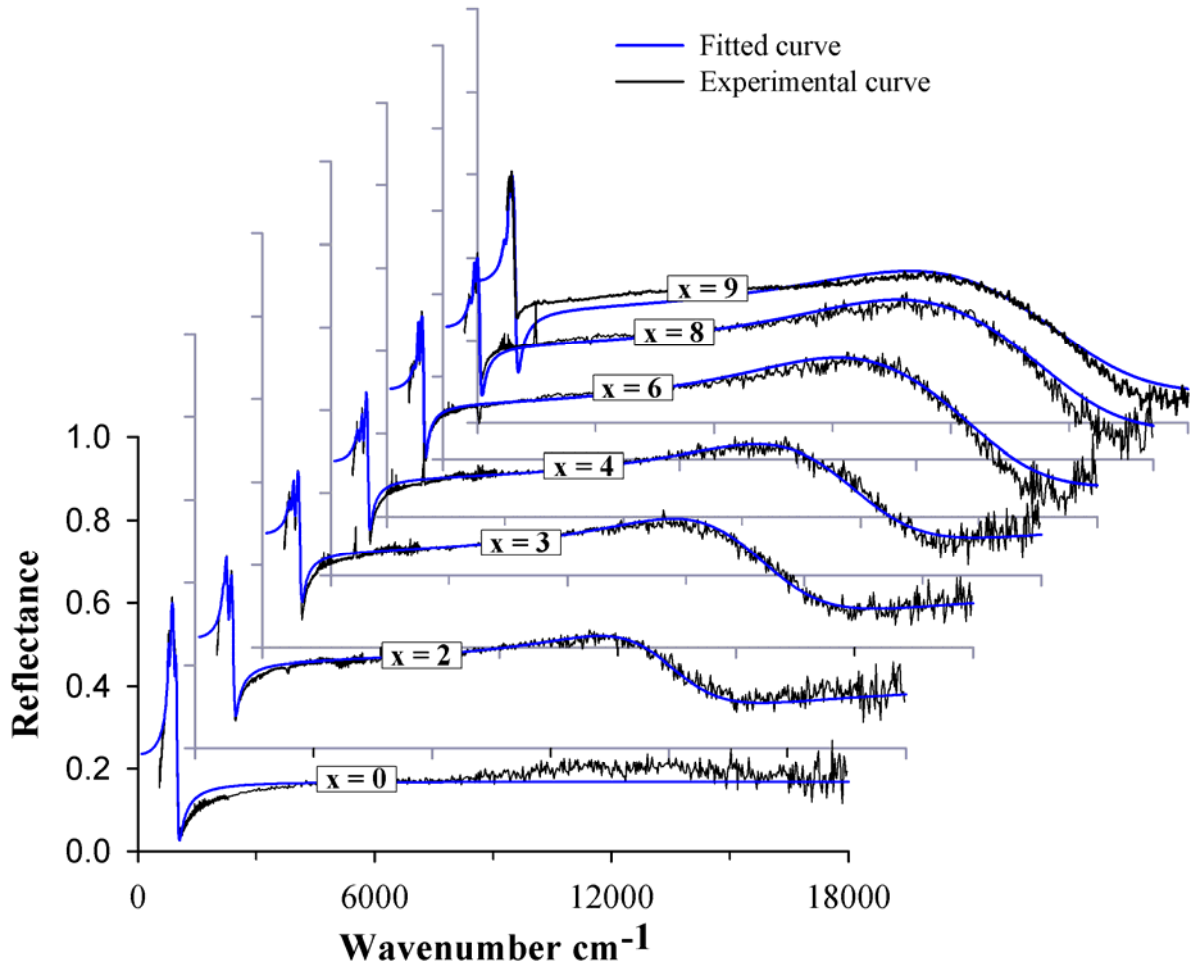


Fig. 60 Polarized reflectivity spectra (black curves) of $\text{Nb}_{18-x}\text{W}_{8+x}\text{O}_{69}$ ($x = 0, 2, \dots, 9$) crystals (as denoted). The spectra are fitted (blue curves) using four Lorentz oscillator functions. The fit parameters values are listed in Table 14.

Table 14 High frequency dielectric constant (ϵ_∞), transversal optical mode (ω_T), damping constant (γ_o), and oscillator strength (F) obtained using Lorentz oscillator model for the description of reflectivity for $E \perp c$ direction of 5×5 block type $Nb_{18-x}W_{8+x}O_{69}$ compounds. The number of “free electrons” expected from the chemical formula $Nb_{18-x}W_{8+x}O_{69}$ with the assumption of Nb^{5+} , W^{6+} , and O^{2-} oxidation states, is given in Table (these numbers are equal to x).

Oscillator	Parameters	Samples, $Nb_{18-x}W_{8+x}O_{69}$						
		0e	2e	3e	4e	6e	8e	9e
First	ϵ_∞	5.7	5.5	5.3	5.3	5.1	5.0	5.0
	$\omega_T / \text{cm}^{-1}$	782	720	698	700	700	700	700
	$\gamma_o / \text{cm}^{-1}$	30	60	70	70	70	70	70
	F	0.6	0.25	0.4	0.4	0.2	0.3	0.5
Second	$\omega_T / \text{cm}^{-1}$	841	785	792	800	805	805	805
	$\gamma_o / \text{cm}^{-1}$	70	70	50	70	25	30	30
	F	1.9	1.4	0.6	0.5	0.42	0.4	0.8
Third	$\omega_T / \text{cm}^{-1}$	940	902	895	895	883	872	855
	$\gamma_o / \text{cm}^{-1}$	40	80	80	70	70	90	95
	F	0.10	0.9	1.15	1.1	1.45	1.9	3.0
Fourth	$\omega_T / \text{cm}^{-1}$	-	11042	10942	11342	11442	11542	11242
	$\gamma_o / \text{cm}^{-1}$	-	3678	4278	4578	5178	5578	6078
	F	-	1.8	2.9	3.1	5.0	5.4	5.5

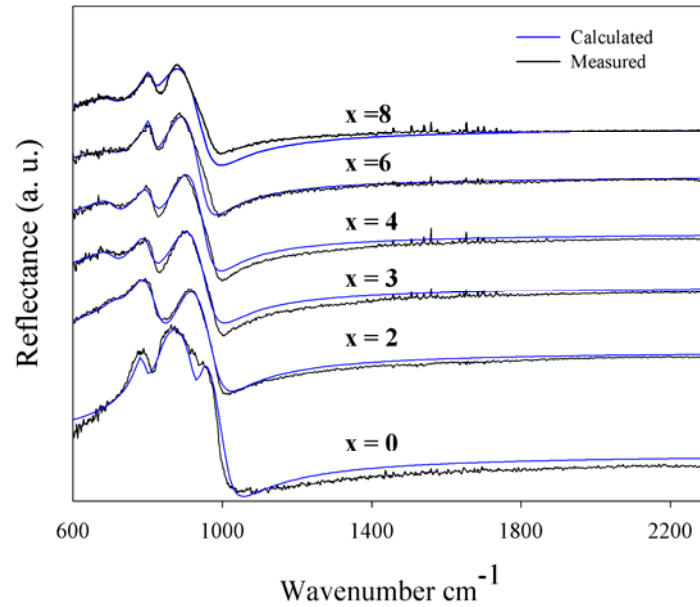


Fig. 61 Polarized reflectivity spectra (black curves) of $Nb_{18-x}W_{8+x}O_{69}$ ($x = 0, 2, \dots, 8$) crystals (as denoted) for $E \perp c$ direction in the MIR spectral range. The spectra are fitted (blue curves) using Lorentz oscillator functions.

5. DISCUSSION

5.1 Structural details concerning Na_xWO_3 and Li_xWO_3 systems

The new data concerning composition, and structure within the systems $\text{Na}_{0.8}\text{Nb}_y\text{W}_{1-y}\text{O}_3$, $\text{Na}_{0.6}\text{Nb}_y\text{W}_{1-y}\text{O}_3$, $(\text{Na}_x\text{Li}_{1-x})_{0.45}\text{WO}_3$, and $\text{K}_{0.55}\text{Nb}_y\text{W}_{1-y}\text{O}_3$ has been evaluated in details in the preceding chapters. Part of the results of $\text{Na}_{0.8}\text{Nb}_y\text{W}_{1-y}\text{O}_3$ and $\text{K}_{0.55}\text{Nb}_y\text{W}_{1-y}\text{O}_3$ systems have already been published (Debnath *et al.*, 2008a and 2008b). Concerning the basic system Na_xWO_3 , there are structural data, which will be discussed in the following.

The present investigation of XRD data for the Na_xWO_3 systems (Table 1, page 19) show pure PTB_0 phase for nominal composition $x = 0.05$, pure PTB_t phase for $x = 0.10$, a mixture of three phases ($\text{PTB}_t + \text{TTB} + \text{PTB}_c$) for $0.15 \leq x \leq 0.25$, a mixture of two phases ($\text{TTB} + \text{PTB}_c$) for $0.30 \leq x \leq 0.4$, and PTB_c pure phase for $x > 0.4$. A set of phase relations for the sodium tungsten bronzes, Na_xWO_3 , was given by Ribnick *et al.* (1963). The present investigation of polycrystalline Na_xWO_3 samples confirms the data of Ribnick *et al.* (1963) for $x > 0.4$ samples. Additional new observations and Rietveld refinements of XRD data improve the range for $x \leq 0.4$. Ribnick *et al.* (1963) observed for samples in the range of $0.39 < x < 0.43$ a mixture of two phases ($\text{PTB}_c + \text{TTB}$); for $0.28 < x < 0.39$ pure TTB phase; for $0.11 < x < 0.28$, a mixture of two phases ($\text{TTB} + \text{PTB}_t$); and for $0.07 < x < 0.11$, pure PTB_t phase. The contribution of each phase could not be obtained in the previous studies. In this work a phase quantification has been achieved using Rietveld profile fit of XRD data, which is visualized in Fig. 62.

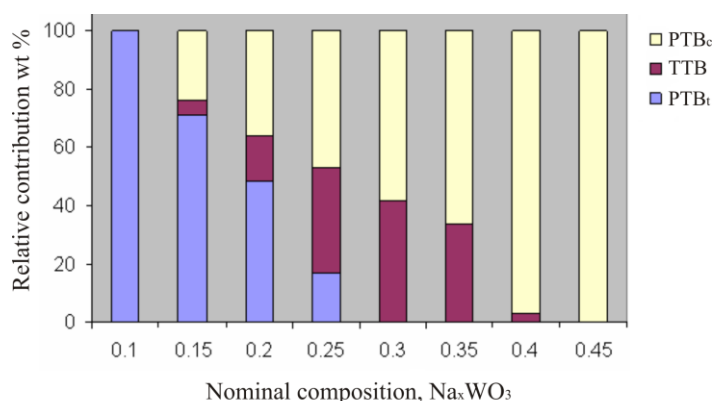


Fig. 62 Relative phase contributions (according to Rietveld refinement) of Na_xWO_3 system prepared by conventional solid state method at 600°C .

García-Ruíz *et al.* (1992) prepared Na_xWO_3 ($0.2 \leq x \leq 0.4$) at 900°C by the same method as used for present investigation and used by Ribnick *et al.* (1963). These authors reported a mixture of two phases for $0.28 \leq x < 0.4$ and a mixture of more than two phases for

$0.20 \leq x < 0.28$ but could not index the third phase. However, in the present investigation it is apparent that the cubic phase start to form from nominal sodium content $x = 0.15$. The systematic decrease in refined lattice parameter of cubic phase with decreasing nominal sodium content (for $x \geq 0.2$) still follow the Brown and Bank relation (1954) (Eq. 18), which shows the formation of PTB_c phase at low sodium content. PTB_c phase at sodium content as low as $x = 0.23$ has been reported (McNeill *et al.*, 1962). The formation of PTB_c phase at sodium content of $x = 0.2$ is also observed for investigation of $(Na_xLi_{1-x})_{0.45}WO_3$ series (Table 5, page 38).

Although the space group Pm-3m was used in most of the earlier works even until presently (Guo *et al.*, 2005), in this work space group Im-3 was used throughout the refinement of PTB_c Na_xWO_3 . Clarke (1977) investigated the temperature dependence of the lattice parameters of single crystal $Na_{0.81}WO_3$ using X-ray diffraction in a back-scattering technique. He found four distinct phases with phase transitions at approximately 293, 343 and 430 K. According to this only above 430 K the structure is that of the ideal perovskite, i.e., the aristotype space group Pm-3m. Below that temperature, the WO_6 octahedra are tilted about pseudocubic $\langle 100 \rangle$ directions and super lattice reflections were observed due to a doubled unit cell in each pseudocubic direction, which leads to space group Im-3. The lattice parameter values given in Table 1 (page 19) for the single phase PTB_c samples are $a_c = a/2$ (Im-3), which directly corresponds to W-W distances. Rüscher *et al.* (2008) investigated the Li_xWO_3 series systematically, and refined the PTB_c phases using Im-3 space group following Wiseman and Dickens (1976). In the present investigation the space group Im-3 is found as the authentic space group for PTB_c Na_xWO_3 system at room temperature.

Rietveld refinement of TTB phase used successfully P4/mbm space group as introduced by Magnéli (1949). However, it is shown (Fig. 9, page 21) that the Rietveld refinement of PTB_t phase using space group P4/nmm as given by Magnéli (1949) is insufficient. Instead PTB_t phase is refined using space group P4/ncc. This result thus improves all previous reports about PTB_t phase where the structure was considered using P4/nmm space group. Recently, the possibility of P4/ncc space group was discussed for PTB_t $Li_{0.1}WO_3$ (Rüscher *et al.*, 2008). In the X-ray diffraction patterns of $Na_{0.1}WO_3$ and $Na_{0.15}WO_3$ there is a small hint for the presence of the 211 reflection in space group P4/ncc in the range between 40 and 41 2theta (Fig. 9, page 21), which is inconsistent with P4/nmm space group. Moreover the structure of PTB_t Na_xWO_3 can be explained by considering the distorted cubic aristotype (ReO_3) structure (space group Pm-3m). In space group P4/nmm the W atoms shift alternatively parallel and anti-parallel to the z-axis. The combination of this antiferroelectric pattern of W displacements on the $\{100\}$

planes of the cubic aristotype and tilting of WO_6 octahedra is related to P4/ncc space group. The use of P4/ncc space group is due to the structural modification for WO_3 where the W atoms are off-centered (as in P4/nmm) and the basal oxygens are additionally tilted around c. Furthermore, the tetragonal structure in P4/nmm and P4/ncc are consistent with the group theoretical analysis, as is the continuous nature of the transition between them (Howard *et al.*, 2002).

Fig. 63a shows the x dependent variation of lattice parameters for perovskite Na_xWO_3 system. The refined lattice parameter values of PTB_o (a_o , b_o , c_o), PTB_t (a_t , c_t) and PTB_c (a) phases are recalculated as $a_{oc} = a_o/2$, $b_{oc} = b_o/2$, $c_{oc} = c_o/2$; $a_{tc} = b_{tc} = a_t/\sqrt{2}$, $c_{tc} = c_t/2$, and $a_c = a/2$, respectively. Thus all parameters are related to the case of Pm-3m symmetry. The average values of lattice parameters of PTB_t and PTB_o phases is also calculated as $\langle a_{tc} \rangle = (2/3 a_{tc} + 1/3 c_{tc})$, and $\langle a_{oc} \rangle = 1/3(a_{oc} + b_{oc} + c_{oc})$, respectively.

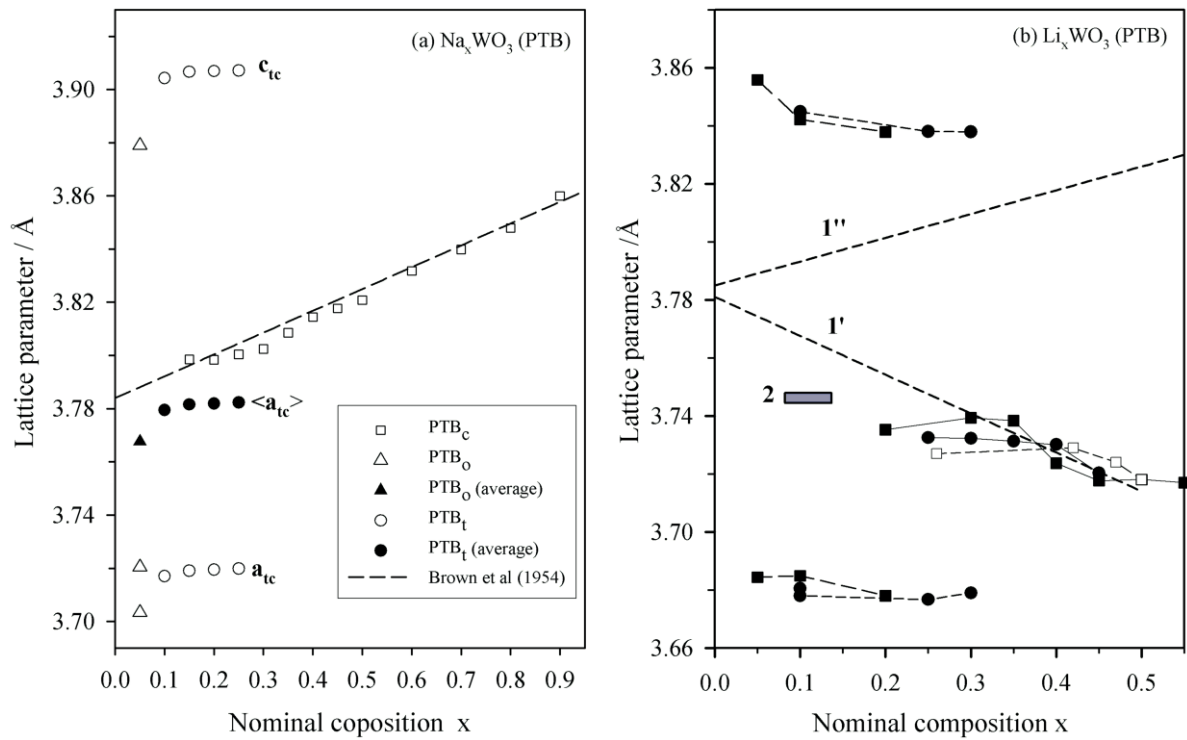


Fig. 63 Lattice parameters of PTB Na_xWO_3 (a) and Li_xWO_3 (b). Figure for Li_xWO_3 system has been taken from Rüscher *et al.* (2008), where \square = Dey *et al.* (2007), \blacksquare = Reau *et al.* (1970), \bullet = Rüscher *et al.* (2008), dashed line 1', 1'' = $x \Rightarrow 0$ extrapolations by Wechter *et al.* (1968) for cubic single phase Li_xWO_3 and Na_xWO_3 compositions, bar (2) = calculated average value $\langle a_{tc} \rangle$ (Rüscher *et al.*, 2008).

With decreasing nominal sodium content the lattice parameter of PTB_c phase decreases until $x = 0.2$. Further decrease in x does not lead to any further decrease in lattice parameter, which indicates that the phase limit has been reached. Similarly, the lattice parameters of PTB_t phase

increases with increasing nominal composition only up to $x = 0.15$, with respect to $x = 0.1$, indicating the phase limit of PTB_t type. A systematic decrease in lattice parameters of PTB_c Na_xWO_3 with decreasing sodium content can be explained by the decrease in W-O bond length in WO_6 octahedra. It has been reported by Wiseman *et al.* (1976) that the WO_6 octahedra are tilted about $3-4^\circ$ for PTB_c Na_xWO_3 without any significant change related on x . Thus Wiseman *et al.* (1976) suggested a change in W-O bond distance for lattice parameter change. Moreover using a theoretical model Walkingshaw *et al.* (2004) showed that the W-O bond length increases, which lead to increase in lattice parameters with systematic incorporation of electron in WO_3 . They, however, consider the undistorted ideal perovskite structure with Pm-3m space group. It is apparent that the actual space group for cubic Na_xWO_3 is Im-3, according to a Glazer (1972 and 1975) type tilting around [001] axis. With further decrease in nominal x a symmetry-breaking transition to an antiferroelectric tetragonal phase (PTB_t) with P4/ncc symmetry is observed. The WO_6 octahedra are tilted and the W atom moves off the center of its WO_6 octahedron in the [001] direction, resulting in alternating W-O bond lengths along c . The P4/ncc symmetry phase become unstable with further decreasing x and an orthorhombic phase is stabilized. This arises from a tilt of WO_6 octahedra towards [110]-type directions lowering the space group to Pcnb.

Although Li_xWO_3 system shows very similar trend of structural changes as described for perovskite Na_xWO_3 system, the much smaller lattice parameters can be explained mainly by tilting of WO_6 octahedra. The lattice parameters of Li_xWO_3 (Rüscher *et al.*, 2008) as related to the shape of a primitive unit cell Pm-3m are plotted as a function of nominal Li content in Fig. 63b together with data given by Reau *et al.* (1970) and Dey *et al.* (2007). The lattice parameter value of the $x = 0.4$ sample is about 1 pm larger compared to the $x = 0.45$ sample. Further decrease in nominal x does not lead to any further increase in a_c and shows that the phase limit has been reached. Wechter *et al.* (1968) proposed an extrapolation from the x dependence of the lattice parameter values from the phase field of cubic compositions Li_xWO_3 with $0.4 < x < 0.5$ and Na_xWO_3 with $0.4 < x < 0.8$ to $x = 0$ according to (in pm) according to Eq. 25 and Eq. 26.

$$a_c(\text{pm}) (Li_xWO_3) = -13.4x + 378.1 \quad \text{Eq. 25}$$

$$a_c(\text{pm}) (Na_xWO_3) = 8.18x + 378.5 \quad \text{Eq. 26}$$

(dashed line 1' and 1'' in Fig. 63b). Eq. 26 is equivalent to the Brown and Banks equation (Eq. 18, page 38). It can be seen that the $x = 0$ intercepts of both lines 1' and 1'' closely agree. Therefore, Wechter *et al.* (1968) suggested a value of about 378.5 pm of a theoretical cubic WO_3 lattice at room temperature. Structure determinations based on powder neutron diffraction

studies on $\text{La}_{0.14}\text{WO}_3$, $\text{Na}_{0.73}\text{WO}_3$, $\text{Na}_{0.54}\text{WO}_3$ and $\text{Li}_{0.36}\text{WO}_3$ samples by Wiseman and Dickens (1976) reveal a tilted perovskite structure with space group Im-3 in all cases apart from $\text{La}_{0.14}\text{WO}_3$ where space group Pm-3m was used. The tilt is given by oxygen shift from a linear W-O-W bonding which results in an angle (φ) as measured by Eq. 27.

$$0.5 \cdot \text{W-W} = l_{\text{W-O}} \cdot \cos(\varphi) \quad \text{Eq. 27}$$

With a W-W distance of $a_c = 373$ pm and a W-O bond length for $\text{Li}_{0.36}\text{WO}_3$ of $l_{\text{W-O}} = 191.7$ pm the tilt angle becomes 13.6° . For $\varphi = 0^\circ$ this bond length leads to a W-W distance of 383.4 pm, which well coincides with the lattice parameter $a_c = 383.4$ pm for the untilted $\text{La}_{0.14}\text{WO}_3$ (Wiseman *et al.*, 1976) with the same W-O bond distance. On the other hand the $x = 0$ intercept of lines 1' and 1'' would imply a tilt angle of about 9° considering a W-O bond length of 191.7 pm. The new data (Rüscher *et al.*, 2008) for the lattice parameter values of single phase PTB_c compositions indicate a more steeper increase for decreasing x values compared to line 1' and that the $x = 0$ intercept could reach the $\varphi = 0^\circ$ value.

The refined lattice parameter values of $\text{PTB}_t \text{Li}_x\text{WO}_3$ (Rüscher *et al.*, 2008) were also recalculated as $a_{tc} = b_{tc} = a_t/\sqrt{2}$, $c_{tc} = a_c$ for better comparison with the lattice parameters of PTB_c as shown in Fig. 63b. The bar denoted by number 2 in Fig. 63b corresponds to the average value $(2/3a_{tc} + 1/3c_{tc}) = \langle a_{tc} \rangle$, which closely agrees to the value a_c of coexisting PTB_c . This shows that the unit volume follows the same trend for the x dependent transition between PTB_c and PTB_t and that the expansion along c is compensated by a contraction perpendicular to c .

Recently many theoretical studies have been done on the structural change of Na_xWO_3 and Li_xWO_3 (Ingham *et al.*, 2005; Walkingshaw *et al.*, 2004 and references therein). Authors explained separately the structural change of Na_xWO_3 and Li_xWO_3 but they did not compare these two systems together. Walkingshaw *et al.* (2004) discussed the structural change of WO_3 upon doping of electron and concluded that the effect of Na^+ ions on the structural change is small. But they did not even consider the formation of TTB phase in Na_xWO_3 system as well as they did not discuss the reason why the Li_xWO_3 system show opposite behavior in the change in lattice parameters that of the Na_xWO_3 . If the electron doping would only be the driving factor in changing crystal structure as well as other physical properties of tungsten bronze family then one would expect same type of structural change in all tungsten bronzes, which is not obvious.

The results from IR absorption spectra of Na_xWO_3 system is very similar to polycrystalline Li_xWO_3 system, investigated by Dey *et al.* (2007). However in Li_xWO_3 system there is no shift

in peak positions to low wavenumber within the PTB_t phase ($0.10 \leq x \leq 0.25$, for Li_xWO₃) although a decrease in lattice parameter with increasing in nominal composition is observed. This may be due to small size of Li ion. On the other hand, in Na_xWO₃ ($x = 0.1 - 0.2$) system a small change in peak position (see Fig. 15, page 27 and Table 4, page 28) of IR absorption spectra is related to the increase in lattice parameters in PTB_t phase. The present IR absorption spectra of Na_xWO₃ do not support the study of Krašovec *et al.* (2001) where a phonon peak at about 800 cm⁻¹ for Na_{0.72}WO₃, Li_{0.31}WO₃, and Li_{0.58}WO₃ samples has been reported. A reasonable explanation for their spectra could be that samples were somehow partially oxidized leading to the formation of tungstate. Metallic oxides e.g., ReO₃ (Feinleib *et al.*, 1968), K_xWO₃ (Hussain *et al.*, 2002) do not show any phonon peak in the infrared spectral range. For an independent check, the absorption spectrum of metallic ReO₃ was measured by using same technique showing no phonon peaks, too.

Salje *et al.* (1980) reported the temperature dependent change in the Raman spectra of WO₃ to be caused by a phase transition from monoclinic to orthorhombic and tetragonal symmetry. Their results indicate that the location of the peak at 809 cm⁻¹ was hardly changed by the phase transition, while the peak at 720 cm⁻¹ split into more than two peaks whose position shifted to lower wavenumbers. The present results for nominal Na_{0.05}WO₃ (PTB_o) also show that the 720 cm⁻¹ mode shifts to lower wavenumber (at 650 cm⁻¹) and broadening of the peak may also indicate more than one peaks. The disappearance of 720 cm⁻¹ mode and little shifting of 809 cm⁻¹ mode to low wavenumber (805 cm⁻¹) for nominal Na_{0.1}WO₃ may indicate a phase transition to PTB_t phase from PTB_o phase. It may note that from the XRD patterns and IR absorption spectra it is obvious that nominal Na_{0.05}WO₃ and Na_{0.1}WO₃ compositions belong to PTB_o and PTB_t phase, respectively. Consequently, these data indicate that the 720 cm⁻¹ mode is highly sensitive to changes in crystal symmetry as well as lattice distortion. The shifting of 809 cm⁻¹ mode was also reported by Egdell *et al.* (1989) but they did observe a second peak at low wavenumber to 809 cm⁻¹ mode for Na_{0.1}WO₃. For crystalline thin film Li_xWO₃ system, it has been reported that the number of Raman peaks decreases with increasing Li/W (= x) ratio, indicating a high symmetry of the structure with higher x values (Lee *et al.*, 2003). In the present system, polycrystalline Na_xWO₃, it was found that the number of peaks also decreases from monoclinic (WO₃) to PTB_t (Na_{0.1}WO₃) phase. For PTB_c, Na_xWO₃ phase no phonon peak was observed. Due to the high reflectivity and low penetration depth of the visible light, most of the Raman measurements yield very small cross sections.

5.2 Discussion of the optical properties of alkali metal tungsten bronzes

A main focus of the present study concerns the chemical composition, structure and optical property relationship of tungsten bronzes and niobium doped tungsten bronzes systems. An important result concerns powder related reflectivity data, which shows very good agreement with the single crystal data for PTB_c Na_xWO₃ systems (Fig. 18, page 30). Following this it has also been shown that powder related reflectivity data could be used as an estimate for the counter doping effect in the TTB system of K_xNb_yW_{1-y}O₃ (Fig. 41, page 55). However, the evaluation of single crystal reflectivity for metallic HTB systems implies a separation in oscillator with the wavenumber above 2000 cm⁻¹ and a Drude free carrier contribution appropriate below instead of a unique free carrier description of the optical properties in these types of systems. Thus, the new separation of the optical properties needs further discussion. A support of the proposed new types of data separation could be achieved taking into account the spectra obtained by other authors: (i) King *et al.* (1972) for Rb_{0.33}WO₃; (ii) Lynch *et al.* (1973) for Na_{0.65}WO₃, Na_{0.735}WO₃, and K_{0.6}WO₃; (iii) Owen *et al.* (1978) for Na_{0.69}WO₃; (iv) Kielwein *et al.* (1995) for Na_{0.68}WO₃.

King *et al.* (1972) measured single crystal reflectivity spectrum of HTB type Rb_{0.33}WO₃ system at 4.2 K. The reflectivity spectrum is shown in Fig. 64a. King *et al.* (1972) explained the spectral feature using Drude free carrier model, also shown in Fig. 64a. It is seen that the minimum feature at about 2000 cm⁻¹ is not included with an ordinary Drude free carrier description. Alternatively, the reflectivity spectrum of Rb_{0.33}WO₃ is fitted using a combination of Drude free carrier and an over damped oscillator model as suggested in this work, which is also shown Fig. 64a along with the fit parameters values for comparison. The frequency dependence of the conductivity ($\sigma(\omega)$) and real part of the dielectric function (ϵ_1) obtained after Kramers-Kronig transformation of measured and calculated reflectivity (R) for Rb_{0.33}WO₃ crystal is shown in Fig. 64b, and c, respectively. It is seen that the reflectivity as well as optical conductivity ($\sigma(\omega)$) can be fitted better by considering a combined model of Drude free carrier and an over damped oscillator. The zero crossing of the real part of the dielectric function (ϵ_1) (pseudo plasma edge) is same in all cases (Fig. 64c). Thus, the data evaluation shows that it is not possible to distinguish from the zero crossing of the real part of the dielectric function between the Drude-oscillator description and Drude free carrier description.

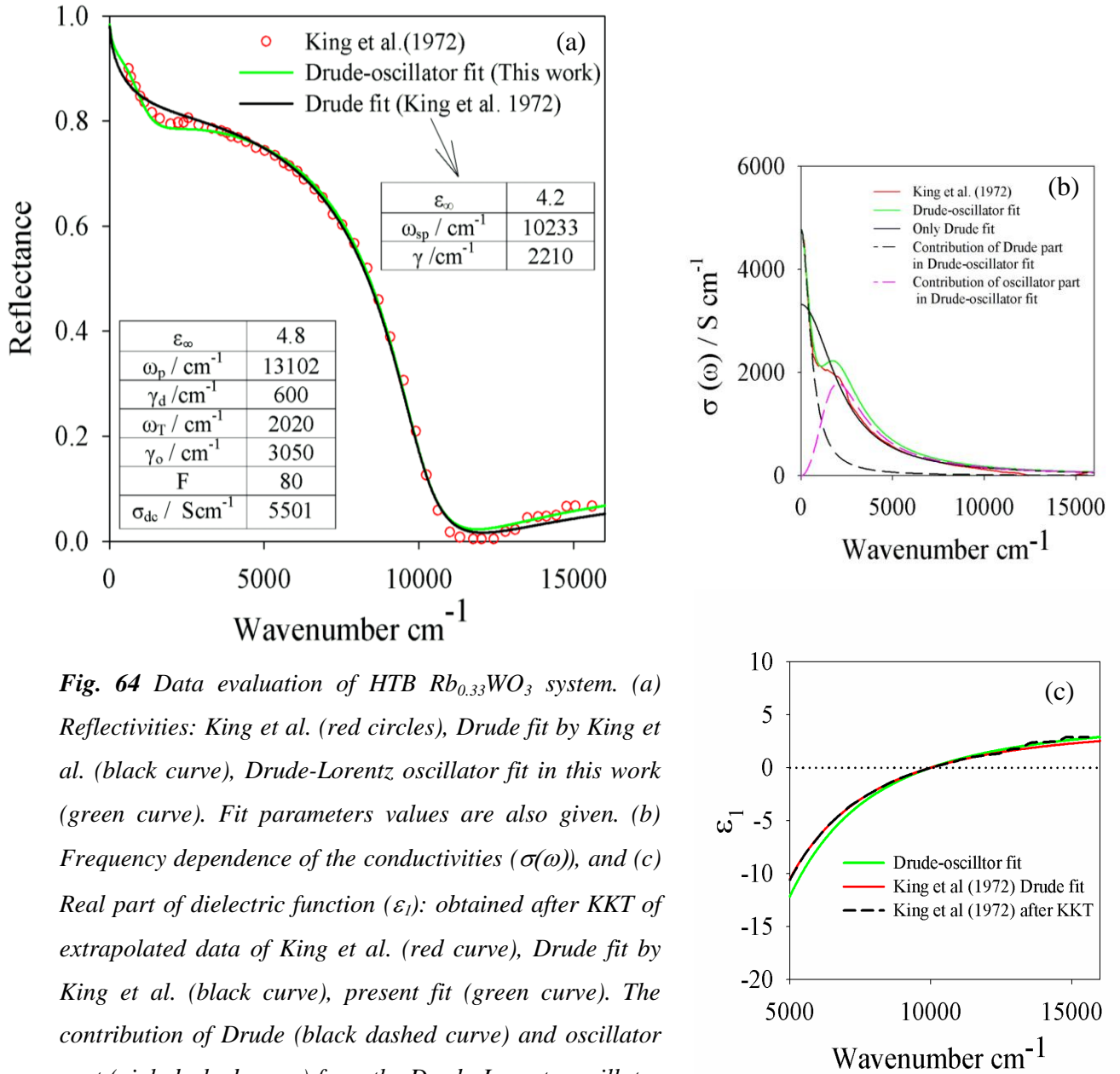


Fig. 64 Data evaluation of HTB $Rb_{0.33}WO_3$ system. (a) Reflectivities: King et al. (red circles), Drude fit by King et al. (black curve), Drude-Lorentz oscillator fit in this work (green curve). Fit parameters values are also given. (b) Frequency dependence of the conductivities ($\sigma(\omega)$), and (c) Real part of dielectric function (ϵ_1): obtained after KKT of extrapolated data of King et al. (red curve), Drude fit by King et al. (black curve), present fit (green curve). The contribution of Drude (black dashed curve) and oscillator part (pink dashed curve) from the Drude-Lorentz oscillator fit are also shown in (b).

Similarly, single crystal reflectivity spectra for $Na_{0.65}WO_3$, $Na_{0.735}WO_3$, and $K_{0.6}WO_3$ measured at 4.2 K by Lynch *et al.* (1973) are fitted using Drude free carrier model and alternatively a combination of Drude free carrier and an over damped oscillator model. The spectra and fit results are shown in Fig. 65, 66, and 67, respectively. It is seen that in all cases the reflectivity as well as optical conductivity can be fitted better by considering a combined model of Drude free carrier and an over damped oscillator. Additionally the real part of $\epsilon(\omega)$ is well fitted as shown for the samples in the corresponding figure. Thus, it is also possible to separate the reflectivity spectra of Lynch *et al.* (1973) into an oscillator contribution and Drude free carrier contribution.

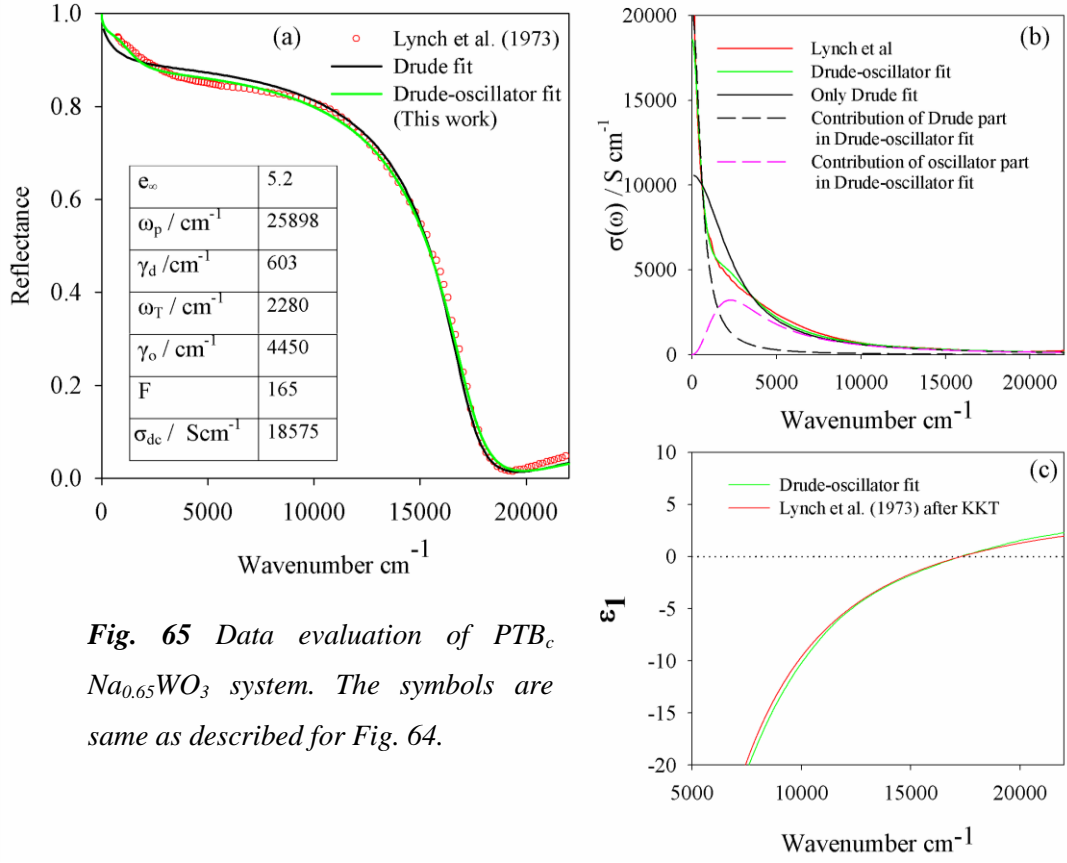


Fig. 65 Data evaluation of PTB_c $Na_{0.65}WO_3$ system. The symbols are same as described for Fig. 64.

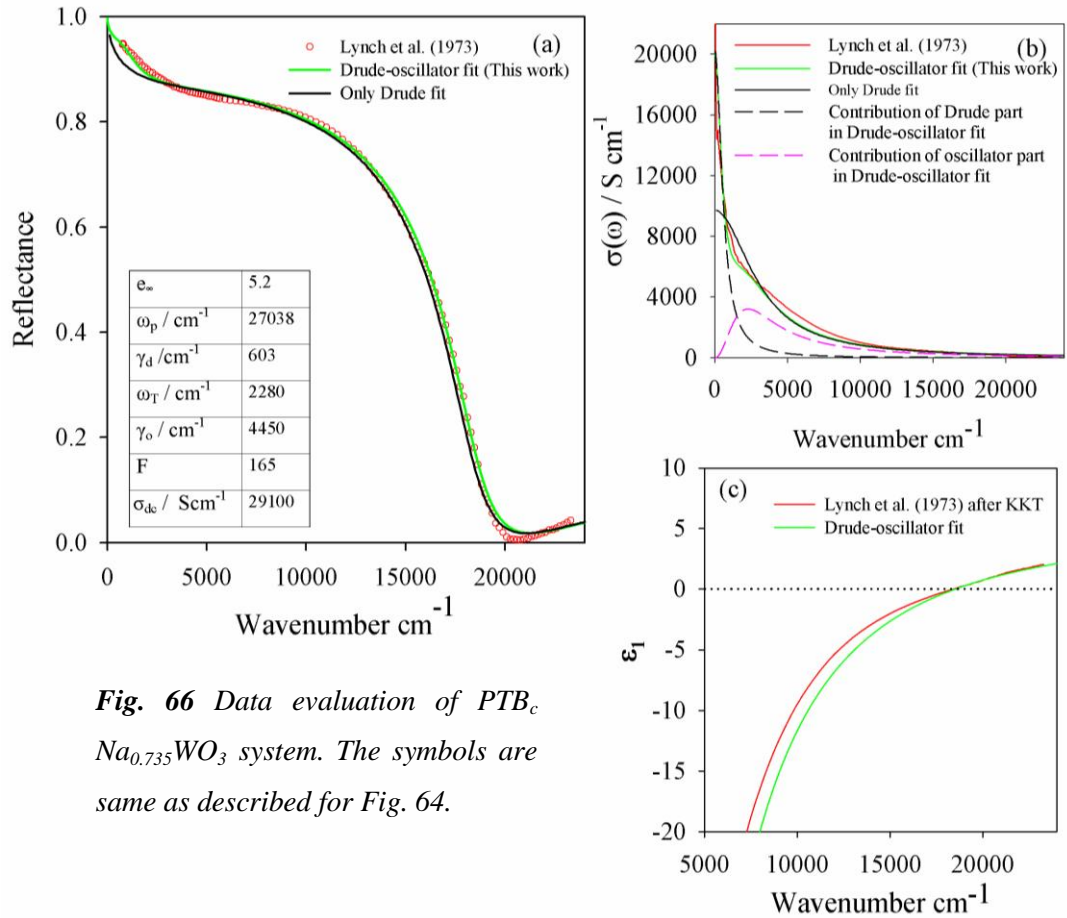


Fig. 66 Data evaluation of PTB_c $Na_{0.735}WO_3$ system. The symbols are same as described for Fig. 64.

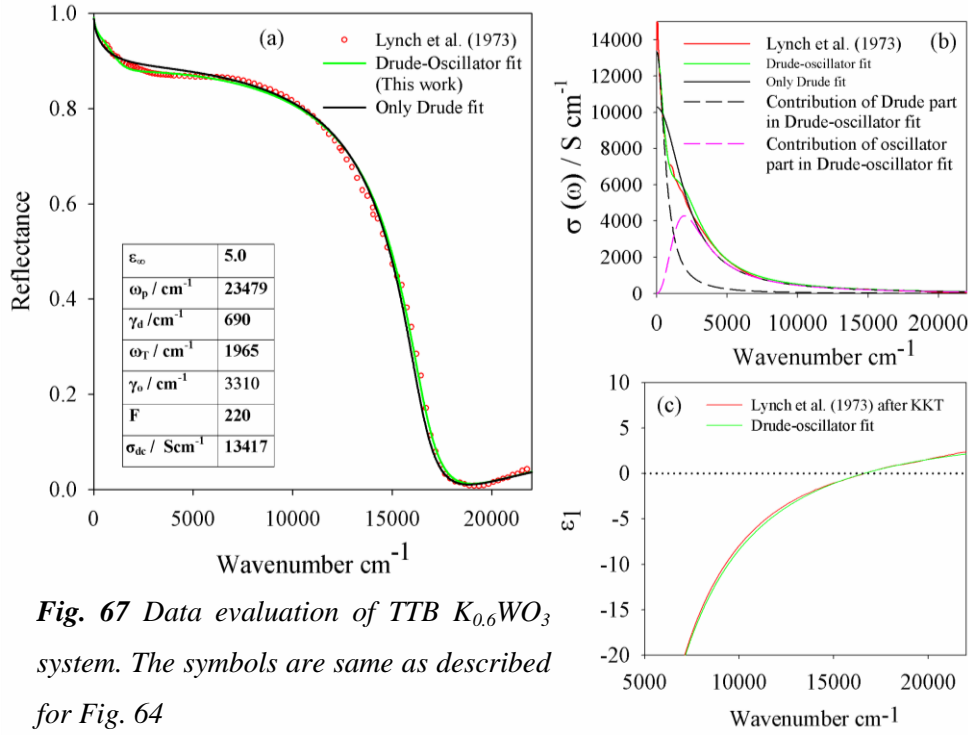


Fig. 67 Data evaluation of TTB $K_{0.6}\text{WO}_3$ system. The symbols are same as described for Fig. 64

It is also important to consider the data and interpretations given by Owen *et al.* (1978) and Kielwein *et al.* (1995) in comparison. Owen *et al.* (1978) measured directly the optical dielectric functions of cubic single crystal Na_xWO_3 ($0.52 \leq x \leq 0.94$) system by a polarization-modulation ellipsometric technique in the energy range from 1.0 to 5.5 eV. Evaluation of these data with the Drude free electron behavior reveal a systematic linear decrease in electron effective mass (m^*) for decreasing sodium content in Na_xWO_3 . This, however, does not support a rigid band model. Therefore, Owen *et al.* (1978) suggested that the optical reflectivity should not simply be described by the Drude free carrier model. Instead a superposition of Drude effect with indirect band transition was considered. Thus Owen *et al.* (1978) used the results of joint-density-of-states calculations in combination with the free-electron model to avoid a relatively large discrepancy between conduction-electron relaxation times derived from the free electron model alone and those determined from the dc conductivity. Kielwein *et al.* (1995) measured the optical constants by high-energy electron-energy-loss spectroscopy (EELS) and also showed that electron effective mass (m^*) increases linearly with increasing Na content in PTB_c Na_xWO_3 . From this finding they proposed a narrowing of conduction band due to admixture of 3s states of Na and 2p states of O.

The data from Owen *et al.* (1978) as well as Kielwein *et al.* (1995) are extrapolated according to Drude equation. The optical reflectivity (R) as well as frequency dependence of the

conductivity ($\sigma(\omega)$) were calculated and shown in Fig. 68 (as denoted) as an example for $\text{Na}_{0.69}\text{WO}_3$ composition.

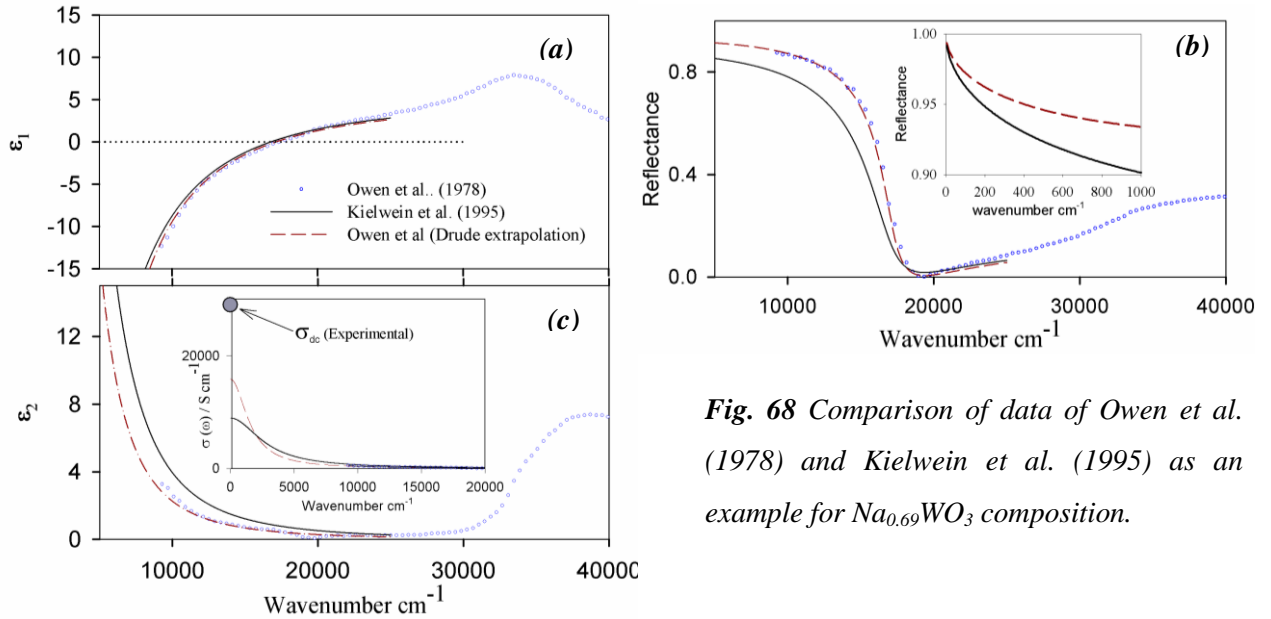


Fig. 68 Comparison of data of Owen *et al.* (1978) and Kielwein *et al.* (1995) as an example for $\text{Na}_{0.69}\text{WO}_3$ composition.

The dashed curve and the solid curve include the derived data from Owen *et al.* (1978) and Kielwein *et al.* (1995), respectively. The absolute values of the calculated parameters vary in these two reports. The dc conductivity derived from the Owen *et al.* (1978) and Kielwein *et al.* (1995) data are shown in inset of Fig. 68c, which indicates the Kielwein *et al.* (1995) conductivity is less than that of the Owen *et al.* (1978). Moreover, Owen *et al.* (1978) noted that the measured dc conductivity (marked with big circle in Fig. 68c) is almost two times larger than that of the calculated. It is seen that the zero-crossing of ϵ_1 is nearly same in both cases although two different techniques have been used.

Thus from the above discussion it can be concluded that the optical properties of metallic M_xWO_3 systems can be separated into two parts: (i) Drude part, and (ii) oscillator part. Accordingly a question arises “What is origin of this oscillator?” A possible answer could be given considering the optical properties of the low symmetric phase possessing a low doping concentration.

The optical property of non-metallic $\text{Na}_{0.037}\text{WO}_3$ (PTB_0) as investigated by polarized micro-reflectivity technique shows the high anisotropy in reflectivity curves (Fig. 22a, page 35). A close approximation of the reflectivity curves could be achieved with calculated reflectivity curves using oscillator functions (Fig. 69). The E 90° spectrum can be described using two

oscillators for the phonon peaks and an over damped one for the absorption effect in the near infrared range. This over damped oscillator can be explained by a polaron absorption considering a strong electron-phonon interaction.

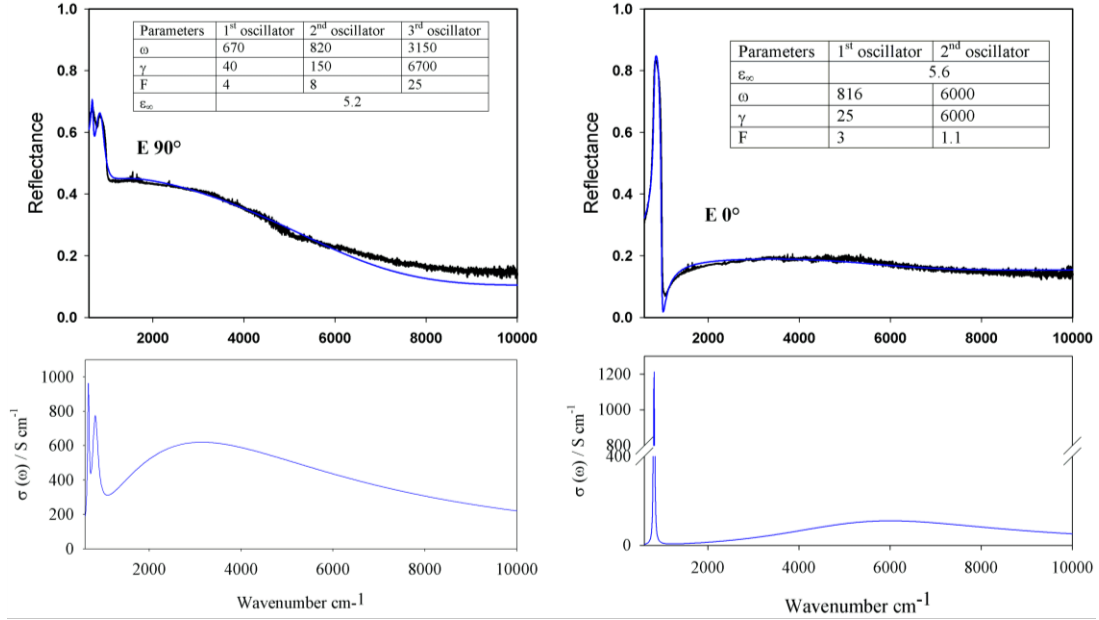
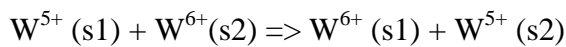


Fig. 69 Measured reflectivity (black curve) of $\text{Na}_{0.05}\text{WO}_3$ crystals (top). $E\ 90^\circ$ and $E\ 0^\circ$ denotes spectra obtained for main components parallel to the electric field vector (E) when rotating the crystal slice. Blue line displays calculated reflectivity. Fit parameter values are included in the figure. The frequency dependence of the conductivity ($\sigma(\omega)$) are also shown (bottom curves).

These data imply that the electron is strongly coupled in one crystallographic direction of $\text{Na}_{0.037}\text{WO}_3$ sample. It has been shown (Rüscher *et al.*, 2008) that polarized reflectivity spectra of $\text{PTB}_t\text{Li}_{0.1}\text{WO}_3$ reveal typical phonon contributions and show strong anisotropic optical properties, too. Thus, it can be argued that structural details of the WO_3 matrix such as W-O-W bond distances and angles, their dynamics and their flexibility play an important role favoring a strongly anisotropic coupling strength. This also holds considering polaron formation as a consequence of sufficient and strong anisotropic electron phonon interaction including the effect of disorder (Böttger *et al.*, 1985; Rüscher *et al.*, 1992; Rüscher *et al.*, 1993; Rüscher *et al.*, 1995). Considering the formation of small polarons the near infrared absorption is dominated by photon assisted hopping of an electron between neighboring W sites s1, s2:



For intermediate sized and larger sized polarons the excitation of internal oscillations could be considered following a Feynman-polaron model with an oscillator effect for the internal oscillation and a Drude term for the polaron drift contribution (Evrard, 1971).

According to this the oscillator function used for the fit of the spectra measured for Li_xWO_3 (PTB_c), K_xWO_3 (HTB), and Cs_xWO_3 (HTB) may indicate polaron formation in these systems.

It has been shown that an ordinary Drude description largely fails in particular in the MIR spectral region. In order to get a better fit of the reflectivity spectra a combination of free carries contribution and oscillator contribution is necessary. This kind of combination of free and bound charges has been described in details by Stern (1963). The background of this big oscillator is the polaron which can be explained by Feynman polaron model. Alternatively the exclusion of Drude free carrier type behaviour can be established more obviously considering Fig. 70, where the plasma frequency as determined by the zero-crossing of ϵ_1 , obtained from the KKT of measured spectra of all the systems are plotted against chemical carrier concentration.

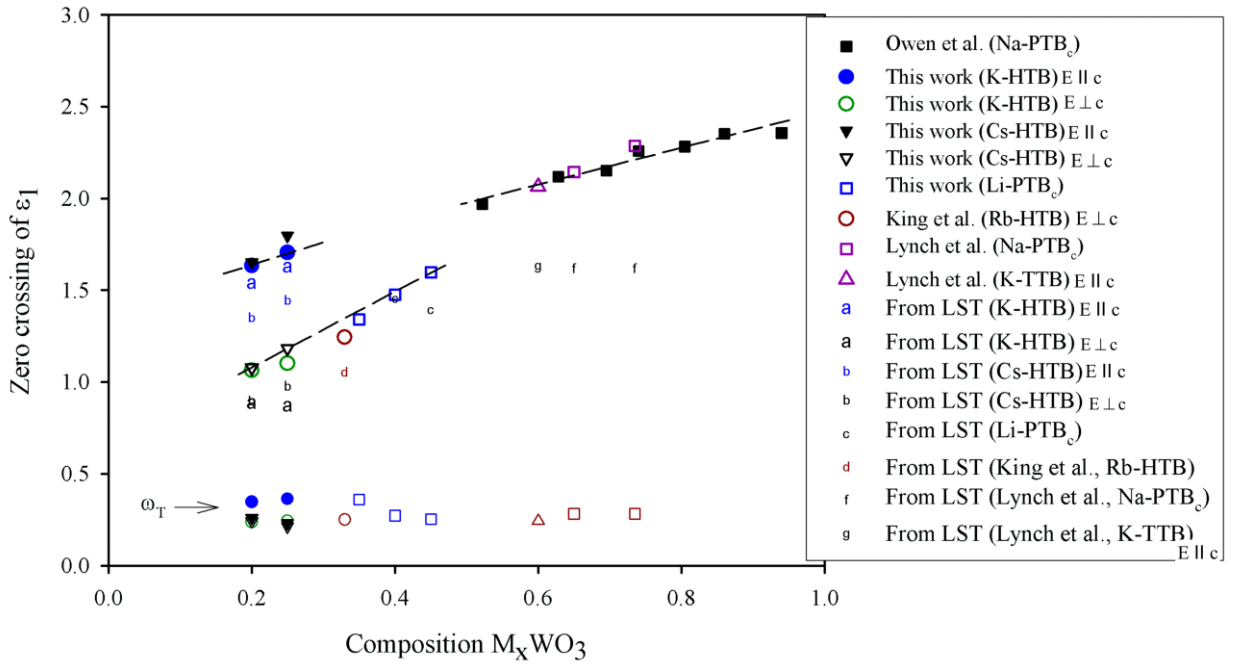


Fig. 70 The zero-crossing of ϵ_1 and transversal optical modes (ω_T) (as denoted) of $M_x\text{WO}_3$ systems. The dashed lines are given only for better comparison. The calculated longitudinal optical modes of the oscillator from the LST relation (Eq. 29) are also included as denoted in the legend.

According to the Drude free carrier concept a square-root behavior is expected for the change in plasma frequency with carrier concentration. However, it is observed that the zero-crossing of ϵ_1 varies linearly with chemical carrier concentration.

The possibility of using only the oscillator to describe the reflectivity of metallic tungsten bronzes can be excluded comparing the values of zero-crossing of ϵ_1 and the longitudinal optical modes (ω_L) calculated from Lyddane-Sachs-Teller relation (LST) (Eq. 29), which is also included in Fig. 70. It is seen that is ω_L smaller compare to zero-crossing ϵ_1 , which let to conclude that the oscillator only is not sufficient to describe the reflectivity feature as well as change in zero-crossing of ϵ_1 with carrier concentration.

It is seen (Fig. 70) that the zero-crossing of ϵ_1 for $E \perp c$ direction of HTB and PTB_c Li_xWO_3 phases lie in the same line, which may be due to nearly same amount of tilting of WO_6 octahedra in both systems. Also the zero-crossing of ϵ_1 for $E \parallel c$ direction for HTB, TTB, and PTB_c Na_xWO_3 phases lie in the same line. This may be due to the same kind of lattice expansion and comparable lattice parameters of PTB_c Na_xWO_3 (≈ 3.80 Å, Table 1) and HTB M_xWO_3 ($c_{HTB/2} \approx 3.76 - 3.78$ Å, Hussain (1978)) phases. On the other hand, the transversal optical modes (ω_T , taken from the Drude-Lorentz oscillator fit results) (Fig. 70) remain nearly constant with respect to the zero-crossing of ϵ_1 for all samples.

Table 15 High frequency dielectric constant (ϵ_∞), transversal optical modes of the oscillator (ω_T), and oscillator strength (F) obtained using the Drude-Lorentz oscillator model for the description of single crystal reflectivity of M_xWO_3 . The zero-crossing of real part of dielectric function (ϵ_1) and calculated oscillator strength (F_{LST}) using Eq. 32 are also included.

Systems	Measured direction	Zero-crossing of ϵ_1	ϵ_∞	ω_T	F	F_{LST}
$K_{0.2}WO_3$ (HTB)	$E \parallel c$	13173	4.8	2797	90	102
$K_{0.2}WO_3$ (HTB)	$E \perp c$	8578	5	1900	66	97
$K_{0.25}WO_3$ (HTB)	$E \parallel c$	13750	5	2937	95	105
$K_{0.25}WO_3$ (HTB)	$E \perp c$	8890	5.1	1972	60	99
$Cs_{0.2}WO_3$ (HTB)	$E \parallel c$	13331	5	2097	130	197
$Cs_{0.2}WO_3$ (HTB)	$E \perp c$	8688	5	1960	63	93
$Cs_{0.25}WO_3$ (HTB)	$E \parallel c$	14485	5	1865	190	297
$Cs_{0.25}WO_3$ (HTB)	$E \perp c$	9541	5	1717	100	149
$Rb_{0.33}WO_3$ (HTB) (King <i>et al.</i>)	$E \perp c$	10027	4.8	2020	80	113
$K_{0.6}WO_3$ (TTB) (Lynch <i>et al.</i>)	$E \parallel c$	16644	5	1965	220	353
$Na_{0.65}WO_3$ (PTB_c) (Lynch <i>et al.</i>)	-	17285	5.2	2280	165	294
$Na_{0.735}WO_3$ (PTB_c) (Lynch <i>et al.</i>)	-	18433	5.2	2280	165	335
$Li_{0.4}WO_3$ (PTB_c)	-	11895	4	2200	110	113
$Li_{0.45}WO_3$ (PTB_c)	-	12877	5.1	2050	148	196

The fit parameter values for oscillator contribution of Drude-Lorentz oscillator fit for all samples (presently investigated) are listed in Table 15. It is seen that the oscillator strength (F) for $E \parallel c$ direction is always higher than that of the $E \perp c$ direction. Structurally this may be related to the alkali metal ions vacancies in parallel to c-axis are more prominent to distort than that of the other direction.

The variation of oscillator strength can be explained considering the model given by Fröhlich (1966) as follows.

The relation between the longitudinal frequency (ω_L), transverse frequency (ω_T), and macroscopic plasma frequency (ω_P) of an oscillator can be explained by Eq. 28, which express that in longitudinal waves the restoring forces are larger than in transverse ones because of the long range Coulomb forces set up by longitudinal waves.

$$\omega_L^2 = \omega_T^2 + \omega_P^2 \quad \text{Eq. 28}$$

If ϵ_s is the static, and ϵ_∞ the high frequency dielectric constant of the oscillator then according to Lyddane-Sachs-Teller relation (LST) (1941)

$$\omega_L^2 / \omega_T^2 = \epsilon_s / \epsilon_\infty \quad \text{Eq. 29}$$

It can be written that

$$(\epsilon_s - \epsilon_\infty) / \epsilon_\infty = (\omega_L^2 - \omega_T^2) / \omega_T^2 \quad \text{Eq. 30}$$

$$\Rightarrow F_{\text{LST}} / \epsilon_\infty = (\omega_L^2 - \omega_T^2) / \omega_T^2 \quad \text{Eq. 31}$$

(F_{LST} = Oscillator strength from LST relation)

$$\Rightarrow F_{\text{LST}} = ((\omega_L^2 - \omega_T^2) / \omega_T^2) \times \epsilon_\infty \quad \text{Eq. 32}$$

Using Eq. 32, the oscillator strength (F_{LST}) has been calculated and added in Table 15. It is seen that F_{LST} from Eq. 32 are larger compare to the oscillator strength (F) obtained from Drude-Lorentz oscillator fit. Therefore the oscillator alone can not explain the zero-crossing of ϵ_1 . The contribution from Drude free carrier part is necessary. Moreover, zero-crossing of ϵ_1 of an oscillator largely decreases with increasing damping, which would result into lower F_{LST} , contrary to the observation. Thus the shift of the reflectivity minima with changing doping concentration does not depend only on oscillator or Drude free carrier part. It is a combined effect of both of them. Such a combination has been considered by Stern (1963), where it has been mathematically shown that dielectric function will have two zero when damping is zero.

In the present systems oscillator plasma edge is more pronounced because of high oscillator strength. The Drude plasma edge becomes less pronounced due to the high damping and high oscillator strength of the oscillator.

5.3 Discussion of the optical properties of Nb-W oxides with block type structure

It is known that the electrical conductivities of Nb-W oxides, $\text{Nb}_{18-x}\text{W}_{9+x}\text{O}_{69}$, change gradually with increasing x from thermally activated ($x = 1$, $E_a = 0.2$ eV) to metallic like ($x = 9$) (Rüscher *et al.*, 1988b) as measured for the electric field parallel to the block axis (Fig. 71). It is interesting to note that metallic like optical properties develop only parallel to the direction of infinite extension (i.e., y-axis) of the block units.

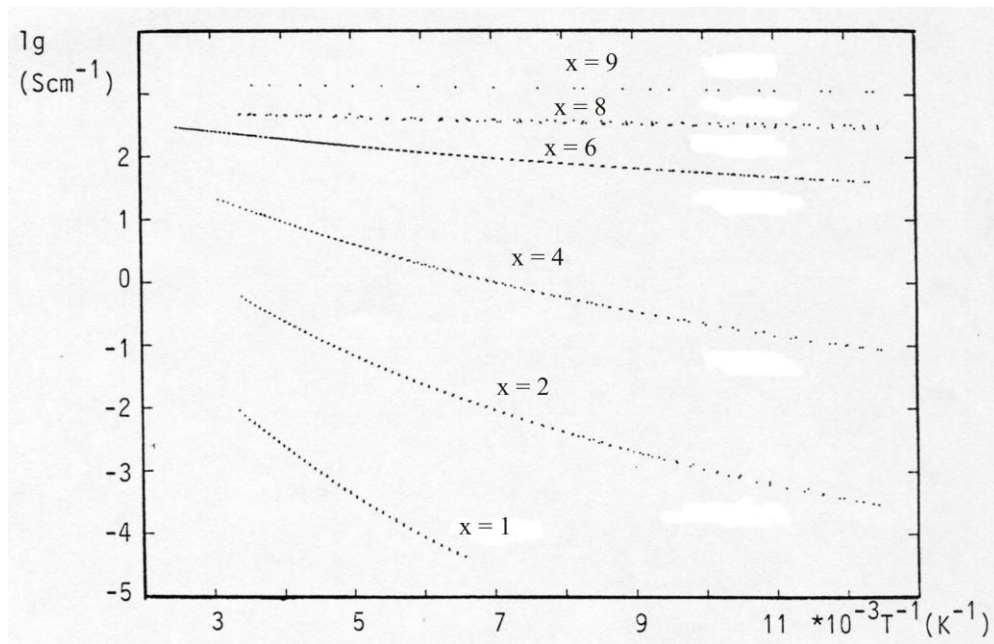


Fig. 71 Arrhenius plot of the electrical conductivity parallel to y axis. This figure is taken from Rüscher *et al.* (1988b).

However, a question is whether the optical properties are dominated by free carriers, by the effect of polarons or by a superimposition of both. It is shown here that the development of the optical plasma edge in Nb-W oxides can not be described considering only Drude equation. This would lead to a much higher dc-conductivity values than that of experimental values. In this work the optical data were remeasured in the infrared range and together with data from near infrared and visible range, were analyzed using Kramers-Kronig transformation (KKT) and Drude-Lorentz oscillator fit procedures. The new data show that most of the spectra can be

fitted systematically with oscillator functions. Only for $x = 6, 8, 9$ samples an additional Drude function has to be added for the $E \parallel y$ component.

The transversal optical mode of the oscillator for $E \parallel y$ and $E \perp y$ direction are plotted against the number of doped electrons per formula unit (Fig. 72).

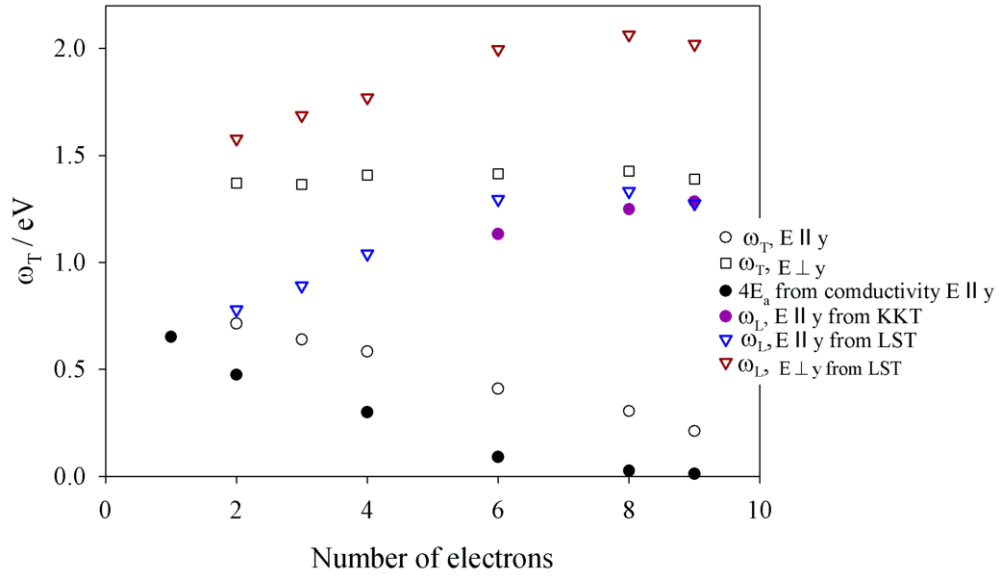


Fig. 72 Variation of transversal optical modes (ω_T , from fitting procedure), longitudinal optical modes (ω_L , both from KKT and LST) with increasing doping concentration of $Nb_{18-x}W_{9+x}O_{69}$ system. The four times of activation energy (E_a) values obtained from Arrhenius plot of conductivity for $E \parallel y$ direction are also compared. The number of “free electrons” expected from the chemical formula $Nb_{18-x}W_{8+x}O_{69}$ with the assumption of Nb^{5+} , W^{6+} , and O^{2-} oxidation states (these numbers are equal to x).

It is seen that the values of transversal optical modes (ω_T) do not change significantly for $E \perp y$ direction, whereas for $E \parallel y$ direction it decreases systematically with increasing doping concentration. It is important to note that ω_T does not reach to zero even for $x \geq 8$ samples, where non-metal to metal transition occurs (see Fig. 71). This supports the oscillator description also for the metallic samples together with the development of the screened free carrier plasma edge in the far infrared region. The activation energy (E_a) for $E \parallel y$ direction is calculated from the Arrhenius plot of the experimental electrical conductivity (Fig. 71) using a linear approximation at 293 K. Within the small polaron model four times of polaron hopping energy (E_a) should coincide with the phonon assisted hopping (PAH) energy as $\omega_T = E_{PAH} = 4E_a$ (Austin and Mott, 1969). Plotting four times of activation energy (i.e., $4E_a$) in Fig. 72, it is seen that it runs almost parallelly with the transversal optical modes (ω_T). The systematically higher values of E_{PAH} (i.e. ω_T) can be related to the high disorder effect or due to stronger effective

electron-phonon coupling strength. Alternatively this could support the Feynman-polaron model, where drift mobility term of polaron and the internal polaron excitation shows a more complex relationship. Since the oscillator strength (Table 13) increases with increasing number of doped electrons, “saturation of polaron” concept as described earlier (Salje *et al.* 1984, Rüschler *et al.*, 1988a and 1988b) can be ruled out.

From the Kramers-Kronig transformation (KKT) of the measured reflectivity spectra it has been found that there is no zero-crossing of ϵ_1 for all samples (i.e., $x \leq 9$) for the $E \perp c$ direction as well as for the $x \leq 4$ samples for $E \parallel y$ direction. This is due to the relatively less oscillator strength (F) and high damping (γ) (see Table 13 and 14). Therefore, the zero-crossings of ϵ_1 (= longitudinal optical modes, ω_L) are calculated using Lyddane-Sachs-Teller relation (Eq. 29) taking the fit parameter values given in Table 13 and Table 14. These values are shown in Fig. 72. It is seen that these values nearly fits with the values obtained using KKT for the metallic like samples ($x \geq 8$). This may be due to the very less Drude contribution, i.e. to the fact that the oscillator dominates in the optical properties here.

6. SUMMARY

Systematic investigations of Na_xWO_3 series, prepared by conventional solid state method, show that a new stability field of different phases exist. The relative contributions of different phases have been calculated using Rietveld refinement method. It is, therefore, important to consider the existence and contribution of different phases before any interpretation about properties of samples which is related to composition. Especially, any model that interpret the absolute value of sodium content for metal to insulator transition and the observed variation of superconducting transition temperature with sodium concentration should consider this fact. Thus, this systematic study of Na_xWO_3 series may stimulate other experimental and theoretical investigations. It has been shown that for $\text{PTB}_t \text{Na}_{0.1}\text{WO}_3$ phase the puckering effect, i.e. the off centering of W along c -axis and tilting of WO_6 octahedra around c -axis occurs, which is consistent with the XRD pattern indexing using space group $P4/ncc$ instead of $P4/nmm$. Similarly, Glazer (1972) type of tilting $a^+a^+a^+$ is observed in $\text{PTB}_c \text{Na}_x\text{WO}_3$ system, which is consistent with the space group Im-3 . The relationship between lattice parameters of different perovskite Na_xWO_3 and Li_xWO_3 has been discussed. It has been argued that the increase in lattice parameters for cubic Na_xWO_3 system and decrease in lattice parameters for cubic Li_xWO_3 system with increasing x is due to the increasing W-O bond length, and increasing tilt angle of WO_6 octahedra, respectively.

The composition dependent IR absorption spectra and Raman spectra of Na_xWO_3 system has been systematically investigated and compared with that of the Li_xWO_3 system. The decrease in peak positions with increasing sodium content (in IR absorption spectroscopy) of $\text{PTB}_t \text{Na}_x\text{WO}_3$ system is due to the increase in average W-O-W distances, which is directly related to the lattice parameter increase. It has been shown that one can distinguish different phases (PTB_o , PTB_t , metallic (TTB and PTB_c)) from spectral behavior. So the present systematic study of the absorption spectra may improve the discrepancy existing in the literatures (e.g., Krašovec *et al*, 2001) specially in the field of thin film techniques, which is very important for further applications.

Solid state synthesis in the system $\text{Na}_{0.8}\text{Nb}_y\text{W}_{1-y}\text{O}_3$ with $0.0 \leq y \leq 0.4$ enable the separation of three cubic perovskite type phases when $y \geq 0.25$. With the present synthesis conditions a substitution of niobium ($y < 0.1$) obtained as single phase. Moreover, a systematic increase in lattice parameter may indicate further Nb doping. Cubic Na_xWO_3 was found to be a common phase for nominal $0.10 \leq y \leq 0.4$ and show a gradual decrease of x with increasing nominal niobium content along with a new perovskite type phase of composition $\text{Na}_{0.5}\text{NbO}_{2.75}$. The new

phase, $\text{Na}_{0.5}\text{NbO}_{2.75}$ could not, however, be prepared as a single phase. Tetragonal potassium tungsten bronzes (TTB), K_xWO_3 , and its niobium substituted forms, $\text{K}_x\text{Nb}_y\text{W}_{1-y}\text{O}_3$ ($x = 0.55$, and $y = 0.0-0.55$), have been prepared by conventional solid state method. It has been shown that maximum 7% Nb ($y = 0.07$) could be doped in TTB type system in the applied preparation way and with the applied experimental parameters. For $y > 0.07$ distorted pyrochlore type phase of composition $\text{K}_{0.5}\text{Nb}_{0.5}\text{W}_{0.5}\text{O}_3$ was observed.

Optical reflectivities of single crystals of Li_xWO_3 (cubic), Na_xWO_3 (metallic), K_xWO_3 (HTB), Cs_xWO_3 (HTB), and $\text{Nb}_{18-x}\text{W}_{9+x}\text{O}_{69}$ (block type compounds) have been reinvestigated. It has been shown that the Drude free carrier description as used earlier for the interpretation of the optical properties of these systems concerning metallic properties is insufficient. Instead the single crystal reflectivity for metallic systems implies a separation in oscillator with the wavenumber at about 2000 cm^{-1} and a Drude free carrier contribution appropriate below. It has been discussed that this new separation of the optical properties is also useful to describe better the optical properties of tungsten bronzes in literatures (e.g. King *et al.* (1972) for $\text{Rb}_{0.33}\text{WO}_3$; Lynch *et al.* (1973) for $\text{Na}_{0.65}\text{WO}_3$, $\text{Na}_{0.735}\text{WO}_3$, and $\text{K}_{0.6}\text{WO}_3$). The exclusion of Drude free carrier type behavior can be established more obviously considering the Fig. 70, where the reported “pseudo-screened plasma frequency” (zero-crossing of ϵ_1) of all the systems varies linearly with chemical carrier concentration instead of square-root behavior. This new separation of the optical properties of tungsten bronzes systems into Drude free carrier and oscillator contribution is supported by reinvestigations of optical reflectivity of $\text{Nb}_{18-x}\text{W}_{9+x}\text{O}_{69}$ block type compounds, too. It is shown that the component parallel to the block axis shows a decrease (softening) of the small polaron “photon assisted hopping” (PAH) excitation. However, the polaron excitation does not disappear for the samples showing metallic properties, but there is an increasing Drude free electron contribution with increasing doping. According to this it is concluded that the optical properties of the metallic alkali metal tungsten bronzes and niobium tungsten oxide series are dominantly polaron properties, following a Feynman-polaron model with an oscillator effect for the internal oscillation and a Drude term for the polaron drift contribution.

7. REFERENCES

- Aird A, Salje EKH (2000): Enhanced reactivity of domain walls in WO_3 with sodium. *Eur. Phys. J. B* 15:205.
- Aristimuno AR, Shanks HR, Danielson GC (1980): Electrical Resistivity of Hexagonal Tungsten Bronzes. *J. Solid State Chem.* 32:245.
- Austin IG, Mott NF (1969): Polarons in Crystalline and Non-Crystalline Materials. *Adv. Phys.* 18:41.
- Böttger H, Bryksin VV (1985): Hopping Conduction in Solids, VCH, Weinheim.
- Brown BW, Banks E (1954): The Sodium Tungsten Bronzes. *J. Am. Chem. Soc.* 76:963.
- Brunner O (1903): Thesis Zürich (This reference is cited from Magnéli (1949)).
- Cadwell LH, Morris RC, Moulton WG (1981): Normal and Superconducting Properties of K_xWO_3 . *Phys. Rev. B* 23:2219.
- Clarke R (1977): New Sequence of Structural Phase Transitions in Na_xWO_3 . *Phys. Rev. Lett.* 39:1550.
- Darlington CNW, Knight KS (1999): High-temperature phases of NaNbO_3 and NaTaO_3 . *Acta Crystallogr. B* 55:24.
- Darriet B, Rat M, Galy J (1970): Phases $\text{K}_x\text{V}_x\text{W}_{1-x}\text{O}_3$ and $\text{K}_x\text{Nb}_x\text{W}_{1-x}\text{O}_3$. *C. R. Acad. Sci., Ser. C* 271:1324.
- Debnath T, Rüschler CH, Gasing TM, Koepke J, Hussain A (2008a): Solid-state synthesis in the system $\text{Na}_{0.8}\text{Nb}_y\text{W}_{1-y}\text{O}_3$ with $0 \leq y \leq 0.4$: A new phase, $\text{Na}_{0.5}\text{NbO}_{2.75}$, with perovskite-type structure. *J. Solid State Chem.* 181:783.
- Debnath T, Roy SC, Rüschler CH, Hussain A (2008b): Synthesis and characterization of niobium doped potassium tetragonal tungsten bronzes, $\text{K}_x\text{Nb}_y\text{W}_{1-y}\text{O}_3$. *J. Mater. Sci.* (under review, manuscript number: JMSC10884R1).
- Deschanvres A, Frey M, Raveau B, Thomazea Jc (1968): Substitution of Tungsten by Tantalum and Niobium in Potassium Tungstates . Evidence for New Phases $\text{K}_x(\text{Nb}_x\text{W}_{1-x})\text{O}_3$. *Bull. Soc. Chim. Fr.*:3519.
- Devreese JT (1971): Polarons in Ionic Crystals and Polar Semiconductors, North-Holland Publ. Comp., Amsterdam.
- Devreese JT, Peeters F (1982): Polarons and Excitations in Polar Semiconductors and Ionic Crystals. Plenum, New York, NATO ASI series B: Physics, Vol. 108.
- Dey KR (2004): Synthesis and Characterisation of alkali metal tungsten bronzes, Li_xWO_3 and $\text{M}_x\text{M}'_y\text{W}_{1-y}\text{O}_3$ ($\text{M} = \text{Li, Na, Cs}$ and $\text{M}' = \text{Nb, Mo}$) Systems. Thesis Hannover.

- Dey KR, Rüschler CH, Gesing TM, Hussain A (2007): Phase transformation of lithium tungsten bronzes, Li_xWO_3 , at room temperature ambient conditions. *Mater. Res. Bull.* 42:591.
- Dickens PG, Whittingham MS (1968): Tungsten Bronzes and Related Compounds. *Quart. Rev. Chem. Soc.* 22:30.
- Dubson MA, Holcomb DF (1985): Metal-Insulator Transition in the Compensated Sodium Bronze, $\text{Na}_x\text{Ta}_y\text{W}_{1-y}\text{O}_3$. *Phys. Rev. B* 32:1955-1960.
- Egdell RG, Jones GB (1989): Evidence for Polaronic States in $\text{Na}_{0.1}\text{WO}_3$ from Raman-Scattering. *J. Solid State Chem.* 81:137.
- Ekstrom T, Tilley RJD (1980): The Crystal Chemistry of the Ternary Tungsten Oxides. *Chem. Scripta* 16:1.
- Evrard R (1971): The Fröhlich Polaron Concept, in *Polarons in Ionic Crystals and Polar Semiconductor*, edited by JT Devreese, North-Holland Publ. Comp., Amsterdam., p29.
- Feinleib J, Scouler WJ, Ferretti A (1968): Optical Properties of Metal ReO_3 from 0.1 to 22 eV. *Phys. Rev.* 165:765.
- Feynman RP, Hellwarth RW, Iddings CK, Platzman PM (1962): Mobility of Slow Electrons in a Polar Crystal. *Phys. Rev.* 127:1004.
- Fröhlich H (1966): Dielectric Instabilities, in *Ferroelectricity*, edited by EF Weller, p.9.
- Fröhlich H, Pelzer H, Zienau S (1950): *Phil. Mag.* 41:221. (This reference is cited from Evrard (1971)).
- Galasso F, Katz L, Ward R (1959): Tantalum analogs of the Tetragonal Tungsten Bronzes. *J. Am. Chem. Soc.* 81:5898.
- García-Ruiz A, Bokhimi (1992): Superconductivity and Crystalline Structure in the Na-W-O System. *Physica C* 204:79.
- Gatehouse BM, Wadsley AD (1964): Crystal Structure of High Temperature Form of Niobium Pentoxide. *Acta Crystallogr.* 17:1545.
- Glazer AM (1972): Classification of Tilted Octahedra in Perovskites. *Acta Crystallogr. B* 28:3384.
- Glazer AM (1975): Simple Ways of Determining Perovskite Structures. *Acta Crystallogr. A* 31:756.
- Glemser O (1943): The structure of blue tungsten. *Z. Anorg. Allg. Chem.* 252:147.
- Granqvist CG (2000): Electrochromic tungsten oxide films: Review of progress 1993-1998. *Sol. Energy Mater. Sol. Cells* 60:201.

- Groh H, Gruehn R (1983a): Contributions to the Investigation of Inorganic Non-Stoichiometric Compounds .22. New Metastable Block Structures in the System $\text{Nb}_2\text{O}_5/\text{WO}_3$, Electron-Optical Investigation Z. Anorg. Allg. Chem. 503:165.
- Groh H, Meyer B, Gruehn R (1983b): Contributions to the Investigation of Inorganic Non-Stoichiometric Compounds .20. Metastable Oxidation of a Series of Solid-Solutions - an access to W-rich Block Structures in the System $\text{Nb}_2\text{O}_5/\text{WO}_3$. Z. Anorg. Allg. Chem. 497:56.
- Groh H, Meyer B, Gruehn R (1982): Electron-Microscopic Study of New Block Structures in the Metastable $\text{Nb}_2\text{O}_5\text{-WO}_3$ System. Z. Kristallogr. 159:53.
- Gu ZJ, Ma Y, Zhai TY, Gao BF, Yang WS, Yao JN (2006): A simple hydrothermal method for the large scale synthesis of single crystal potassium tungsten bronze nanowires. Chem. A Eur. J. 12:7717.
- Guo J, Dong C, Yang LH, Fu GC (2005): A green route for microwave synthesis of sodium tungsten bronzes Na_xWO_3 ($0 < x < 1$). J. Solid State Chem. 178:58.
- Hägg G (1935): Information on cubic sodium tungsten bronzes. Z. Phys. Chem. B 29:192.
- Hallopeau LA (1900): Ann. Chim. Phys. 7, 19: 92(This reference is cited from Magnéli (1949)).
- Heurung G, Gruehn R (1980): Electron-Microscopy of Structure of WO_3 Systems with Niobium (V) Oxide Crystals. J. Less-Common Met. 76:17.
- Hirano A, Masumi T (1987): Cyclotron-Resonance of Polarons in Pure AgCl. Solid State Commun. 63:439.
- Holstein T (1959): Studies of Polaron Motion: Part I. The molecular crystal model, Annals Phys. 8: 325; Part II. The Small Polaron. Annals Phys 8:343.
- Howard CJ, Luca V, Knight KS (2002): High-temperature phase transitions in tungsten trioxide - the last word? J. Phys.: Condens. Matter 14:377.
- Hussain A (1978): On the Alkali Metal Tungsten Bronzes in particular to those of Potassium, Rubidium and Cesium . Chem. Commun. Univ. Stockholm No. 2: 1.
- Hussain A, Gruehn R (1989): Contributions to the investigation of inorganic non-stoichiometric compounds .36. Tungsten-rich Solid Solution Series of $(\text{Nb}, \text{W})\text{O}_x$ Phases Having Block Structures - Preparation by Chemical Transport. Z. Anorg. Allg. Chem. 571:91.
- Hussain A, Gruehn R, Rüschler CH (1997): Crystal growth of alkali metal tungsten bronzes M_xWO_3 ($\text{M}=\text{K}, \text{Rb}, \text{Cs}$), and their optical properties. J. Alloys Compds. 246:51.
- Hussain A, Ul-Monir A, Murshed MM, Rüschler CH (2002): Synthesis and characterization of niobium substituted hexagonal tungsten bronzes. Z. Anorg. Allg. Chem. 628:416.
- Ingham B, Hendy SC, Chong SV, Tallon JL (2005): Density functional studies of tungsten trioxide, tungsten bronzes, and related systems. Phys. Rev. B 72: 5109.

- Johansson KE, Palm T, Werner PE (1980): An automatic micro densitometer for X-ray powder diffraction photographs. *J. Phys. E: Sci. Instrum.* 13:1289.
- Kielwein M, Saiki K, Roth G, Fink J, Paasch G, Egdell RG (1995): High-Energy Electron-Energy-Loss Study of Sodium Tungsten Bronzes. *Phys. Rev. B* 51:10320.
- Kihlborg L, Sharma R (1982): Order and disorder in compounds with tungsten bronze structures. *J. Microsc. Spectrosc. Electron.* 7: 387.
- Kihlborg L, Klug A (1973): Alkali metal distribution in tetragonal potassium tungsten bronze structure. *Chem. Scripta* 3:207.
- King CN, Benda JA, Greene RL, Geballe TH (1972): Specific Heat, Optical, and Transport Properties of Hexagonal Tungsten Bronzes. *Low Temperature Physics, LT-13*, edited by Timmerhaus *et al.* Plenum, New York, Vol. 3, p 411.
- Klimova IP, Voronkova VI, Yanovskii VK (1995): New Compounds $AB_nW_{3-n}O_9$ with the Hexagonal Tungsten Bronze Structure. *Inorg. Mater.* 31:245.
- Krašovec UO, Vuk AS, Orel B (2001): IR Spectroscopic studies of charged-discharged crystalline WO_3 films. *Electrochim. Acta* 46:1921.
- Kuhn A, Bashir H, Dos Santos AL, Acosta JL, Garcia-Alvarado F (2004): New protonic solid electrolyte with tetragonal tungsten bronze structure obtained through ionic exchange. *J. Solid State Chem.* 177:2366.
- Labbe Ph (1992): Tungsten Oxides, Tungsten Bronzes and Tungsten Bronze-type Structures. *Key Eng. Mater.* 68: 293.
- Landau LD (1933): *Phys. Z. Sowjetunion* 3:664. (This reference is cited from Salje *et al.* (1995)).
- Landau LD, Pekar SI (1946): *Zh. Eksperim. I Teor. Fiz.* 16:341(This reference is cited from Devreese (1972)).
- Laurent A (1838): *Ann. Chim. Phys.* 267 : 215 (This reference is cited from Magnéli (1949)).
- Lee SH, Seong MJ, Cheong HM, Ozkan E, Tracy EC, Deb SK (2003): Effect of crystallinity on electrochromic mechanism of Li_xWO_3 thin films. *Solid State Ionics* 156:447.
- Leitus G, Cohen H, Reich S (2002): Interplay of Cs concentration, dimensionality and superconductivity in Cs_xWO_3 . *Physica C* 371:321.
- Locherer KR, Swainson IP, Salje EKH (1999): Phase transitions in tungsten trioxide at high temperatures - a new look. *J. Phys.: Condens. Matter* 11:6737.
- Lyddane RH, Sachs RG, Teller E (1941): On the polar vibrations of alkali halides. *Phys. Rev.* 59:673.
- Lynch DW, Rosei R, Weaver JH, Olson CG (1973): Optical properties of some alkali metal tungsten bronzes from 0.1 to 38 eV. *J. Solid State Chem.* 8:242.

- Maczka M, Hanuza J, Majchrowski A (2001): Vibrational properties of ferroelectric hexagonal tungsten bronzes $AB_xW_{3-x}O_9$, where A = K, Rb, Cs and B=Nb, Ta, Zr, Cr. *J. Raman Spectrosc.* 32:929.
- Magnéli A (1949): The crystal structure of tetragonal potassium tungsten bronze. *Arkiv. Kemi* 1:213.
- Magnéli A (1951): Tetragonal tungsten bronzes of degenerated perovskite type. *Acta Chem. Scan.* 5:670.
- Magnéli A (1953): Studies on the hexagonal tungsten bronzes of potassium, rubidium and cesium. *Acta Chem. Scan.* 7:315.
- Magnéli A, Blomberg B (1951): Contribution to the knowledge of the alkali tungsten bronzes. *Acta Chem. Scan.* 5:372.
- McNeill W, Conroy LE (1962): Electrical properties of some dilute cubic sodium tungsten bronzes. *J. Chem. Phys.* 36:87.
- Miyamoto Y, Kume S, Doumerc JP, Hagenmuller P (1983): High pressure synthesis and structural evolution of new compounds of formulation $NaNb_{1-x}W_xO_3$. *Mater. Res. Bull.* 18:1463.
- Nimmo KM, Anderson JS (1972): Reduction and non-stoichiometry of niobium pentoxide. *J. C. S. Dalton Trans.*:2328.
- Obayashi H, Anderson JS (1976): Solid-State Reactions in System $Nb_2O_5.WO_3$ – Electron Microscopic Study. *J. Solid State Chem.* 19:331.
- Owen JF, Teegarden KJ (1978): Optical properties of the sodium tungsten bronzes and tungsten trioxide. *Phys. Rev. B* 18:3827.
- Raj S, Hashimoto D, Matsui H, Souma S, Sato T, Takahashi T, Ray S, Chakraborty A, Sarma DD, Mahadevan P, McCarroll WH, Greenblatt M (2005): Angle-resolved photoemission spectroscopy of the metallic sodium tungsten bronzes Na_xWO_3 . *Phys. Rev.* 72: 125125.
- Raj S, Hashimoto D, Matsui H, Souma S, Sato T, Takahashi T, Sarma DD, Mahadevan P, Oishi S (2006): Angle-resolved photoemission spectroscopy of the insulating Na_xWO_3 : Anderson localization, polaron formation, and remnant Fermi surface. *Phys. Rev. Lett.* 96: 147603.
- Raub CJ, Broadsto.S, Matthias BT, Jensen MA, Sweedler AR (1964): Superconductivity of sodium tungsten bronzes. *Phys. Rev. Lett.* 13:746.
- Raveau B, Thomazea Jc (1968): Novel phases of pyrochlore type. *C. R. Acad. Sci., Ser. C* 266:540.
- Reau JM, Fouassie.C, Leflem G, Barruad JY, Doumerc JP, Hagenmul. P (1970): Systems $WO_3-WO_2-A_2O$ (A = $WO_3-WO_2-Li_2O$, $WO_3-WO_2-Na_2O$, $WO_3-WO_2-K_2O$). *Revue Chimie Miner.* 7:975.

- Reich S, Leituss G, Tssaba Y, Levi Y, Sharoni A, Millo O (2000): Localized high- T_c superconductivity on the surface of Na-doped WO_3 . *J. Superconductivity* 13:855.
- Ribnick AS, Post B, Banks E (1963): Phase transitions in sodium tungsten bronzes. *Adv. Chem. Ser.* 39: 246.
- Rimmer MP, Dexter DL (1960): Optical constants of germanium in the region 0-10 eV. *J. Appl. Phys.* 31:775.
- Roth RS, Wadsley AD (1965a): Multiple phase formation in binary system Nb_2O_5 - WO_3 . I. preparation and identification of phases. *Acta Crystallogr.* 19:26.
- Roth RS, Wadsley AD (1965b): Multiple phase formation in binary system Nb_2O_5 - WO_3 . 2. structure of monoclinic phases $\text{WNb}_{12}\text{O}_{33}$ and $\text{W}_5\text{Nb}_{16}\text{O}_{55}$. *Acta Crystallogr.* 19:32.
- Roth RS, Wadsley AD (1965c): Multiple phase formation in binary system Nb_2O_5 - WO_3 . 3. structures of tetragonal phases $\text{W}_3\text{Nb}_{14}\text{O}_{44}$ and $\text{W}_8\text{Nb}_{18}\text{O}_{69}$. *Acta Crystallogr.* 19:38.
- Roth RS, Wadsley AD (1965d): Multiple phase formation in binary system Nb_2O_5 - WO_3 . 4. block principle. *Acta Crystallogr.* 19:42.
- Roth RS, Waring JL (1966): Phase equilibria as related to crystal structure in system niobium pentoxide-tungsten trioxide. *J. Res. Nat. Bur. Stand. Sect. A* 70:281.
- Roy SC (2007): Studies on niobium substituted potassium tetragonal tungsten bronzes (K-TTB). M.S. Thesis, University of Dhaka.
- Rüscher CH, Salje E, Hussain A (1988a): The effect of high polaron concentration on the polaron transport in $\text{NbO}_{2.5-x}$: optical and electrical properties. *Solid State Phys.* 21:3737.
- Rüscher CH, Salje E, Hussain A (1988b): The effect of the Nb-W distribution on polaronic transport in ternary Nb-W oxides: electrical and optical properties. *Solid State Phys.* 21:4465.
- Rüscher CH (1992): The structural effect on the electrical properties of $\text{NbO}_{2.5-x}$ block-type compounds. *Physica C* 200:129.
- Rüscher CH (1995): The near infrared and optical absorption of high- T_c superconductors using powders. in *Polarons and Bipolarons in High- T_c Superconductors and Related Materials*, edited by Salje EKH, Alexandrov AS and Liang WY, Cambridge University Press. p. 206.
- Rüscher CH, Dey KR, Debnath T, Horn I, Glaum R, Hussain A (2008): Perovskite tungsten bronze-type crystals of Li_xWO_3 grown by chemical vapour transport and their characterisation. *J. Solid State Chem.* 181:90.
- Rüscher CH, Zimmermann M, Gotte M (1993): Investigations of the anisotropic optical reflectivity of binary and ternary Nb-W oxides possessing block-type crystal structure. *Z. Naturforsch.* 48a:443.

- Sabatier R, Baud G (1972): Tungsten Bronzes with 2 Cations in Octahedral Site. *J Inorg. Nucl. Chem.* 34:873.
- Salje E (1975): Lattice dynamics of WO_3 . *Acta Cryst.* A31: 360.
- Salje E (1976): Structural Phase Transitions in System $\text{WO}_3\text{-NaWO}_3$. *Ferroelectrics* 12:215.
- Salje E, Hoppmann G (1980): High Temp. High Press. Phys. High-pressure transformations of tungsten trioxide 12: 213.
- Salje EKH, Alexandrov AS, Liang WY (1995): Polarons and Bipolarons in High- T_c Superconductors and Related Materials. Cambridge University Press.
- Salje E, Güttler B (1984): Anderson Transition and Intermediate Polaron Formation in WO_{3-x} Transport-Properties and Optical-Absorption. *Philos. Mag. B* 50 :607.
- Sanjuan ML, Kuhn A, Azcondo MT, Garcia-Alvarado F (2008): Proton and deuteron exchange in TTB-like $\text{Na}_{1.2}\text{Nb}_{1.2}\text{W}_{0.8}\text{O}_6$: Structural characterization and spectroscopic study. *Eur. J. Inorg. Chem.*:49.
- Schäfer E (1903): *Z. anorg. allg. Chem.* 38:142 (This reference is cited from Magnéli (1949)).
- Shanks HR (1972): Growth of tungsten bronze crystals by fused salt electrolysis. *J. Cryst. Growth.* 13/14:433.
- Sharma R (1985): Bronzoid phases in the pseudo binary system $\text{K}_x\text{Nb}_x\text{W}_{1-x}\text{O}_3$ and $\text{Cs}_x\text{Nb}_x\text{W}_{1-x}\text{O}_3$. *Mater. Res. Bull.* 20:1373.
- Sharma R, Kihlberg L (1981): Structures and defects of new intergrowth tungsten bronze analogs revealed by High-Resolution Electron-Microscopy. *Mater. Res. Bull.* 16:377.
- Shen ZX, Wang XB, Kuok MH, Tang SH (1998): Raman scattering investigations of the antiferroelectric-ferroelectric phase transition of NaNbO_3 . *J. Raman Spectrosc.* 29:379.
- Sienko MJ, Macennnes.S (1963): Electrical and magnetic properties of potassium tungsten bronze and rubidium tungsten bronze. *Inorg. Chem.* 2:485.
- Skokan MR, Moulton WG, Morris RC (1979): Normal and superconducting properties of Cs_xWO_3 . *Phys. Rev. B* 20:3670.
- Stanley RK, Morris RC, Moulton WG (1979): Conduction properties of the hexagonal tungsten bronze, Rb_xWO_3 . *Phys. Rev. B* 20:1903.
- Stern F (1963): Elementary Theory of the Optical Properties of Solids. *Sol. State Phys.* 15: 299.
- Takusagawa F, Jacobson RA (1976): Crystal Structure Studies of Tetragonal Sodium Tungsten Bronzes, Na_xWO_3 .1. $\text{Na}_{0.33}\text{WO}_3$ and $\text{Na}_{0.48}\text{WO}_3$. *J. Solid State Chem.* 18:163.

- Triantafyllou ST, Christidis PC, Lioutas CB (1997): X-ray and electron diffraction study of the tetragonal sodium tungsten bronze, $\text{Na}_{0.10}\text{WO}_3$, with distorted perovskite structure. J. Solid State Chem. 133:479.
- Vogt T, Woodward PM, Hunter BA (1999): The high-temperature phases of WO_3 . J. Solid State Chem. 144:209.
- Walkingshaw AD, Spaldin NA, Artacho E (2004): Density-functional study of charge doping in WO_3 . Phys. Rev. B 70:165110.
- Wechter MA, Shanks HR, Voigt AF (1968): Relations between Lattice Parameter and x Value for Some Cubic Tungsten Bronzes. Inorg. Chem. 7:845.
- Weller PF, Taylor BE, Mohler RL (1970): Crystal preparation of doped sodium tungsten bronze. Mater. Res. Bull. 5:465.
- Werner PE (1970): A Fortran Program for Least-Squares Refinement of Crystal-Structure Cell Dimensions. Arkiv Kemi 31:513.
- Wiseman PJ, Dickens PG (1976): Neutron-Diffraction Studies of Cubic Tungsten Bronzes. J. Solid State Chem. 17:91.
- Wöhler F (1823): Ann. Chim. Phys. 29:43. (This reference is cited from Brown *et al.* (1954)).
- Woodward PM, Sleight AW, Vogt T (1997): Ferroelectric tungsten trioxide. J. Solid State Chem. 131:9.
- Yang XG, Li C, Mo MS, Zhan JH, Yu WC, Yan Y, Qian YT (2003): Growth of $\text{K}_{0.4}\text{WO}_3$ whiskers via a pressure-relief-assisted hydrothermal process. J. Cryst. Growth 249:594.
- Yuzyuk YI, Gagarina E, Simon P, Reznitchenko LA, Hennet L, Thiaudiere D (2004): Synchrotron x-ray diffraction and Raman scattering investigations of $(\text{Li}_x\text{Na}_{1-x})\text{NbO}_3$ solid solutions: Evidence of the rhombohedral phase. Phys. Rev. B 69:144105.

LIST OF PUBLICATIONS

Full Papers:

C.H. Rüschler, K.R. Dey, **T. Debnath**, I. Horn, R. Glaum, and A. Hussain, J. Solid State Chem. 181 (2008) 90, Perovskite tungsten bronze-type crystals of Li_xWO_3 grown by chemical vapour transport and their characterisation.

T. Debnath, C.H. Rüschler, T. -M. Gesing, J. Koepke and A. Hussain, J. Solid State Chem. 181(2008) 783. Solid-state synthesis in the system $\text{Na}_{0.8}\text{Nb}_y\text{W}_{1-y}\text{O}_3$ with $0 \leq y \leq 0.4$: A new phase, $\text{Na}_{0.5}\text{NbO}_{2.75}$, with perovskite-type structure.

T. Debnath, S.C. Roy, C.H. Rüschler, and A. Hussain. J. Mater. Sci. (under review, manuscript number: JMSC10884R1), Synthesis and characterization of niobium doped potassium tetragonal tungsten bronzes, $\text{K}_x\text{Nb}_y\text{W}_{1-y}\text{O}_3$.

Conference contributions:

T. Debnath and A. Hussain, 2004, Book of extended abstract, 251-254, Bangladesh Chem. Soc. Solid state Synthesis and characterization of niobium doped sodium tungsten bronzes. (oral presentation)

T. Debnath, C.H. Rüschler, T.-M. Gesing and A. Hussain, Z. Kristallogr. Suppl., 24, 2006, 175, Phase separation into two cubic perovskites in the system $\text{Na}_{0.8}\text{Nb}_y\text{W}_{1-y}\text{O}_3$. (poster).

T. Debnath, C.H. Rüschler, I. Horn, T.-M. Gesing, K.R. Dey and A. Hussain, Beih. z. Eur. J. Mineral. Vol 18, 2006, No.1, 27, Investigation of $(\text{Na}, \text{Li})_x\text{WO}_3$ perovskites. (poster)

T. Debnath, C.H. Rüschler and A. Hussain, Z. Kristallogr. Suppl., 2007, Optical properties of Na_xWO_3 bronzes. (poster).

T. Debnath, S.C. Roy, C.H. Rüschler and A. Hussain, Z. Kristallogr. Suppl., 2008, Erlangen, Synthesis and characterization of niobium doped potassium tetragonal tungsten bronzes, $\text{K}_x\text{Nb}_y\text{W}_{1-y}\text{O}_3$. (poster).

T. Debnath, and C.H. Rüschler, Z. Kristallogr. Suppl., 2008, Erlangen, Charge carriers in Nb-W oxides with block type structure. (poster).

CURRICULUM VITAE

Personal Details:

Name:	Tapas Debnath
Present address:	Room No. 853, Jägerstraße 3-5, D-30167, Hannover, Germany
Date of birth:	12 th March 1977
Place of birth:	Netrakona, Bangladesh
Nationality:	Bangladeshi by birth
Gender:	Male

Education:

Primary School:	Adarsha Shishu School, Netrakona Year: 1982-87
Secondary School:	Anjuman Adarsha Govt. High School, Netrakona, Dhaka Board Year: 1987-92 , Grade: First class (with certificate)
Higher Secondary School:	Govt. Netrakona College, Dhaka Board. Year: 1992-94, Grade: First class (with certificate)
Bachelor of Science:	Dept. of Chemistry, University of Dhaka, Bangladesh Session start: 1995/1996 (8 semester) Final examination year: 2003 (with certificate)
Master of Science:	Dept. of Chemistry, University of Dhaka, Bangladesh Session start: 2000/2001 (3 semester) Final examination year: 2003, Grade: First Class (with certificate) Thesis Title: Synthesis and characterization of niobium doped sodium tungsten bronzes.
Doctoral Study:	Since June 2005: Ph.D. student at Institute of Mineralogy, Leibniz University of Hannover, Scholarship program: “Georg-Christoph-Lichtenberg-Stipendium” provided by Ministry of Science and Culture, Land Niedersachsen, Germany.

Since June 2008: Scientific co-worker at Institute of Mineralogy, Leibniz University of Hannover, in the “DFG project” “Pulversynthese und Charakterisierung müllitähnlicher Verbindungen des Typs $\text{Bi}_2\text{M}_4\text{O}_9$ ”.